

2014

## TIME LAPSE SEISMIC OBSERVATIONS AND EFFECTS OF RESERVOIR COMPRESSIBILITY AT TEAL SOUTH OIL FIELD

Nayer Islam  
*Michigan Technological University*

Follow this and additional works at: <https://digitalcommons.mtu.edu/etds>

 Part of the [Geophysics and Seismology Commons](#), and the [Petroleum Engineering Commons](#)

Copyright 2014 Nayer Islam

---

### Recommended Citation

Islam, Nayer, "TIME LAPSE SEISMIC OBSERVATIONS AND EFFECTS OF RESERVOIR COMPRESSIBILITY AT TEAL SOUTH OIL FIELD", Dissertation, Michigan Technological University, 2014.  
<https://doi.org/10.37099/mtu.dc.etds/811>

Follow this and additional works at: <https://digitalcommons.mtu.edu/etds>

 Part of the [Geophysics and Seismology Commons](#), and the [Petroleum Engineering Commons](#)

TIME LAPSE SEISMIC OBSERVATIONS AND EFFECTS OF RESERVOIR  
COMPRESSIBILITY AT TEAL SOUTH OIL FIELD

By  
Nayyer Islam

A DISSERTATION

Submitted in partial fulfillment of the requirements for the degree of

DOCTOR OF PHILOSOPHY

In Geological Engineering

MICHIGAN TECHNOLOGICAL UNIVERSITY

2014

©2014 Nayyer Islam

This dissertation has been approved in partial fulfillment of the requirements for the Degree of DOCTOR OF PHILOSOPHY in Geological Engineering.

Department of Geological and Mining Engineering and Sciences

Dissertation Advisor: *Dr. Wayne D. Pennington*

Committee Member: *Dr. Roger Turpening*

Committee Member: *Dr. Gregory P. Waite*

Committee Member: *Dr. Tamara Olson*

Department Chair: *Dr. John Gierke*

# Table of Contents

List of Figures.....	v
Preface.....	viii
Acknowledgements .....	ix
Abstract.....	x
<b>1. Introduction .....</b>	<b>1</b>
<b>2. Time-lapse observations of fluid movement at Teal South from poststack 3D seismic data.....</b>	<b>5</b>
2.1. Abstract.....	5
2.2. Introduction.....	5
2.3. Data Cross-Equalization .....	7
2.3.1. Travel-Time Equalization.....	8
2.3.2. Amplitude Equalization .....	11
2.3.3. Cross-Equalization of Time-Lapse Data for Phases I and II .....	18
2.4. Time-lapse Observations of Seismic Amplitudes.....	20
2.4.1. Methodology.....	23
2.4.2. Results and Discussion .....	23
2.5. Time-Lapse, Travel-Time Shifts, and Reservoir Compaction.....	37
2.5.1. Methodology.....	38
2.5.2. Results and Discussion .....	39
2.6. Conclusion .....	41
<b>3. Elastic property changes from reservoir compaction inferred from pre-stack seismic time-lapse data .....</b>	<b>43</b>
3.1. Abstract.....	43
3.2. Introduction.....	43
3.3. Teal South AVO .....	49
3.4. Rock-physics Modelling and AVO Response .....	51
3.4.1. Methodology.....	51
3.5. Results and Discussion .....	57

3.5.1.	Green’s Model and Hertz-Mindlin Model .....	57
3.5.2.	Effects of Friction and Pressure Dependence on AVO Gradient .....	69
3.5.3.	Walton’s Model for Anisotropic Unconsolidated Sands .....	74
3.6.	Conclusion .....	85
<b>4.</b>	<b>Conclusion .....</b>	<b>87</b>
<b>5.</b>	<b>Appendices.....</b>	<b>89</b>
5.1.	Appendix A: Reservoir Fluid, Shale and Sand Properties, and Pressure Data.	89
5.2.	Appendix B: Hertz-Mindlin Model .....	91
5.3.	Appendix C: Walton’s Model for Anisotropic Medium and Thomsen’s Anisotropy Parameters.....	93
5.4.	Appendix D: CMP Gathers Generated from the AVO curves Predicted by Rock Physics Models .....	96
5.5.	Appendix E: Permissions to use copyrighted material. ....	97
<b>6.</b>	<b>References.....</b>	<b>99</b>

# List of Figures

Figure 1. 1. Location of the Teal South oil field with respect to offshore Louisiana. ....	1
Figure 1. 2. Legacy and time-lapse survey boundaries. See Appendix E for permission. ...	3
Figure 2. 1. 4500-ft sand horizon tracked on legacy data. ....	6
Figure 2. 2. Static travel-time shift between legacy and Phase I data. ....	8
Figure 2. 3. Seismic section after applying a static shift of -77ms to time-lapse data. ....	9
Figure 2. 4. Lateral misalignment between legacy and Phase I data. ....	10
Figure 2. 5. Residual mistie between legacy and Phase I data. ....	12
Figure 2. 6. Reference reflector tracked on legacy data (a) and Phase I data (b). ....	12
Figure 2. 7. Amplitude equalization between legacy and Phase I data. ....	13
Figure 2. 8. Crossplots between legacy data (after amplitude equalization) and Phase I data throughout the volume. ....	14
Figure 2. 9. Histogram presenting Phase I/legacy ratio. ....	15
Figure 2. 10. Crossplot between legacy and Phase I data after cecross-equalization. ....	16
Figure 2. 11. A histogram of ratio between Phase I amplitude and legacy amplitude corrected by multiplication factor of 3800. ....	17
Figure 2. 12. Amplitude spectra for Phase I data (solid line) and legacy data (dashed line), both are filtered by a low pass filter of 50Hz. ....	18
Figure 2. 13. A histogram of travel time-shifts between Phase I and Phase II data. ....	19
Figure 2. 14. Crossplot between Phase I and Phase II data. ....	19
Figure 2. 15. Amplitude spectra of Phase I and Phase II data. ....	20
Figure 2. 16. A horizon tracked over the 4500-ft sand. ....	24
Figure 2. 17. A 3D structural view of reservoir A. ....	25
Figure 2. 18. Time slice 1480ms displaying difference in squared instantaneous amplitude. ....	25
Figure 2. 19. A random line connecting water encroachment with reservoir. ....	27
Figure 2. 20. Seismic section displaying the Phase I (blue) and Phase II (red) data in wiggle display on a random line. ....	28
Figure 2. 21. Same section as displayed in Figure 2.20 but Phase II data have been shifted up by almost 1ms. ....	28
Figure 2. 22. Time slices 1456 (assumed oil zone) and 1444 (assumed gas cap) displaying legacy and time-lapse difference over reservoir 'C'. ....	30
Figure 2. 23. Time slice 1460 exhibiting the effects of regional pressure drop on reservoir B. ....	32
Figure 2. 24. A body of reservoir 'B' is presented with all the three seismic data sets acquired over the Teal South oil field at three different times. ....	32
Figure 2. 25. Seismic section displaying a random line connecting reservoir 'B' with reservoir 'C'. ....	33
Figure 2. 26. Inline 3523 displaying Phase I data over reservoir 'B'. ....	34

Figure 2. 27. A three dimensional view of most likely leakage path for gas escaping from reservoir C.....	34
Figure 2. 28. A random seismic line exhibiting the fluid migration path from reservoir ‘C’ to ‘B’, .....	35
Figure 2. 29. Superimposed time slices exhibiting the location of the 'tiny' reservoir with respect to other neighboring reservoirs.....	36
Figure 2. 30. A random line connecting all the reservoirs exhibiting time-lapse changes. ....	36
Figure 2. 31. Another random line exhibiting a different path for pressure communication.....	37
Figure 2. 32. Time-lapse travel time shifts between legacy and Phase I data, presented on inline 3500 .....	39
Figure 2. 33. Time-lapse travel time shift between Phase I and Phase II data, presented on inline 3500 .....	40
Figure 3. 1. 3D structural view of 4500-ft sand tracked on legacy data. ....	44
Figure 3. 2. Production history and pressure profile of the 4500-ft sand, reservoir 'A'....	45
Figure 3. 3. Effect of frame stiffening on P-wave velocity and Poisson's ratio of reservoir 'A'. ....	46
Figure 3. 4. Partial stacks extracted from the unmigrated P-wave seismic data for the 4500' sand reservoir ‘A’.....	50
Figure 3. 5. AVO trend of 4500-ft sand reservoir ‘A’ .....	50
Figure 3. 6. A plot of co-ordination number with the porosity.....	54
Figure 3. 7. Elastic properties of 4500-sand predicted by Green’s model.....	59
Figure 3. 8. Elastic properties of reservoir A predicted by Hertz-Mindlin model.....	60
Figure 3. 9. P-wave velocity (purple) and Poisson's ratio (blue) for water sand estimated by Green's model .....	61
Figure 3. 10. Plot of p-wave velocity (purple) and Poisson's ratio (blue) of water sand computed by Hertz-Mindlin model.....	61
Figure 3. 11. AVO response of 4500-ft sand predicted from the rock properties estimated by Green’s Model .....	62
Figure 3. 12. AVO response of the 4500-ft sand using elastic properties predicted by Hertz-Mindlin model. ....	63
Figure 3. 13. Stacked seismic response predicted by Green’s Model. ....	64
Figure 3. 14. Stacked seismic response predicted by Hertz-Mindlin model. ....	65
Figure 3. 15. Plot of modeled seismic amplitude of oil zone as a function of $\sin^2(\theta)$ . ....	67
Figure 3. 16. Elastic properties estimated by Hertz-Mindlin model using different values of friction factor (f). ....	71
Figure 3. 17. Analysis of effects of friction factors on AVO response. ....	71
Figure 3. 18. Pressure dependence sensitivity of the Hertz-Mindlin Model. ....	73
Figure 3. 19. Plot of Thomsen's parameter with the strain anisotropy ( $E_{11}/E_{33}$ ). ....	76

Figure 3. 20. AVO response under anisotropic conditions caused by uniaxial compaction. ....	77
Figure 3. 21. Modelled amplitude for oil zone of reservoir ‘A’ versus $\text{Sin}^2\theta$ assuming anisotropic (uniaxial) conditions for Phase II data. ....	78
Figure 3. 22. Stacked seismic response predicted by Hertz-Mindlin model assuming anisotropic (uniaxial) conditions.....	79
Figure 3. 23. AVO curves predicted assuming triaxial compression. ....	80
Figure 3. 24. AVO trend of oil zone of 4500-ft sand assuming anisotropic conditions caused by triaxial compression. ....	81
Figure 3. 25. Stacked seismic response predicted by Hertz-Mindlin model assuming anisotropic conditions for Phase-II data caused by assumed triaxial compression. ....	83
Figure D. 1. NMO corrected synthetic CMP gathers presenting AVO response for 4500-ft sand predicted from Green's model and Zoeppritz equations.....	96
Figure D. 2. Synthetic CMP gathers presenting the AVO response of 4500-ft predicted by the Hertz-Mindlin model.....	96

## **Preface**

Chapter 2 of this dissertation is planned to be submitted to the Society of Exploration Geophysicists (SEG) to publish in its 'Interpretation' journal. The paper includes Dr. Wayne D. Pennington and Mohamed A. Ezawi as coauthors. Ezawi did data analysis using instantaneous amplitude on time-slices and made time-lapse observations from Phase I to Phase II. His observations are not included in this dissertation but were presented in 2012 at SEG conference in Las Vegas, NV. Nayyer Islam extended the previous work by Ezawi incorporating more data and some additional attributes, and provided greater detail in the visual observations of the changes in stacked time-lapse data from legacy to Phase I and Phase II. The paper presents all time-lapse observations made by Ezawi and Nayyer. Dr. Pennington provided the technical support for both works and did most of editing.

Chapter 3 will also be submitted for publication in 'Interpretation' journal by the SEG. Dr. Wayne D. Pennington is co-author on this paper. Nayyer Islam did the rock-physics modelling to explain the time-lapse behavior of Teal South oil-field and wrote the paper. The work was done under Dr. Pennington's supervision, he provided the technical support and did most of editing to the paper.

## Acknowledgements

I thank to Almighty Allah for blessing me with the intellectual capabilities and helping me throughout the challenging period of my graduate work. I could have never done it without His countless blessings and mercy on me.

I thank to Dr. Wayne D. Pennington (my advisor) for all his technical support and encouragement during my stay at Michigan Technological University. Throughout my academic career at Michigan Technological University he not only supported me for my research work but also encouraged me to grow my professional skills and leadership abilities. He has always helped me to come out of all difficult periods that I had during my graduation. I cannot list his contribution in building my career in the limited space here, but it is his efforts and encouragements to me that today I am very close to achieve the biggest goal of my life.

I pay my gratitude to my graduate committee for being patience towards my mistakes. A special thanks to Dr. Roger Turpening who have been a big source of literature for my work. He often provided me reading materials that helped me to strengthen my concepts and understandings of different technical topics.

I also thank to all my friends and colleagues who helped me in my work and wished me always the best, especially Dr. Imran Aslam, Abid Ali Mirza, Dr. Joshua Richardson, Irfan Haider, and many more to list.

Data for this works were provided by the Geophysical Inc., and Energy Research Clearing House. Software used in in time-lapse observations was provided by the dGB Earth Sciences, and Matlab codes used in chapter 3 were modified from the original codes by University of Calgary. I appreciate all of them for their contribution to the development of science and technology. I also thank Dr. Leon Thomson for sharing his spread-sheet on anisotropic AVO analysis that led the research work discussed in the second part of this dissertation.

I also thank the University of Engineering and Technology, Lahore and the Government of Pakistan for giving me an opportunity to come to USA for my graduate studies by sponsoring my first three years of education at Michigan Technological University.

I thank to my parents and parents in laws for trusting me, supporting me, praying for me and giving me the moral support throughout my graduate studies.

Last, but most important, I thank to my wife and my daughter (Irha Noor) for their support. I have not been able to fulfill my duties to them during this period but they always welcomed me with thanks, and gave me power to fight against all difficulties. I love you.

## Abstract

One of the original ocean-bottom time-lapse seismic studies was performed at the Teal South oil field in the Gulf of Mexico during the late 1990's. This work reexamines some aspects of previous work using modern analysis techniques to provide improved quantitative interpretations. Using three-dimensional volume visualization of legacy data and the two phases of post-production time-lapse data, I provide additional insight into the fluid migration pathways and the pressure communication between different reservoirs, separated by faults. This work supports a conclusion from previous studies that production from one reservoir caused regional pressure decline that in turn resulted in liberation of gas from multiple surrounding unproduced reservoirs. I also provide an explanation for unusual time-lapse changes in amplitude-versus-offset (AVO) data related to the compaction of the producing reservoir which, in turn, changed an isotropic medium to an anisotropic medium.

In the first part of this work, I examine regional changes in seismic response due to the production of oil and gas from one reservoir. The previous studies primarily used two post-production ocean-bottom surveys (Phase I and Phase II), and not the legacy streamer data, due to the unavailability of legacy prestack data and very different acquisition parameters. In order to incorporate the legacy data in the present study, all three post-stack data sets were cross-equalized and examined using instantaneous amplitude and energy volumes. This approach appears quite effective and helps to suppress changes unrelated to production while emphasizing those large-amplitude changes that are related to production in this noisy (by current standards) suite of data.

I examine the multiple data sets first by using the instantaneous amplitude and energy attributes, and then also examine specific apparent time-lapse changes through direct comparisons of seismic traces. In so doing, I identify time-delays that, when corrected for, indicate water encroachment at the base of the producing reservoir. I also identify specific sites of leakage from various unproduced reservoirs, the result of regional pressure blowdown as explained in previous studies; those earlier studies, however, were unable to identify direct evidence of fluid movement. Of particular interest is the identification of one site where oil apparently leaked from one reservoir into a "new" reservoir that did not originally contain oil, but was ideally suited as a trap for fluids leaking from the neighboring spill-point. With continued pressure drop, oil in the new reservoir increased as more oil entered into the reservoir and expanded, liberating gas from solution. Because of the limited volume available for oil and gas in that temporary trap, oil and gas also escaped from it into the surrounding formation. I also note that some of the reservoirs demonstrate time-lapse changes only in the "gas cap" and not in the oil zone, even though gas must be coming out of solution everywhere in the reservoir. This is explained by interplay between pore-fluid modulus reduction by gas saturation decrease and dry-frame modulus increase by frame stiffening.

In the second part of this work, I examine various rock-physics models in an attempt to quantitatively account for frame-stiffening that results from reduced pore-fluid pressure in the producing reservoir, searching for a model that would predict the unusual AVO features observed in the time-lapse prestack and stacked data at Teal South. While several rock-physics models are successful at predicting the time-lapse response for initial production, most fail to match the observations for continued production between Phase I and Phase II. Because the reservoir was initially overpressured and unconsolidated, reservoir compaction was likely significant, and is probably accomplished largely by uniaxial strain in the vertical direction; this implies that an anisotropic model may be required. Using Walton's model for anisotropic unconsolidated sand, I successfully model the time-lapse changes for all phases of production. This observation may be of interest for application to other unconsolidated overpressured reservoirs under production.

# 1. Introduction

The Teal South is a small oil field in Eugene Block 354 in the Gulf of Mexico. It is a shallow water (85m) reservoir that has produced both oil and gas from many small reservoirs composed of unconsolidated turbidite Tertiary sands. The reservoirs range from 4000ft to 8000ft in depth and are separated mainly by regional and local faults. Figure 1.1 shows the location of Teal South in the Gulf of Mexico.



Figure 1. 1. Location of the Teal South oil field with respect to offshore Louisiana. The image is created using Google Earth and the coordinates of one of the wells drilled in the field. See Appendix E for permission.

The reservoir of interest in this and many previous studies is located in the 4500ft-sand, named for its approximate depth. The reservoir has been labelled as reservoir ‘A’ in previous studies and will be called reservoir ‘A’ in this work as well. Reservoir ‘A’ is the only producing reservoir, among many small reservoirs in the formation. The reservoir is a highly porous, unconsolidated and over-pressured sand. Production from this reservoir started in November 1996 almost a year after acquisition of the “legacy” seismic data set. Previous studies suggest that at the time of discovery the reservoir was saturated with light oil without any free gas, although the reservoir pressure and temperature were very close to the bubble point. The initial production from the reservoir was under liquid expansion drive mechanism that caused a sudden and rapid drop in pressure. Soon after the start of production gas started coming out of solution and a pressure support developed by the gas cap. The ocean-bottom seismic data are composed of two time-lapse studies (Phase I and Phase II) obtained after production had resulted in free gas released from solution.

Being poorly consolidated and over-pressured, 4500ft-sand is very sensitive to pressure and saturation changes. Its high sensitivity to pressure and saturation changes and quick depletion make it a highly suitable candidate for time-lapse studies. In 1996, Texaco and Input/Output selected Teal South as a test site to investigate the efficiency of a novel 4C/4D permanent reservoir monitoring system. Under this project first set of time-lapse data (Phase I) was acquired using ocean bottom cables in July-August 1997, following nearly 8 months of production. In late 1997, the project was opened for industry participation under a consortium managed by the Energy Research Clearing House (ERCH). The consortium brought participation from many academic and industrial institutions to test and develop processing and interpretation techniques specific to ocean-bottom and/or time-lapse data. The consortium conducted a second phase of data acquisition (Phase II) again using ocean bottom cables in April 1999, after almost 30 months of production.

The Teal South project provided a total of three sets of seismic data, recorded at three different times, representing different reservoir conditions. The ocean-bottom time-lapse data (Phase I and Phase II) were acquired and processed with every effort to match the two survey geometries and processing flows to minimize changes unrelated to production; the details of survey geometry and processing steps are described in previous studies by (Druzhinin and MacBeth (2001), Ebrom, Krail, et al. (1998), Rodriguez-Suarez, Stewart, and Lu (2000)). The legacy data, however, were acquired using streamers and were processed independently of the time-lapse data. In addition, only post-stack data from the legacy data set was made available to us, while pre-stack data from the two time-lapse ocean-bottom surveys was available to all members of the ERCH consortium, including the academic partners. Figure 1.2 shows the survey boundaries for legacy and time-lapse surveys.

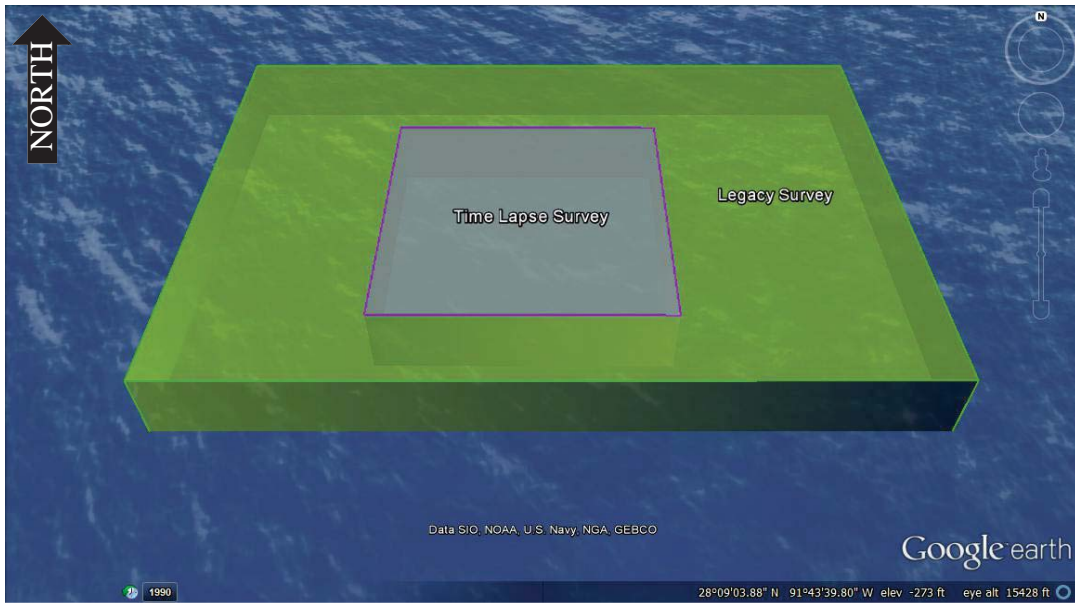


Figure 1. 2. Legacy and time-lapse survey boundaries. See Appendix E for permission.

Many previous studies have examined the time-lapse data from Teal South. Christie, MacBeth, and Subbey (2002) performed simulations, providing a history match for production data which was used by other studies, including the present one. Pennington et al. (2001), qualitatively explained time-lapse changes in Teal South using rock-physics models, AVO analysis of the time-lapse data sets, and inversion of the legacy stacked data set. They discovered that the pressure drop caused by production from reservoir ‘A’ was communicated to at least one ‘little neighbor’ reservoir which also exhibits time-lapse changes in spite of not being under production. They proposed that the fluid in the neighboring reservoir has dropped below bubble point, and gas is coming out of solution. They further predicted that the gas expansion in the neighbor was pushing oil down, ultimately to escape from the spill point into the surrounding formation. They accounted for the AVO observations with a model that required frame-stiffening of the formation as pore pressure decreases between Phases I and II. This model predicted a decrease in Poisson’s ratio (and an increase in AVO gradient) along with an increase in acoustic impedance (and a decrease in zero-offset reflection amplitude), matching the observations, at least qualitatively.

Ezawi, Pennington, and Islam (2012) used a specific seismic attribute, squared instantaneous amplitude, on time-slices of stacked data through the field in an effort to identify leakage of the oil (and gas) from the neighboring reservoirs. They confirmed the initial prediction by Pennington and others (2001): the oil and gas from a neighboring reservoir is leaking into the surrounding rocks from where it may be lost forever if not trapped by a secondary trap. They also identified the water influx from the down dip of the reservoir. Squared instantaneous amplitude was used in order to maximize the visual

effect of the amplitude changes while minimizing the visual clutter from lower-amplitude “noise” in the time-lapse data.

This work extends the previous work by Ezawi, Pennington, and Islam (2012) and Pennington et al. (2001), in two parts. In the first part (Chapter 2), it provides greater detail in the visual observations of the changes in stacked time-lapse data from legacy to Phase I and Phase II, after first performing cross-equalization to remove some artifacts. In the second part (Chapter 3), it quantitatively examines various frame-stiffening models in order to account for the amplitude-versus-offset observations in some detail, invoking anisotropic reservoir compaction in the only acceptable model examined.

## 2. <sup>1</sup>Time-lapse observations of fluid movement at Teal South from poststack 3D seismic data

### 2.1. Abstract

A combined analysis of poststack seismic time-lapse data and legacy data from Teal South was performed to investigate the details of regional pressure communication from production of one reservoir on neighboring unproduced reservoirs. This work supports previous observations of gas leakage from neighboring reservoirs. The use of squared instantaneous amplitude allows visualization of the large-amplitude changes while visually minimizing noise, while the use of translucency in the 3D time-lapse difference volumes assists in identifying features of interest that were unrecognized in earlier studies. For example, this investigation has found that fluid appears to have escaped from one small reservoir from its spill point, only to be trapped in a nearby structure, from which it ultimately escapes through that trap's spill point. Time-lapse travel-time shifts because of the compaction of the producing reservoir are also observed in the overburden and under-burden.

### 2.2. Introduction

Teal South is a small oil field in the Gulf of Mexico. The field has been the focus of many time-lapse studies because of its quick depletion and strong sensitivity to pressure and saturation changes. In 1996, Texaco and Input/Output initiated a time-lapse research project at Teal South to test one of the first 4D/4C permanent monitoring systems. In 1997, the project was handed over to a consortium managed by the Energy Research Clearing House. Many industrial and academic institutions then participated in the consortium to develop and test acquisition, processing, and interpretation techniques specific to time-lapse studies (Ebrom, Krail, et al. 1998, Ebrom, Nolte, et al. 1998, Pennington et al. 2001, Druzhinin and MacBeth 2001, Christie, MacBeth, and Subbey 2002, Ezawi, Pennington, and Islam 2012).

Three different sets of seismic data exist from three different times of production. The first, "legacy" data set was acquired in 1995 from conventional streamer arrays, almost a year before the start of production in November 1996. In August 1997, the first ("Phase I") of two ocean-bottom cable (OBC) data sets was acquired, using four east-west cables, each having six multi-component receiver stations. Data for "Phase II" were acquired in April 1999, after almost 30 months of production, with some additional cables deployed to improve imaging for targets deeper than those concerned in the present study. Further details on the Teal South data acquisition and processing can be found in the earlier

---

<sup>1</sup> The material contained in this chapter will be submitted for publication in *Interpretation*, a journal published by the Society of Exploration Geophysicists.

papers on the subject (Ebrom, Krail, et al. (1998), Rodriguez-Suarez, Stewart, and Lu (2000), Druzhinin and MacBeth (2001)).

The field has many small reservoirs that are separated by North-South trending faults. The main reservoir of interest in many previous time-lapse studies is the largest reservoir within the '4500-ft sand', labelled as reservoir 'A' in figure 2.1, which shows this horizon as tracked on the legacy (streamer) data with two attributes shown in colors. The red color in figure shows the typical brightspots that exhibit strong negative reflection coefficients, and the blue and green colors show the likely fault locations based on lowest coherence values. Reservoir A is the only reservoir within 4500-ft sand that was under production before Phase II data acquisition.

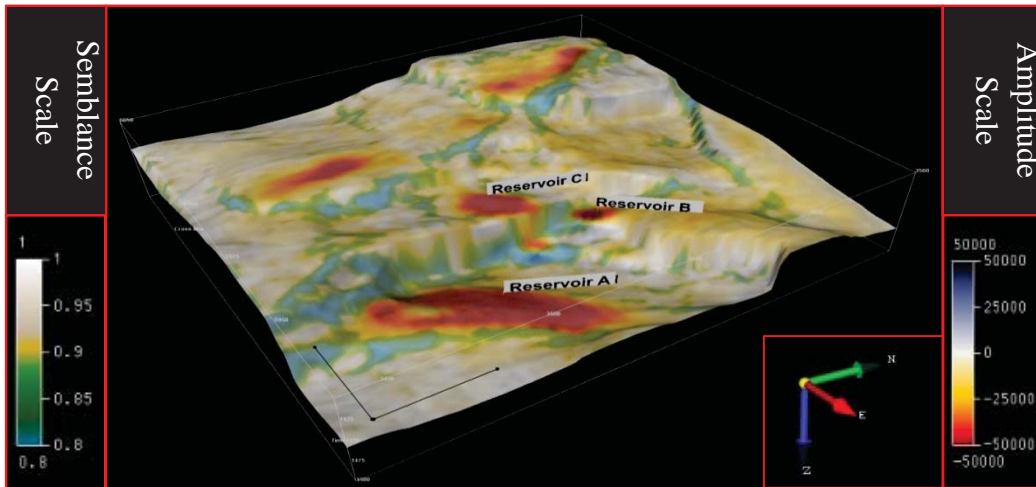


Figure 2. 1. 4500-ft sand horizon tracked on legacy data. Seismic amplitude from Phase II data is displayed on the horizon in red and black color scheme given on the right of figure. 40 % transparency is applied to seismic data. The reservoirs in the 4500-ft sand exhibit typical brightspot characteristics (bright strong negative reflections). Phase II data are underlain by a 'Semblance' attribute computed from legacy seismic data. Semblance is displayed using color scheme given on the left of the figure. The blue color represents the most likely locations of faults based on low coherence values. Reservoir 'A' is the only reservoir from 4500-ft sand that was under production at the times of time-lapse data acquisition. Other reservoirs ('B' and 'C') have been reported in previous studies exhibiting time-lapse changes. The black lines on the horizon show 1000ft length along x-axis and y-axis.

It has been demonstrated in previous studies that at the time of discovery reservoir 'A' was a light-oil reservoir that contained no free gas. It is very likely that other neighboring reservoirs were also saturated with light oil under similar conditions (Pennington et al. 2001). All the reservoirs appear as typical 'brightspots' on seismic sections (figure 2.1).

Pennington et al. (2001) performed rock-physics modelling and explained the time-lapse observations at the Teal South. They also pointed out that a small neighboring reservoir, exhibited time-lapse changes due to the production in reservoir 'A'. They proposed that the reservoirs are in pressure communication, most likely through the down-dip water-sand. Because of production from reservoir 'A', pressure drops in the 'little neighbors' resulting a fluid expansion and release of free gas in those reservoirs. They predicted that

the gas expansion would push the oil down to leak out the spill points to another trap or escape to overlying sands. Ezawi, Pennington, and Islam (2012), using squared instantaneous amplitude to assist in visualization, identified the previously predicted effects of fluid expansion and water encroachment on time slices through the data volume. They also identified gas leakage from a nearby small reservoir. In this study, the primary ‘little neighbor’ of Pennington et al. (2001) is referred to as reservoir ‘C’, and reservoir ‘B’ of Ezawi, Pennington, and Islam (2012) as reservoir ‘B’.

In this work, I extend the previous work presented by Ezawi, Pennington, and Islam (2012) to include the time-lapse differences between the legacy (streamer) data and Phase I (OBC) data. I will compare the time-lapse observation from legacy to Phase I and then from Phase I to Phase II. The data are analyzed in two aspects: production-induced changes in seismic response visualized through simple attributes based on amplitude, and production-induced compaction indicated by seismic travel-time shifts. For the first part, I use squared instantaneous amplitude to analyze the time-lapse changes from legacy to Phase I, and finally to Phase II. For the second part, trace matching based approach is used to determine the time shifts between any two seismic data sets (legacy to Phase I and Phase I to Phase II).

Through these observations, several features related to production from Reservoir A can be observed. This reservoir, which is the only one under production, apparently undergoes some vertical compaction, as indicated by travel-time changes. Deeper portion of one of the neighboring reservoirs appears to undergo some changes in reflection character between the time of the legacy data acquisition and that of Phase I acquisition, but not between Phases I and II, apparently due to a trade-off between the gas expansion effects on the fluid modulus and the stiffening effects on the rock frame. Some details of fluid migration, including water encroachment in Reservoir A, and migration of fluid from one of the neighbors through its spill point, into a small trap, and ultimately out of that trap through its spill point, are also observed.

### **2.3. Data Cross-Equalization**

The legacy streamer data and the two time-lapse OBC data sets were acquired with different survey geometries and different processing; because of this, there are many differences between the two (legacy and OBC) types of data sets that have no relation to the production process. To suppress the differences caused by different survey geometries and processing schemes, the first step in this work was to cross-equalize the legacy data with the time-lapse data. The pre-stack data were not available for the legacy (streamer) data set, so this study made use only of the post-stack migrated data for all data sets. The cross-equalization had two primary goals: all data sets should be well-aligned in terms of two-way travel times, and the amplitudes should be properly scaled to preserve the production-related changes in amplitude. The following sections describe the procedures used to cross-equalize the legacy streamer data and time-lapse OBC data.

### 2.3.1. Travel-Time Equalization

Both legacy and time-lapse data sets were imported in a single survey. Inlines and crosslines of time-lapse data were re-numbered to correspond to the numbering used in the legacy data, including conversion to feet from meters. After data loading, I aligned them in two-way travel time, using a reference reflector that is particularly flat, which exhibits strong reflections with few discontinuities, and concentrated on areas distant from reservoir 'A'. Figure 2.2 shows a 3D view of some of the seismic data from Teal South: legacy data is displayed on a crossline (right section) while the Phase I data is displayed on an intersecting inline (left section). The large time-shift between legacy and Phase I is due to the depth of the streamer cable (a few m) compared with the depth of the OBC (about 85m). A static shift of -77 ms was applied to time-lapse data (Phase I and Phase II) to temporally align it with legacy data. Figure 2.3 shows the image of same seismic sections as displayed in figure 2.2 after that static correction has been applied.

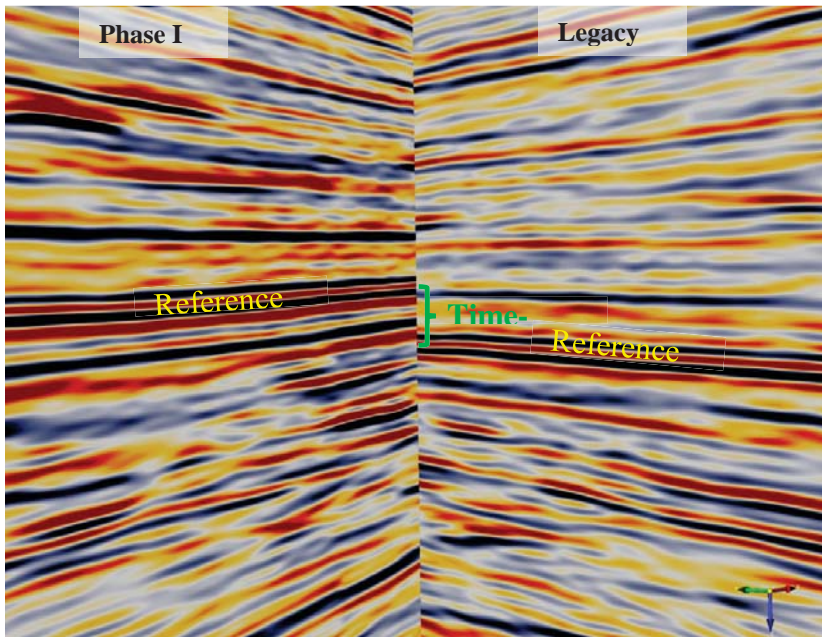


Figure 2. 2. Static travel-time shift between legacy and Phase I data. Figure shows legacy data on the right and seismic data from Phase I on the left. Red shows negative reflection coefficient and black shows positive reflection coefficient. The strong and continuous reflector at the center of the sections (labelled as 'reference') is used as a reference reflector for all equalization purposes. There is a significant time-shift between the legacy and Phase I data primarily because the legacy data is acquired with the streamer towed close to the water-surface while time-lapse data is recorded with ocean bottom cables that are deployed at the sea-floor. The water depth at Teal South is approximately 85 m.

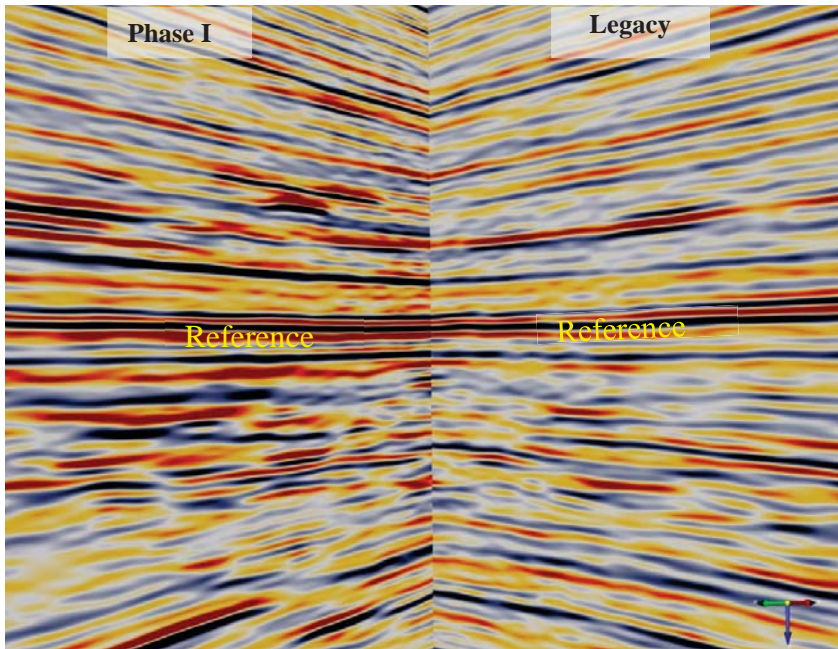


Figure 2. 3. Seismic section after applying a static shift of  $-77\text{ms}$  to time-lapse data. The reference reflector is now well aligned. Red color marks negative reflection coefficient and black color marks the positive reflection coefficient.

In addition to the shift in time, there is a small lateral shift between the two sets of surveys (see figure 2.4). A lateral shift equal to four seismic lines was applied to the time-lapse data in the cross-line direction. The time-lapse data are now in agreement with the legacy seismic within the limit of data quality. No lateral alignment is needed in the inline direction as both the legacy and time-lapse data tie nicely on crosslines.

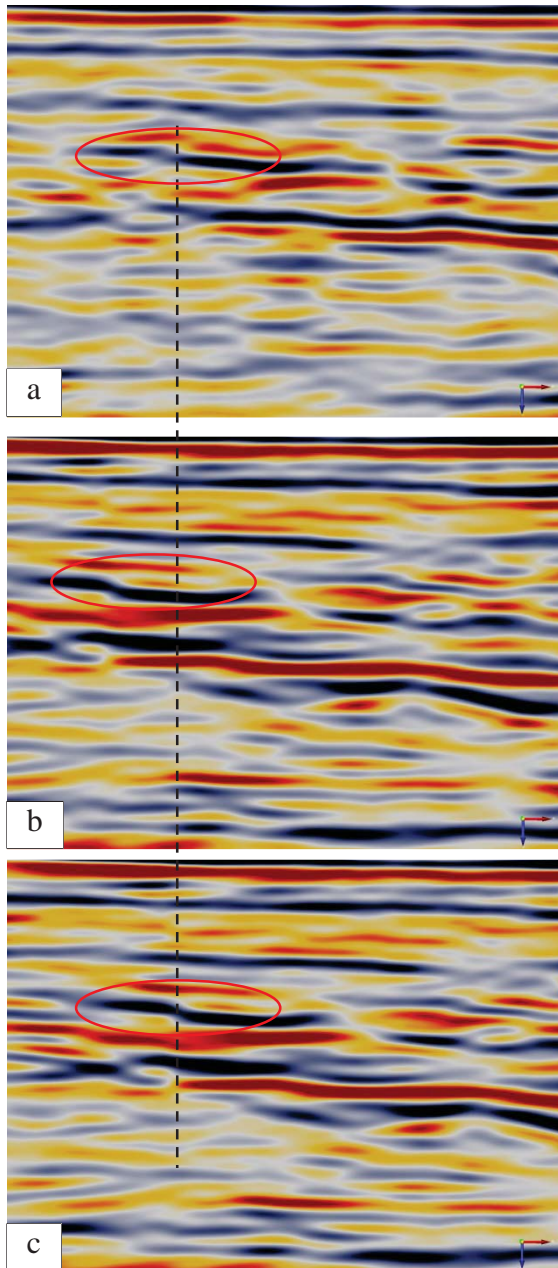


Figure 2. 4. Lateral misalignment between legacy and Phase I data. (a) Legacy Data, (b)Phase I data before lateral shift, (c) Phase I after lateral shift. The dashed line marks one feature that shows a mistie between the time-lapse data and the legacy data. After applying a lateral shift of 4 lines in the xline direction, the data is well-aligned.

After correcting for mistie by visual inspection, the time-lapse data and legacy data were then matched using a commercial software package to determine the residual statics that could be applied to improve the cross-equalization. Complete time-lapse data are processed in order to identify and correct for any compaction effect that may be present. The legacy data set was used as the reference, and a maximum shift of 10ms was

allowed. The output from the program is the time-difference of similar events on the two data sets (legacy and time-lapse data), named 'delta', throughout the volume. I then smoothed the delta function by applying a low pass filter using an average of several (typically 13) traces around any trace position. The filtered delta is then applied to the time-lapse data (Phase I and Phase II). In this way, I should be able to see the production induced amplitude variations more accurately and free of any error caused by misalignment of the data.

Figure 2.5 (a) shows crossline 6005. Legacy seismic data (black and red) are displayed in the figure, and is overlain by the residual mistie (smoothed delta with Phase I) value (blue and green). The smoothed delta value appears to change randomly in space and two-way traveltime, suggesting a significant degree of non-repeatability that results from the survey and processing differences. The smoothed delta value was applied to the Phase I and Phase II data sets to remove this random element, as shown in examples in Figure 2.5 (b) and 2.5 (c). After applying this correction, the data now seem well aligned throughout the section and can be used for amplitude comparisons after the amplitudes are scaled appropriately.

### **2.3.2. Amplitude Equalization**

Legacy and time-lapse data were scaled differently. After correcting for mistie between legacy and time-lapse data, the next step was to correct for amplitude differences. Because both data sets were processed independently it will not be possible to match them perfectly, but the match can be made sufficiently for our purposes. For amplitude equalization, I used Phase I and Phase II data that have already been corrected for mistie.

Again for this purpose, I used the same reference reflector used to adjust misties. I tracked a horizon represented by the reference reflector, first on the legacy data and then on Phase I data, using maximum positive reflections, as shown in figure 2.6, where the horizons are colored by two-way traveltime. These times are in good agreement, suggesting that temporal and spatial alignment had been done with a reasonable accuracy.

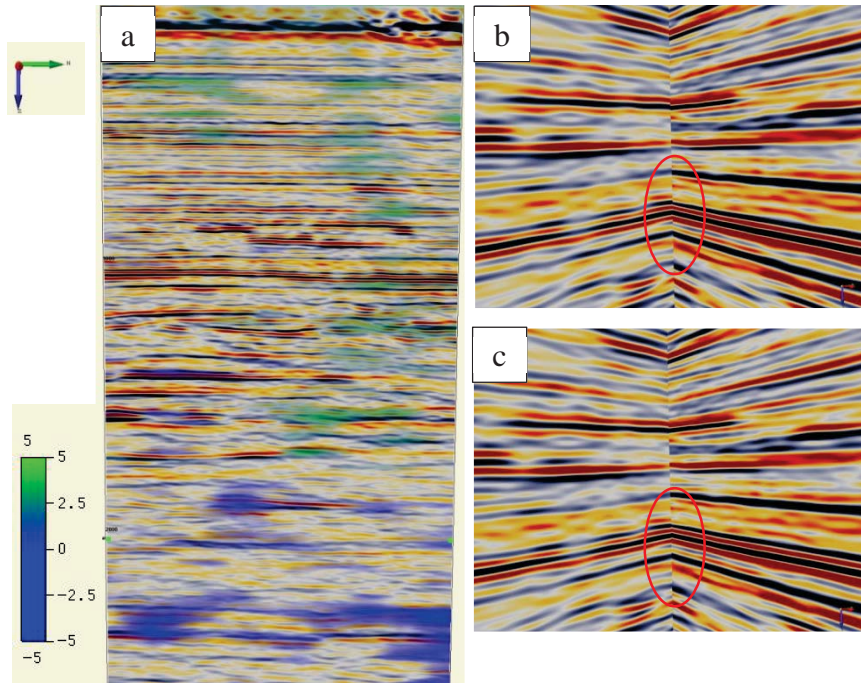


Figure 2. 5. Residual mistie between legacy and Phase I data. (a) Crossline 6005 displaying residual mistie (green and blue) between the legacy data and the time-lapse data on a seismic section displaying seismic data from the legacy survey. Legacy data are used as reference. Maximum allowable shift is 10 ms. Green color marks location of delayed arrivals and blue color marks the early arrivals of time-lapse reflections as compared to legacy reflections. Note that there is no constant shift needed any more. (b) A display of crossline 6005 (left) and inline 3528 (right). Legacy data is displayed on crossline 6005 and Phase I data after initial corrections is displayed on the right. Note the mistie circled in red. (c) Same display as displayed in figure 2.4 (b), but now inline 3528 display data after residual correction, such that the data are now better aligned.

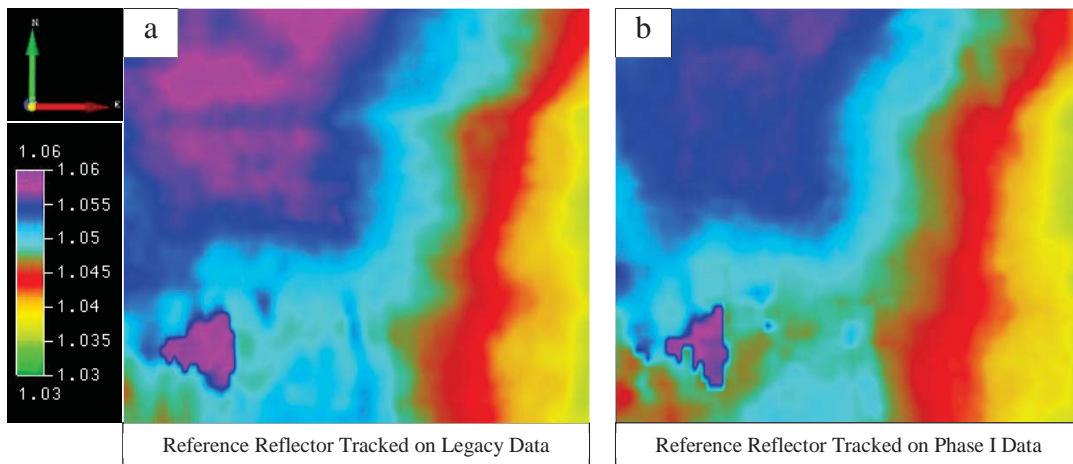


Figure 2. 6. Reference reflector tracked on legacy data (a) and Phase I data (b).

Amplitude differences between the two data sets depend on the spreading correction, gain, NMO corrections, deconvolution, and migration velocities that have been applied. Here we seek to use a simple linear scaling factor, recognizing that this may be a great

simplification. A cross plot of amplitudes from Phase I and legacy data is shown in Figure 2.7(a), representing data from the reference horizon only. The slope of the best-fit curve suggests a multiplication factor of 2650 and y-intercept of 12000 (to be applied to the legacy data). Logically, both data sets should converge to zero so y-intercept should be zero. Fixing y-intercept at zero gives a slope of 4800 for the best fit. Further, a histogram was prepared by taking a ratio of amplitudes of Phase I data to that of legacy data and is given in Figure 2.7(b). The histogram proposes a value of 4500. I used 4500 as calibration factor to translate legacy data into time-lapse equivalent.

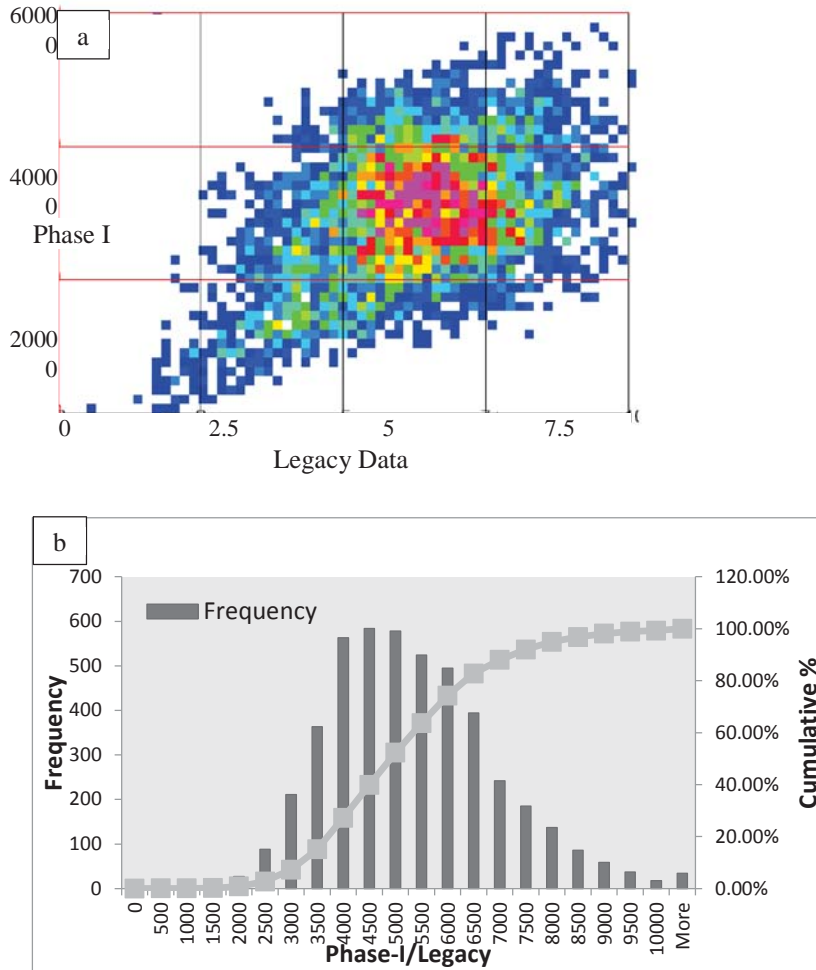


Figure 2. 7. Amplitude equalization between legacy and Phase I data. (a) Crossplot between the amplitude of reference reflector (shown in Figure 2.5) from legacy data and from Phase I data. The color represents the density of the points [highest density=pink, lowest density=blue]. Note that cell with highest density corresponds to almost 30000 on Phase I data and 6 on legacy data, it suggests a Phase I to legacy ratio of about 5000. (b) A histogram of amplitude ratio between Phase I and legacy data. Histogram peaks between 4000-5000.

Amplitude balancing based on energy is considered the simplest possible approach (Rickett and Lumley 1998). To see the effectiveness of amplitude equalization, I plot the energy of time-lapse data against the energy of calibrated legacy data (Figure 2.8 (a))

throughout the entire volume, not just the reference horizon. A similar plot, but using instantaneous amplitude, is given in Figure 2.8(b). The red lines in these plots show desired output with perfect correlation. The data points below red line indicate over-prediction and above this line under-prediction. A multiplication factor of 4500 over-corrects most of the legacy data, especially the data with low amplitudes. The reference reflector selected for establishment of the scaling factor is very strong in magnitude and will not represent weak reflections properly.

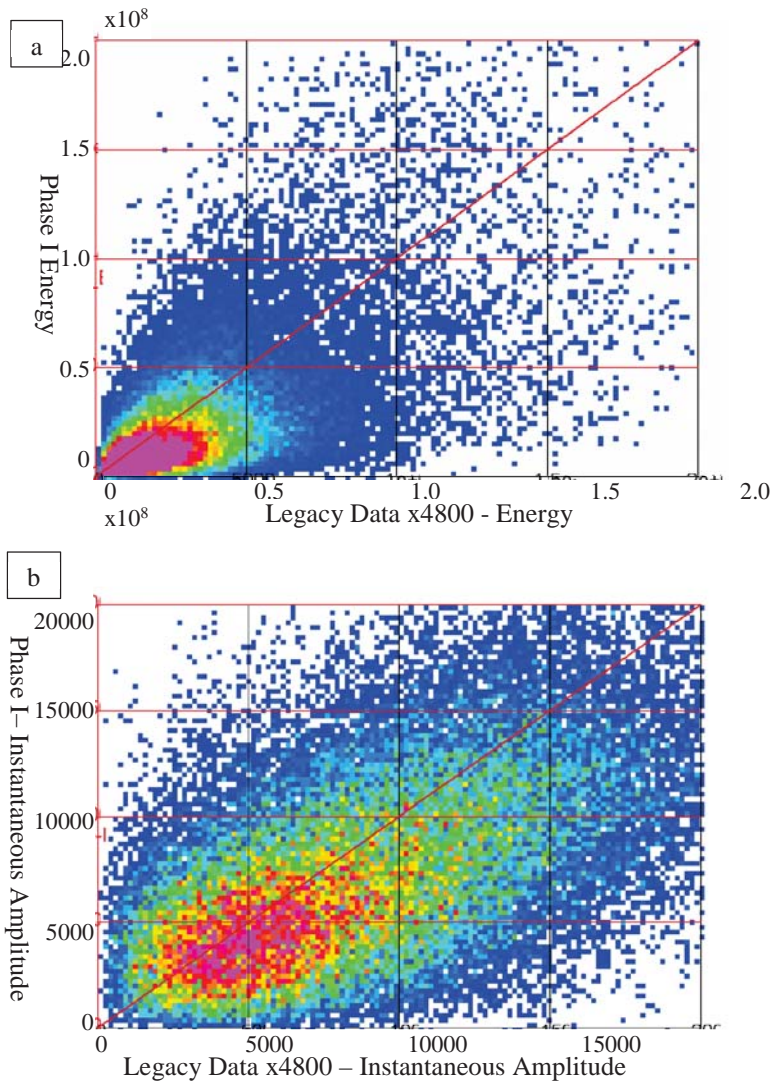


Figure 2. 8. Crossplots between legacy data (after amplitude equalization) and Phase I data throughout the volume. (a) A plot of energy of Phase I data versus energy of legacy data. (b) Plot of instantaneous amplitude computed from Phase I data with instantaneous amplitude computed from legacy data. Along the red diagonal lines, the legacy data match with the Phase I data. Points below these lines are over-corrected and above this are under-corrected. The color here shows the density of the points. Pink color shows highest density and blue color shows the lowest density. The legacy data amplitudes were multiplied with 4800 to match with Phase I data. Note that 4800 has overcorrected the legacy data especially at low amplitudes.

In order to choose a multiplication factor that is a representative for most of the data, a wider range of the data was used rather than one horizon only. The time-lapse data were processed focusing on reservoir 'A' and neighboring reservoirs so reflections below 4500-ft sand and at the edges of the survey are poorly processed. A cube ranging inline 3490-3540, crossline 5940-6030 and two way travel time of 500-1500 was used for revised amplitude analyses. This cube includes some portion of reservoir A and all of reservoir B. A histogram of the amplitude ratio from Phase I to legacy was prepared for this cube and is shown in Figure 2.9. Most of the reflections in this cube suggest a ratio of 2000-4000.

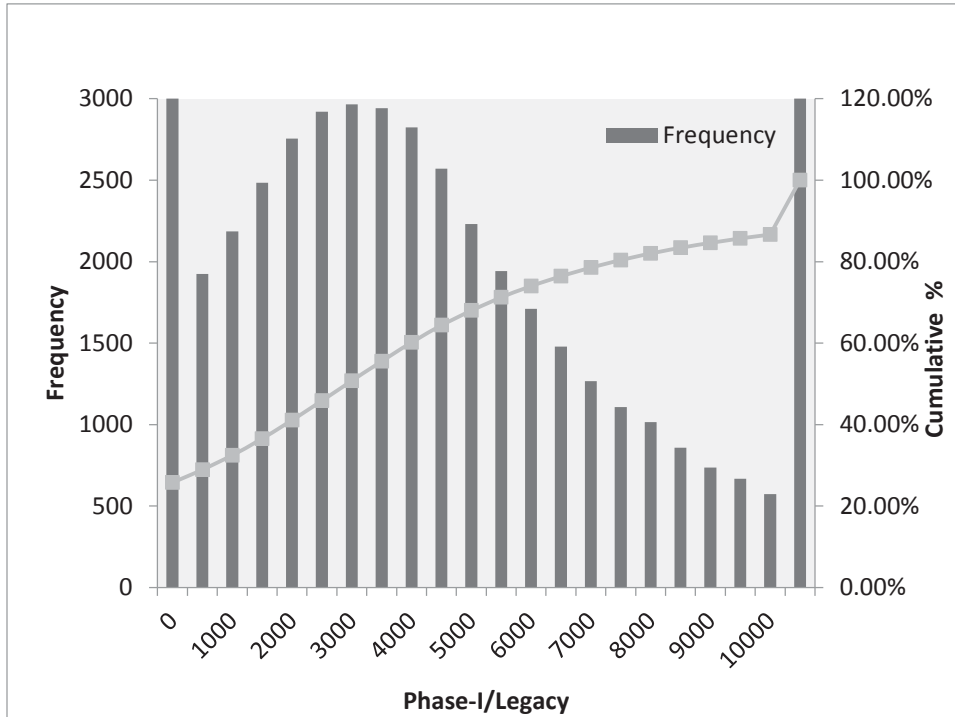


Figure 2. 9. Histogram presenting Phase I /legacy ratio. The data points are randomly picked from inline ranging 3490 to 3530, crossline ranging 5940 to 6030 and TWT ranging from 500 to 1500ms. Histogram peaks between 2500-4000.

A range of values were tested between 3000 and 4800. A multiplication factor of 3800 is selected as it gives the best results for whole data. Figure 2.10 shows crossplots between Phase I and legacy data using the energy attribute and the instantaneous amplitude using 3800 as the amplitude multiplication factor. Subsequent analyses use this scaling factor.

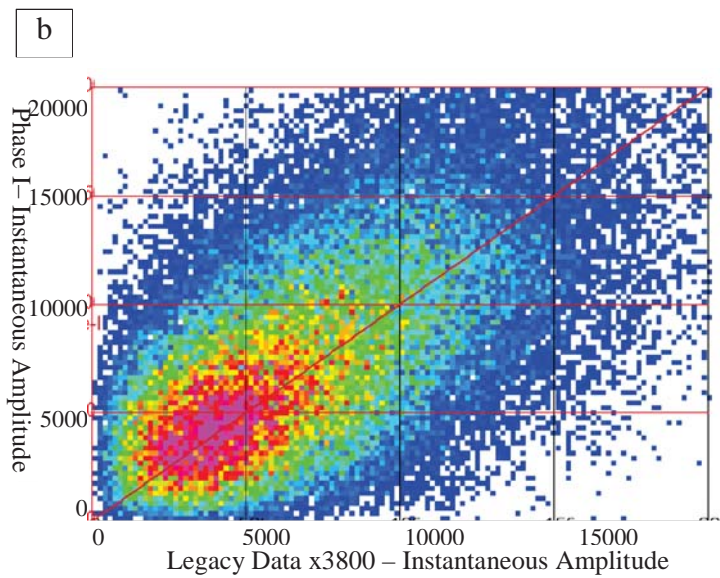
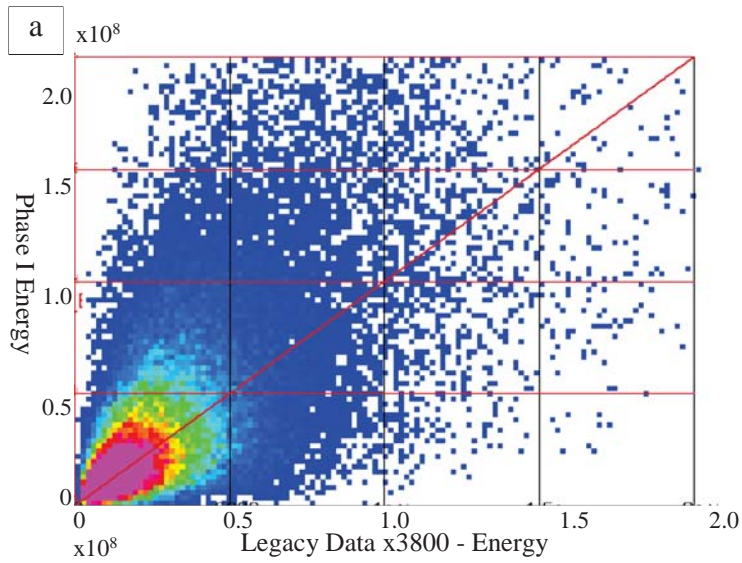


Figure 2. 10. Crossplot between legacy and Phase I data after cros-equalization. (a) A cross plot between energy attribute computed from Phase I data with energy attribute extracted from legacy data multiplied with 3800. (b) A crossplot similar to Figure 2.9 (a) but using instantaneous amplitude as an attribute. The data points are randomly picked over the same range of data as used for Figure 2.7. Note that these plots show a slight under-correction but the histogram shown in Figure 2.10 show slight overcorrection.

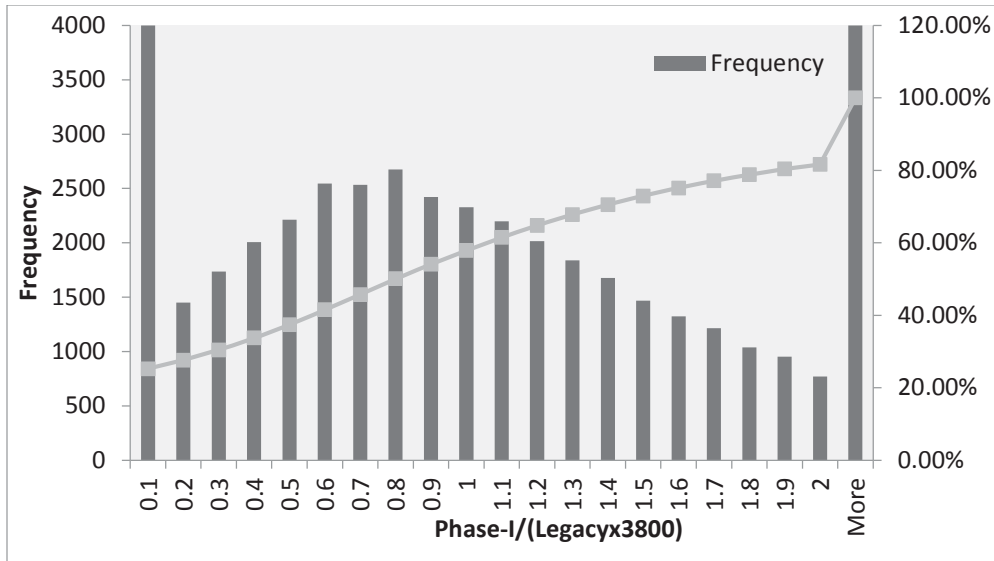


Figure 2. 11. A histogram of ratio between Phase I amplitude and legacy amplitude corrected by multiplication factor of 3800. Histogram peaks at 0.8, although the desired output was 1.0. Histogram suggests slight over-correction but plots in Figure 2.9 suggest slight under-correction.

In addition to equalizing amplitude, frequency equalization is also an essential component. The two data set types were acquired using different sources, receivers, and survey geometry, and then processed independently, so it is important to adjust the frequency components of both data sets.

The time-lapse data contain higher frequencies than the legacy data. A low-pass filter of 50Hz dropping off at 2dB/octave was included as part of the amplitude equalization; all of the amplitudes and attributes (legacy as well as time-lapse data) displayed in the previous figures had been filtered with a 50Hz high cut filter. An example of amplitude spectra from legacy and Phase I data is shown in Figure 2.12, after amplitude scaling. The two spectra match very well at all frequencies except at very low frequencies where the Phase I data drop off at about 10Hz while the legacy data extend to about 5Hz. I chose not to apply a low-cut filter to either data set.

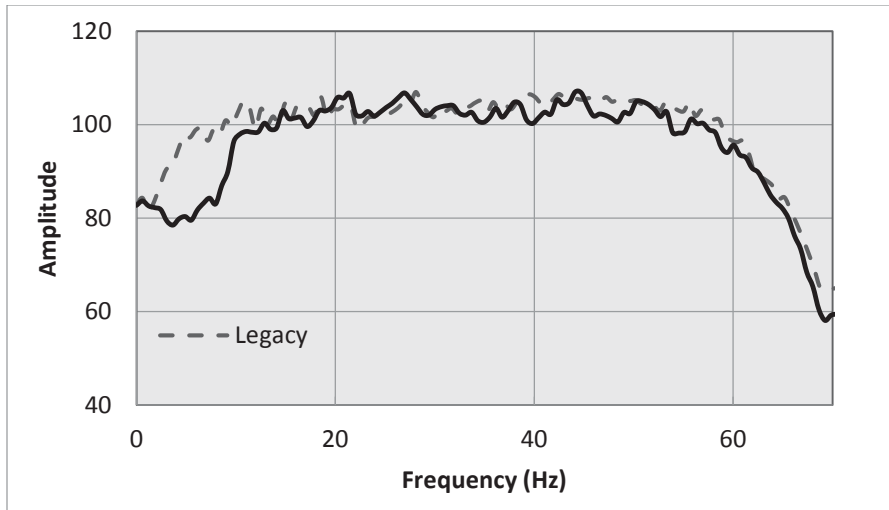


Figure 2. 12. Amplitude spectra for Phase I data (solid line) and legacy data (dashed line), both are filtered by a low pass filter of 50Hz. The filter slope is 2dB /Octave. Legacy data has been equalized in amplitude with the Phase I data. The amplitude spectra are prepared for inline 3513. Legacy data for this particular line shows that Phase I data are a little deficient in low frequency components. I have not applied any low-cut filter as it may filter-out some important data. The amplitude spectra vary a little bit from line to line.

### 2.3.3. Cross-Equalization of Time-Lapse Data for Phases I and II

In the previous sections, I described processing to match legacy data and Phase I data. In contrast to legacy data, the two time-lapse data sets (Phase I and Phase II) were acquired with the intent to investigate the production-related changes in the 4500-ft sand, and the parameters were kept constant during both phases of data acquisition and processing as much as possible.

In order to evaluate the temporal and spatial alignment between the Phase I and Phase II data, a 'delta' attribute is computed similar to legacy data with maximum allowable shift of 6 ms. Output from the analysis is given in Figure 2.13 in the form of a histogram. It shows that most of the time-lapse data are well aligned and there is no major time-shift necessary. However, at some locations, a small mistie of two-way traveltime is observed between the Phase I and Phase II data. Most of these differences range between 1 and 3ms, less than the sampling interval (4 ms) for this processed data. The error is small and appears to be random. When I smooth the 'delta' function, it becomes negligible. No correction is applied as a result.

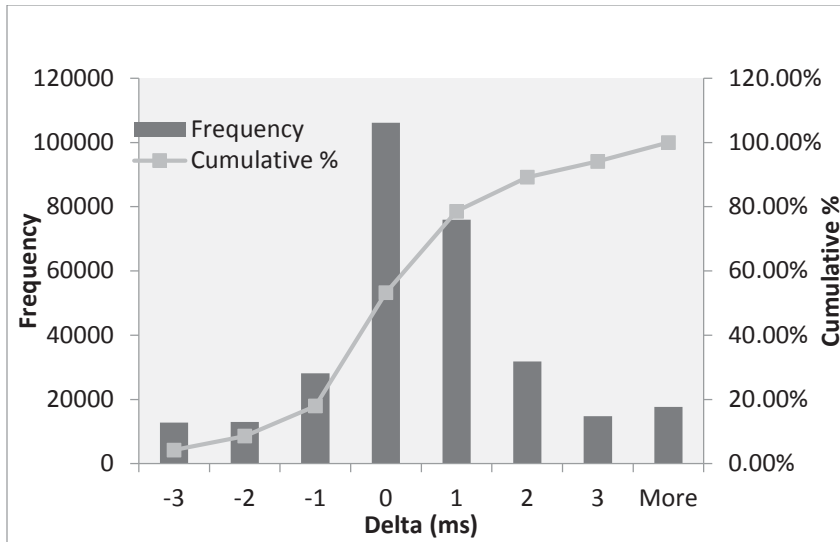


Figure 2. 13. A histogram of travel time-shifts between Phase I and Phase II data. Phase I data are set as reference data and maximum allowable shift is 6 ms. Histogram peaks at 0 ms, indicating that most of the time-lapse data are matched perfectly. However, there are small occasional time-shifts present in the data that should be considered while interpreting time-lapse changes.

The energy attribute and instantaneous amplitude attribute are again used to evaluate the accuracy of amplitude equalization of time-lapse data. These show that time-lapse data had been equalized extremely well, and any significant changes observed should be associated with the production process.

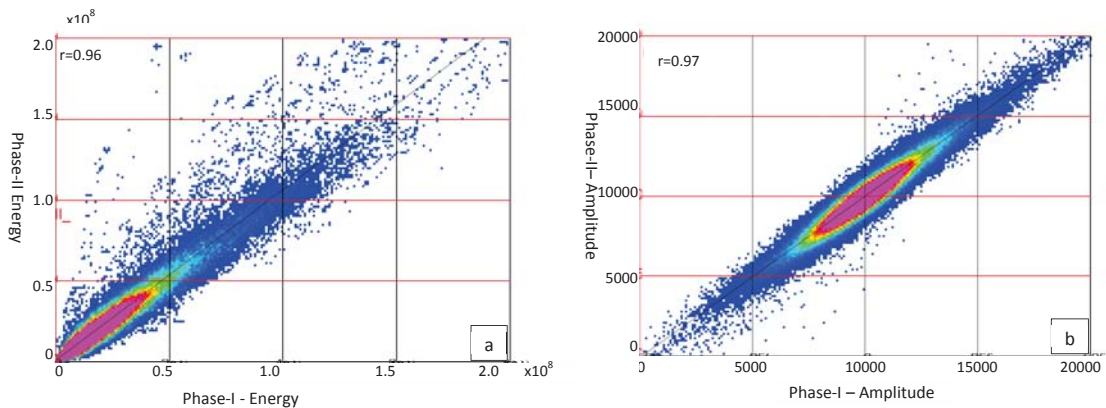


Figure 2. 14. Crossplot between Phase I and Phase II data. (a) A plot between the Phase I energy attribute and Phase II energy attribute at different sampling points. Figure shows that most of the data points show equal energy at Phase I stage and Phase II stage. (b) A crossplot between Phase I amplitude and Phase II data amplitude. The plot indicates that both data sets have almost equal amplitude at most points. The figure suggests that Phase I and Phase II data are well equalized.

Amplitude spectra for Phase I and Phase II data are presented in Figure 2.15. Time-lapse data show an excellent match in frequencies between Phase I and Phase II.

At this point, I conclude that time-lapse data have already been processed appropriately to suppress the background noise and non-production related changes between Phase I and Phase II data. On the other hand, legacy data were equalized as described previously to match the Phase I data. Care should be taken while interpreting legacy and Phase I data to investigate the production induced time-lapse changes because of the inherent limitations of that cross-equalization. My analysis may give reliable qualitative results but can not be relied on to give quantitative results between the legacy and the time-lapse data sets.

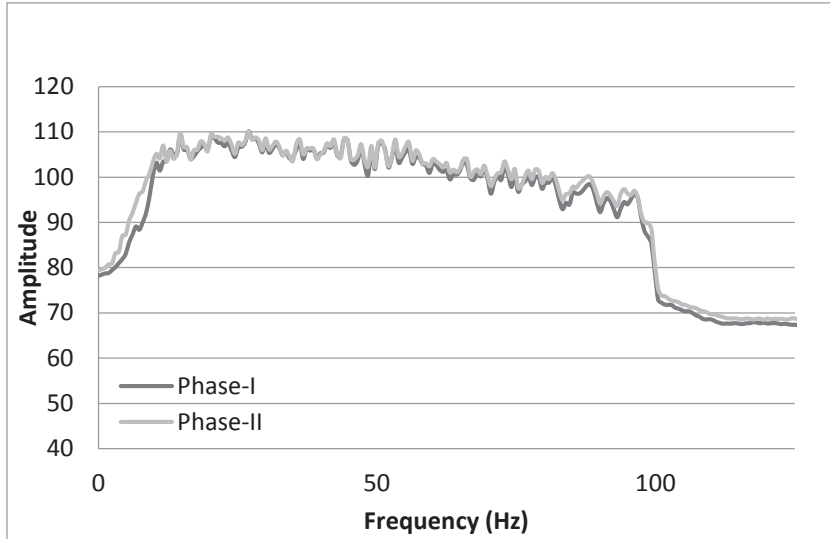


Figure 2. 15. Amplitude spectra of Phase I and Phase II data. Both data-sets show exactly similar behavior in amplitude spectra and have same range of frequencies. No filtering is required to match the frequency content of Phase I data with Phase II data.

## 2.4. Time-lapse Observations of Seismic Amplitudes

To analyze time-lapse changes in the Teal South, I used squared instantaneous amplitude. Instantaneous amplitude is a measure of the reflection strength at every sampling point. It is estimated by complex trace analysis, and provides a good estimate of the overall size of a signal, regardless of zero-crossings within a complicated signal.

In 1970s after the discovery of ‘brightspots’, it was soon realized that the apparent ‘brightness’ of reflections depends on many factors other than geology. Because of a reflection’s polarity and phase, ‘brightspots’ often remain un-recognized (Barnes 2007) and instantaneous amplitude provides a direct measure of reflection strength that is independent of phase and polarity. In the early 1970s, Anstey discovered that the trace-envelope is a good measure of the reflection strength (Barnes 2007). A trace envelope connects peaks of a seismic trace and indicates the maximum possible reflection strength a trace can have given a constant phase rotation. Taner, Koehler, and Sheriff (1979) used the Bracewell (1965) description of the analytic signal together with Anstey’s idea of

reflection strength and proposed a method of reflection strength computation by using the complex number description of a trace. They named it “complex seismic trace analysis”. In complex trace analysis, a seismic trace ‘x(t)’ is rotated by  $-90^\circ$  using the Hilbert transform y(t). The two traces (seismic trace and its Hilbert transform) are then combined as the real and imaginary part of a time-varying function ‘R(t)’, named ‘Instantaneous Amplitude’, defined by:

$$R(t) = [x(t)^2 + y(t)^2]^{1/2};$$

The phase rotation needed to rotate the trace to its maximum is called ‘instantaneous phase ( $\phi(t)$ )’, and is given by:

$$\phi(t) = \arctan\left[\frac{y(t)}{x(t)}\right];$$

The output from complex seismic trace analysis is a set of instantaneous amplitude and instantaneous phase for each time sample. Many other attributes are then derived from these two. For example, instantaneous frequency is then defined as the rate of change of instantaneous phase.

$$f(t) = \frac{1}{2\pi} \left[ \frac{d\phi(t)}{dt} \right]$$

Instantaneous amplitude, by definition, is the trace envelope that is defined as slowly varying function of time that connects the peaks of seismic trace, and by design it measures the reflection strength at any sampling time. Instantaneous amplitude brings out the bright reflections by highlighting them and reduces complications due to thin beds and a finite wavelet. Instantaneous amplitude has more power to resolve the reflectors than seismic trace (Zhang and Bentley 2000). Being a direct measurement of reflection strength, instantaneous amplitude can readily identify time-lapse changes in amplitude caused by saturation or pressure change during production. In this study, we use the square of instantaneous amplitude in order to better emphasize (visually) the large-amplitude changes and to reduce the visual clutter from low-amplitude changes, which may be related to noise and lack of repeatability; the same goal could have been achieved through the use of a non-linear color scale.

The Teal South oil field is characterized by typical ‘brightspots’. Low impedance water-sand is underlain by high-impedance shale. In the reservoir, oil replaces most of the water in the pore spaces. The presence of oil (or gas) reduces further the acoustic impedance of the sand, and in turn generates brighter reflections over the oil (gas) zone compared to the surrounding rocks.

Earlier studies concluded that at the time of discovery the 4500ft-sand was an oil reservoir with no free gas; the reservoir pressure and temperature were close to bubble point. With the start of production, the liquid oil in the pores expanded, slightly

decreasing the bulk density and compressional velocity of the medium, while the reservoir experienced liquid expansion drive. As the production continued, the reservoir pressure decreased and quickly dropped below bubble point. At this pressure, gas started coming out of solution, perhaps developing a gas cap while increasing gas saturation in the oil zone. The addition of gas in the pores caused a sudden and significant drop in bulk rock modulus and the velocity dropped. This decrease in velocity decreased the reservoir impedance even more, enhancing impedance contrast at the interface so reflections after the release of free gas become even brighter than they were upon discovery.

Due to the reduction in overall reservoir fluid volume caused by production of fluids through the well, water from surrounding sands likely encroached into the reservoir. The replacement of oil with water in the pores increased the density and seismic velocity of the medium, thereby increasing the acoustic impedance of sand where water has encroached. The increased impedance 'dims' reflections from the reservoir because of reduced impedance contrast at the interface.

The 4500-ft sand is composed of unconsolidated sands of very high porosity (39%) that were strongly over-pressured at the time of discovery (~0.65 psi/ft). Due to the high pore volume and poor grain-to-grain connections, the acoustic velocity in this type of sand can be strongly dependent on the pore-fluids. The Teal South reservoir was expected to deplete quickly, and the time-lapse changes from the Teal South reservoir were expected to be quite pronounced.

The effect of frame-stiffening due to a reduction in pore-fluid pressure during production will result in a different observation: production will result in an increase in bulk modulus of the rock frame (as the grains become more intimately in contact with each other), and the acoustic impedance of the overall rock, occupied with fluids including gas, may decrease with extended production (see Pennington, et al., 2001, and chapter 3 of this dissertation for details). Because the frame-stiffening effect also reduces Poisson's ratio during extended production, we can expect that the stacked seismic traces (over the angle ranges present in the Teal South data) will result in a continued brightening as production continues over the life of the time-lapse experiment. Thus, although the zero-offset amplitudes may be expected to decrease slightly during extended production (after gas has come out of solution), the stacked result should show continued brightening during production in the oil (gas) zones as a result of strong brightening at offsets, while the water-encroachment zone should show dimming over time on stacked data.

Because instantaneous amplitude is a direct measure of (stacked) reflection strength, the difference between instantaneous amplitudes of seismic data recorded after different periods of production should exhibit these changes. Fluid expansion and release of free gas is identified by an increase in instantaneous amplitude, and water encroachment is identified by a decrease in instantaneous amplitude of stacked seismic sections. In order to emphasize the large-amplitude changes, squared instantaneous amplitude is used here.

In addition to difference in reflection strength ‘semblance’ is used to delineate the faults associated with the reservoir. Semblance is a measure of the coherence or similarity between neighboring traces that quantifies how similar the two traces are; values range from zero for no similarity to 1 for identical traces. When there is a fault in the region, at any particular depth the reflections across the fault will be different and the semblance will be low; plots are usually shown with dark colors for low values of similarity (semblance) and light colors (white) for high values.

In its simplest form, coherence is defined by computing the cross-correlation coefficient of a small windowed portion of a seismic trace against its neighboring traces in the inline and crossline directions. Semblance is computed across a group of traces in a small data volume using smaller time windows, thus giving finer depth resolution than coherence and is a bit less sensitive to trace-to-trace noise. In the following discussion, the terms are used interchangeably, but semblance was used in all of the computations.

I use semblance to delineate the faults on time slices. The faults may then be related to time-lapse changes to define the pressure communication between the reservoirs reported in previous studies (Pennington et al. 2001, Ezawi, Pennington, and Islam 2012).

#### **2.4.1. Methodology**

Instantaneous amplitude was computed from all the three seismic data-sets (legacy data, Phase I data and Phase II data) available from Teal South. Instantaneous amplitude was then squared, and a difference of squared instantaneous amplitude was computed generating two separate volumes: one from legacy to Phase I (Phase I – Legacy), and second from Phase I to Phase II (Phase II-Phase I). These differences are then displayed on the time slices and in volume displays using minimum values for opacity cut-offs.

In addition to instantaneous amplitude, semblance was used to define the faults on time-slices. A semblance cube was computed by using a time window of -28ms to 28 ms. Because the data display minor temporal misalignments, every time-lapse change described here was confirmed with the wiggle-trace display on the respective inlines and crosslines.

#### **2.4.2. Results and Discussion**

There are many small reservoirs in the 4500-ft sand; in this work I focus only on three main reservoirs (A, B and C) shown in Figure 2.16 and one “tiny” reservoir identified later. First, I discuss the time-lapse changes for each reservoir independently and then will examine how all these reservoirs are associated with each other, including the “tiny” reservoir at that point. For clarity and simplicity, the difference volume covering the time from legacy to Phase I will be referred as the legacy difference, and the difference cube from Phase I to Phase II will be referred as the time-lapse difference.

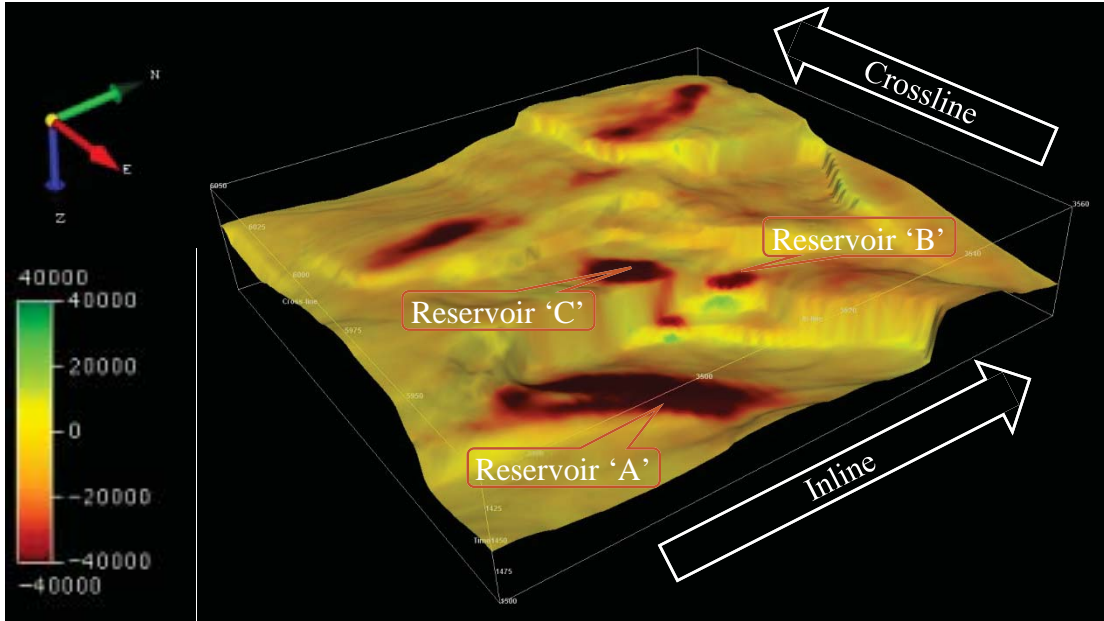


Figure 2. 16. A horizon tracked over the 4500-ft sand. The horizon has been smoothed by applying a median filter. The color scheme shows the seismic amplitude recorded in Phase II data. Note that the 4500-ft sand exhibits typical 'brightspots'. There are many small reservoirs visible on this horizon, this work focuses only on three reservoirs labelled in Figure as reservoir A, reservoir B and reservoir C. Only reservoir 'A' is under-production but the other two reservoirs exhibit time-lapse changes indicating pressure communication across faults. The sides of the portion of the survey shown here are about 5550 m in length. The survey box limits are: z-axis 1400-1500ms, inlines 3470-3560, and crosslines 5920 to 6050.

#### 2.4.2.1. Reservoir 'A'

Reservoir 'A' is the only producing reservoir in the 4500-ft sand, and was the initial target for the ERCH-consortium time-lapse studies. Figure 2.17 shows the three-dimensional structure of reservoir A, visualized by using the time-lapse difference volume (of squared instantaneous amplitude) and applying an opacity cut-off value of  $5e+008$ . A time-slice at 1480ms is added to the structure to aid in visualizing the geometry of the north-dipping body.

Figure 2.18 shows time slices at 1480 ms from the legacy difference volume and from the time-lapse difference volume. Both time slices are overlain by the semblance slice computed from the legacy data, displayed with 50% transparency. Red and yellow colors on difference-slices represent an increase in post-stack reflection strength (due to fluid expansion, release of gas from solution, and the frame-stiffening effect), and blue color represents dimming of reflections (presumably due to water encroachment). The lower semblance values (black) correspond to the most likely locations of faults.

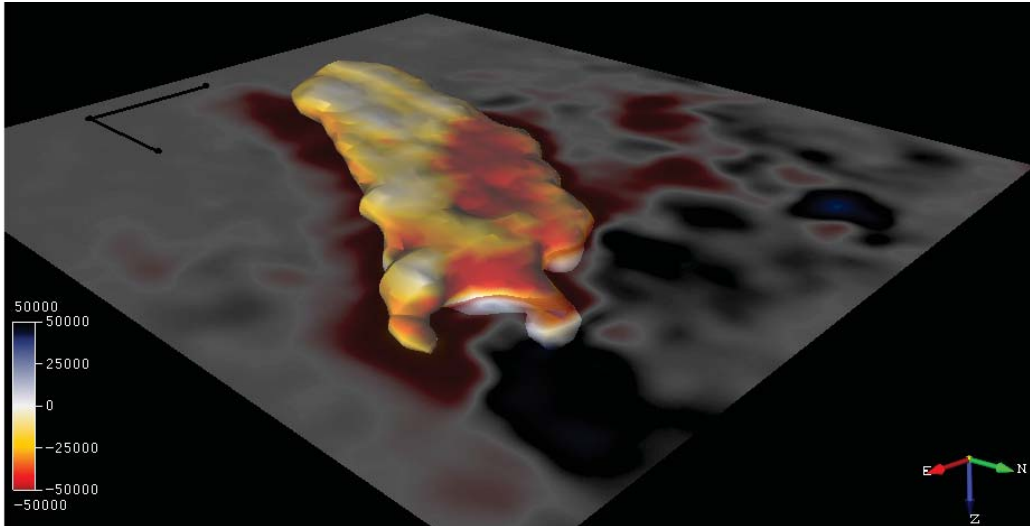


Figure 2. 17. A 3D structural view of reservoir A. Reservoir body was created using the time-lapse difference volume by displaying only points that exhibit a time-lapse difference of  $5.0e+008$  (difference of squared instantaneous amplitude) or higher. Reservoir body is colored according to the Phase II seismic amplitude. 1480 ms time-slice is added to help visualize the structural trend. The reservoir is dipping towards the north-northwest. Two perpendicular black lines at the left corner of the figure mark 500 ft length in their respective directions.

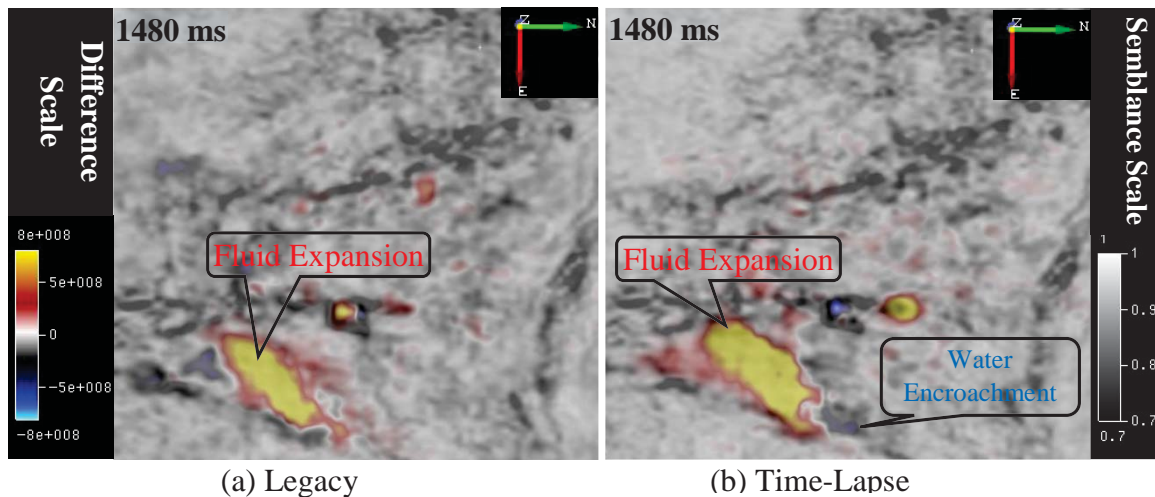


Figure 2. 18. Time slice 1480ms displaying difference in squared instantaneous amplitude from legacy to Phase I (a) and Phase I to Phase II (b). The difference slices are overlain by the semblance plot (grey scale) to show regional orientation of faults, displayed with 50% transparency, and computed from the legacy data. Reservoir 'A' exhibits continued time-lapse changes from legacy to Phase II times. From the time-slices it is evident that pore-fluid is continuously expanding and/or gas saturation is increasing from legacy to Phase II represented by increase in reflection strength (reddish-yellow color). Water encroachment from the North of the reservoir is marked by dimming of reflections (blue color) from Phase I to Phase II data, at or near a junction of two faults. Legacy difference data, however, do not indicate any water encroachment.

Reservoir 'A' exhibits time-lapse changes on both difference slices: from legacy to Phase I the reservoir shows brightening throughout the reservoir while from Phase I to Phase II the most of the reservoir brightens but there is some dimming downdip. The brightening

of the reservoir demonstrates continuous fluid expansion and release of solution gas from Phase I to Phase II. The dimming observed on time-lapse difference slice is probably caused by water-encroachment.

Because of the continuous production from reservoir 'A', the reservoir pressure drops significantly between all phases, and the effects observed can be explained by fluid flow as a result. Water from the water sand enters into the base of the reservoir at its downdip end, drawn in by the pressure reduction and replacing some of the volume of the fluid extracted by production. This in turn causes an increase in bulk modulus of the pore-fluid, so increases the bulk modulus of the rock, implying an increase in impedance for the zone of water encroachment. This increased impedance decreases the reflection strength because the impedance contrast between the overlying shale and the 4500ft sand decreases in that area. This decrease in reflection strength appears as a small blue area on the difference slice. Comparison of Figure 2.18(a) with Figure 2.18(b) shows that the water encroachment zone in the time-lapse difference slice appeared as a brightening in the legacy difference slice, suggesting that gas initially came out of solution there, but that oil and gas was probably replaced with water after production continued.

On the other hand, a closer look at the time slices and seismic sections (see Figure 2.19) indicates that this brightening appears along the top of the reservoir at its downdip end, which would be surprising. Figure 2.20 displays Phase I data (blue) over Phase II data (red) in seismic-wiggle format, while the underlying colored density displays the time-lapse difference data, with dimming in blue and brightening in yellow. A close look at the wiggle display suggests that the Phase II data is slightly delayed relative to the Phase I data. The delay is more prominent and apparent further down-dip. The delay could be processing or acquisition artifact but could also be because of reservoir compaction. I locally applied a static time-shift of 1ms to the Phase II data, aligning most of it with the Phase I data, and computed a new difference cube, displayed in Figure 2.21. This adjusted difference cube shows that dimming, and presumably water encroachment, now appears at the bottom of the downdip end of the reservoir.

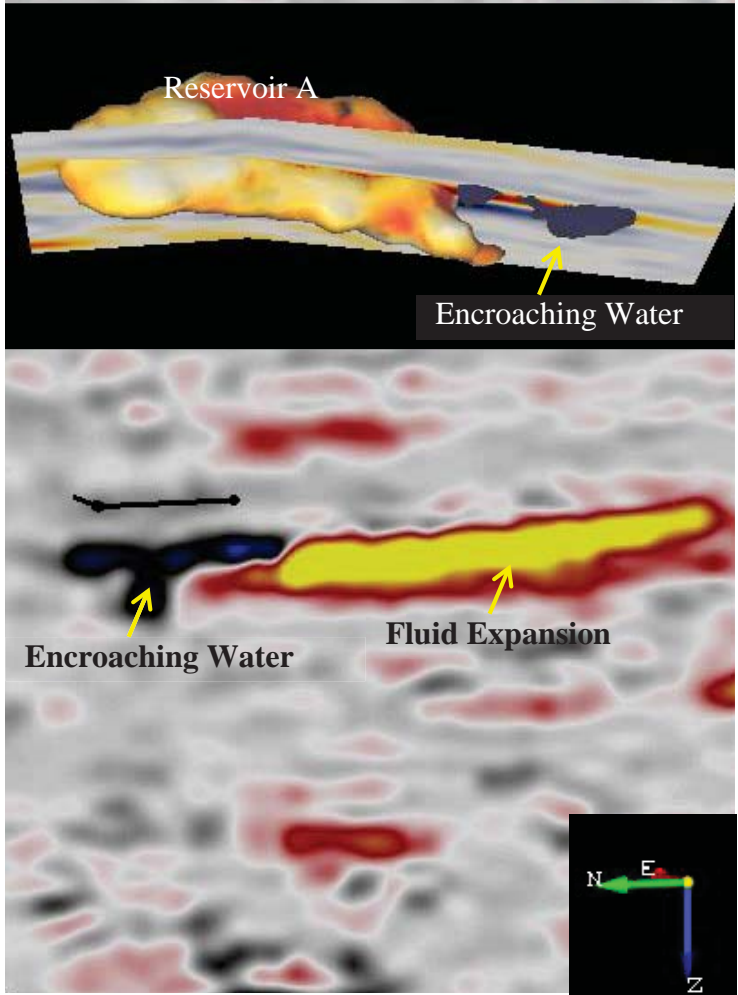


Figure 2. 19. A random line connecting water encroachment with reservoir. The figure at top shows 3D structural view of reservoir A. The reservoir body is colored according to Phase II seismic amplitude. The red color shows strong negative reflection coefficients and yellow color shows comparatively weaker reflections. The dark blue body at the down dip of the reservoir is the dimming observed from time-lapse data that is marked as water encroaching into the reservoir. The 2D line over the body shows the positions of the line displayed at the bottom. The bottom figure shows a 2D random line created connecting the reservoir with the water-encroachment zone. Time-lapse difference is displayed on the section where red and yellow color mark 'brightening' and blue and black color mark dimming. Note that time-lapse data suggest water encroaching along the top of the reservoir which contradicts the basics of fluid dynamics.

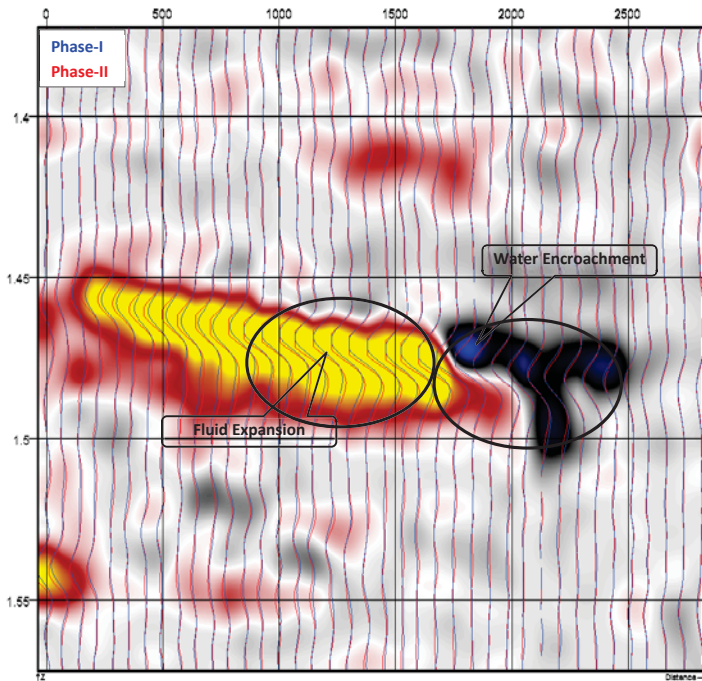


Figure 2. 20. Seismic section displaying the Phase I (blue) and Phase II (red) data in wiggle display on a random line created by connecting the reservoir with the water-encroachment zone as shown in figure (2.19 (top)). In the background, time-lapse difference of squared instantaneous amplitude is displayed. Note the small delay in Phase II data as compared to phase -I data (circled with a red circle). The delay is more prominent at downdip location of the reservoir. It is this misalignment that makes water encroachment to appear at the top of the reservoir.

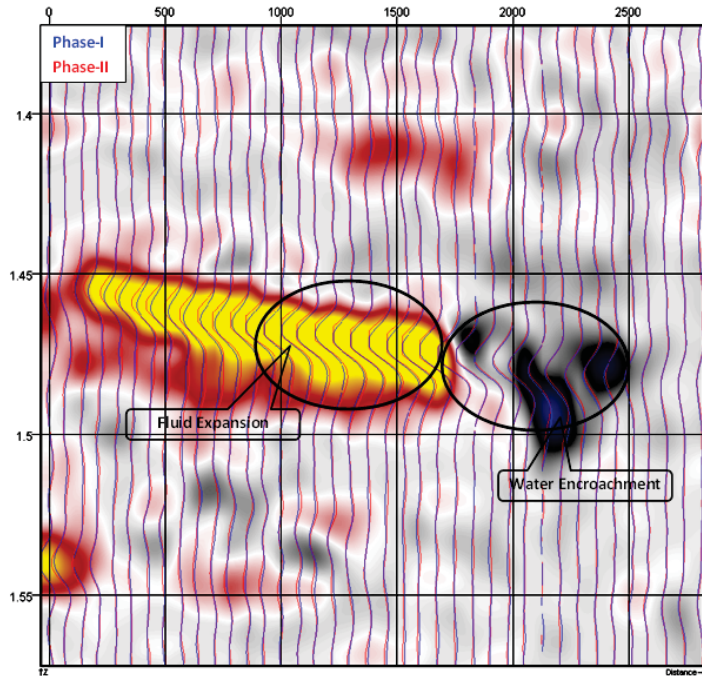


Figure 2. 21. Same section as displayed in Figure 2.20 but Phase II data have been shifted up by almost 1ms. Note that the wiggles are now better aligned. Also note that water now seems to be encroaching at the base of the reservoir.

In summary, Reservoir A shows evidence of gas expansion and water encroachment. Gas expansion is implied throughout the reservoir between the times that the legacy and Phase I data sets were acquired, as indicated by the brightening of stacked data. No evidence of water encroachment is found between legacy and Phase I data. Between Phase I and Phase II, water encroachment appears to have occurred at the downdip NE end of the reservoir, based on dimming observed, particularly after a minor static time adjustment that may be related to reservoir compaction.

#### 2.4.2.2. Reservoir 'C'

Reservoir 'C' is a small reservoir located almost 1450 ft Northwest of reservoir 'A' and is almost 28 ms shallower than reservoir 'A'. The two reservoirs are separated by a N-S trending normal fault. Because of the limited data quality, it is difficult to conclude if both reservoirs belong to same depositional sequences or are two different sand bodies. Remember that the reservoir 'C' is not under production.

It is reservoir 'C' that Pennington et al. (2001) identified as the primary 'little neighbor' in their work and reported to be exhibiting time-lapse changes because of production from reservoir 'A'. They proposed that pressure is most likely being communicated through water sand extending down-dip of reservoir 'A' where they have observed continuity of sands.

The legacy (Phase I – legacy) difference data (for squared instantaneous amplitude) is presented on time-slice 1456 ms in Figure 2.22 (a), and Figure 2.22(b) shows the difference slice for the time-lapse (Phase II – Phase I) data. Both time slices are overlain by 'semblance'. These time slices suggest fluid expansion as production (from reservoir A) starts and continues to Phase I, but from Phase I to Phase II there are negligible time-lapse changes here. (A small dimming on the west boundary of reservoir 'C' on legacy slice is apparently caused by small residual mistie between legacy and Phase I data.)

As we view shallower time-slices we observe brightening of reservoir 'C' in the time-lapse difference data. The first brightening on time-lapse data appears at 1448 ms, almost 12 ms shallower than the lowest brightening observed on legacy data slice, while difference slices at 1444 ms show brightening at reservoir 'C' in both time-lapse difference volumes, as shown in Figure 2.22 (c & d). The time-lapse changes in reservoir 'C' confirm that pressure has been communicated from reservoir 'A' to 'C'.

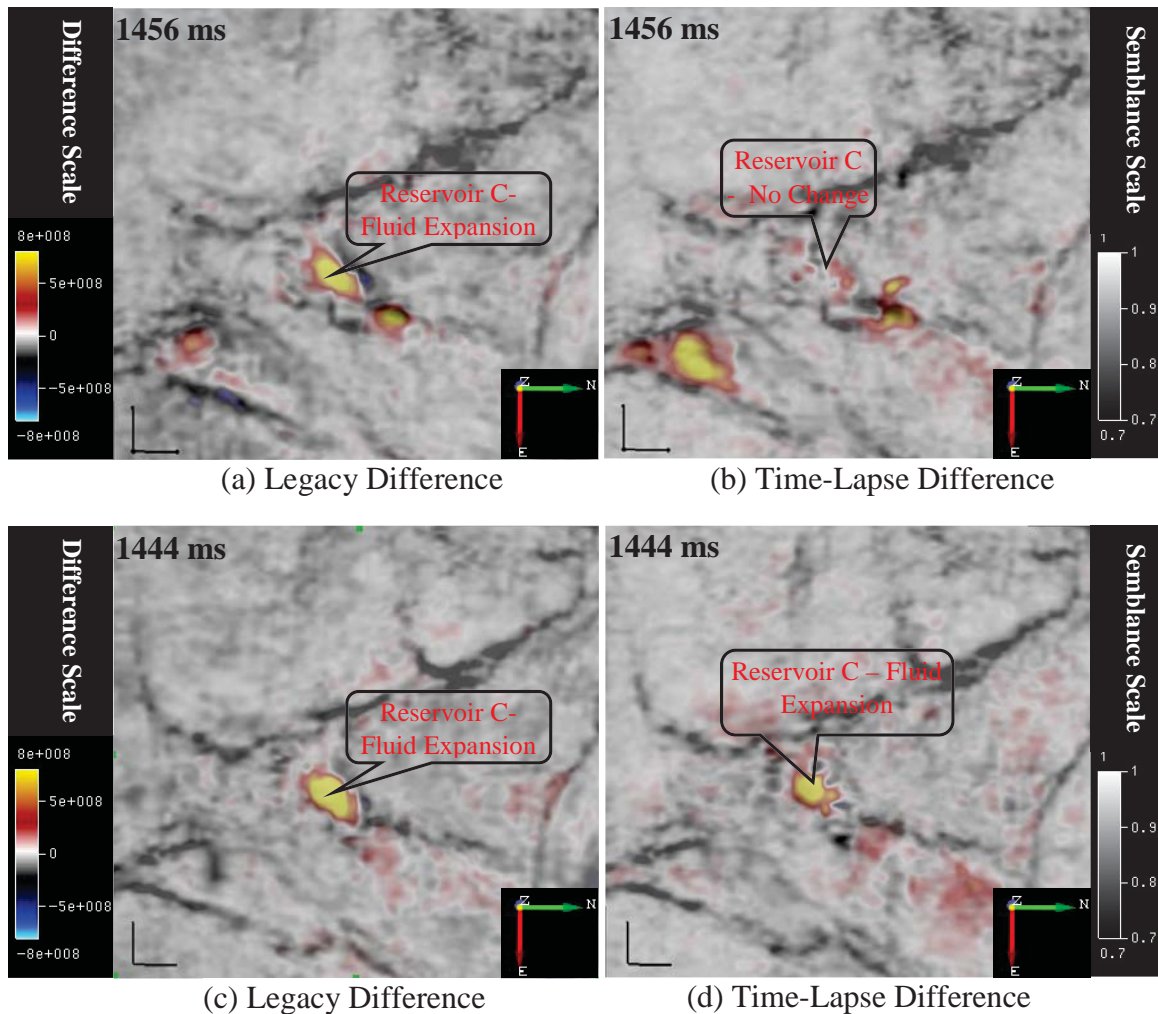


Figure 2. 22. Time slices 1456 (assumed oil zone) and 1444 (assumed gas cap) displaying legacy and time-lapse difference over reservoir 'C'. Note reservoir C is not under production but is being affected by regional 'blowdown' caused by production from reservoir A. (a) Legacy difference at 1456 ms shows that reservoir C brightens between legacy and Phase I. (b) Time-lapse difference at 1456 ms suggest that there is negligible effect of regional pressure drop on the base of reservoir C after Phase I data acquisition time. (c) Like the base of the reservoir the top of the reservoir also exhibits the effects of fluid expansion between legacy and Phase I data. (d) In contrast to the base of the reservoir 'C', the top of the reservoir exhibits fluid expansion from Phase I to Phase II. All the four images together suggest that reservoir C had fluid expansion and release of free gas after the start of production that cause the brightening of whole reservoir between Phase I and Phase II. After Phase I the frame stiffening played a role, and canceled the effect of fluid expansion in oil zone so we do not see any time lapse change at the lower part of reservoir after Phase I, but in gas cap the effect of fluid expansion dominates the frame-stiffness and the upper part of the reservoir shows brightening of the reservoir.

The time-lapse observations from reservoir 'C' suggest that because of regional pressure drop the oil in reservoir 'C' expanded and gas came out of solution between the legacy and Phase I acquisition, appearing as brightening on legacy difference. With further decrease in pore-pressure the gas cap expanded between Phase I and Phase II acquisition generating bright reflections in the shallower levels of the reservoir 'C'. In the oil-zone,

the fluid expansion might have been accommodated by the frame stiffening, as explained by Pennington et al. (2001), resulting almost no-time lapse changes in the oil-zone as evidenced by the stacked data analyzed here. One may argue that the frame stiffening should also affect the gas cap. While our models are insufficiently unique to say with confidence, it may be that the fluid expansion in gas cap dominates over the frame stiffening effect, so we see brightening of gas cap despite the frame stiffening over the angle ranges used for stacking. [In a separate study presented in Chapter 3, I have used rock-physics models and predicted AVO response of Teal South under different reservoir conditions. That work demonstrates that under isotropic conditions the stacked output should exhibit negligible time-lapse response in oil zone when we change pressure conditions from Phase I to Phase II but the gas cap will exhibit significant brightening.]

#### 2.4.2.3. Reservoir 'B'

Reservoir 'B' is another small reservoir located almost 850 ft NE of reservoir 'C' and almost 1450 ft NW of reservoir 'A'. (These distances are given between centers of the reservoirs based on stacked seismic sections.) Reservoir 'B' is separated from reservoir 'A' by the same NS trending fault that separates reservoir 'C' from reservoir 'A'. There is a small NW-SE trending fault that separates reservoir 'B' from reservoir 'C'.

Ezawi, Pennington, and Islam (2012) reported that reservoir 'B' is leaking because of regional 'blowdown'. They used the difference between the squared instantaneous amplitudes of time-lapse data and demonstrated that reservoir 'B' is expanding because of fluid expansion and release of free gas. The limited space available in the reservoir leaves no option for the oil except leaking out from the spill point.

Figure 2.23 presents time-slices at 1460 ms, first exhibiting the legacy difference (Phase I – Legacy) and then the time-lapse difference (Phase II – Phase I), showing continuous brightening of reservoir 'B' after the start of production and demonstrating the pressure communication among reservoirs. Because Ezawi, Pennington, and Islam (2012) only compared the time-lapse differences (Phase II – Phase I), they did not recognize that reservoir 'B' appears to have been water-saturated at the time of the legacy data acquisition – it does not appear as a brightspot on that data set.

Figure 2.24 shows 3D structure of the body of reservoir 'B', extracted by combining data points exhibiting a time-lapse change of  $5e+008$  or more (squared instantaneous amplitude) from Phase I to Phase II. In this figure, however, the body is variously colored by amplitude of seismic data from the legacy survey (a), Phase I survey (b) and Phase II survey (c). This progression of images shows that the body of reservoir 'B' was filled with water before production (evident from the weak reflections on legacy data); as the production started from reservoir 'A' the pressure drop communicated to the neighboring reservoirs. As we have seen in the previous section, Reservoir 'C' was also affected by this regional pressure drop, and the fluid volume of reservoir 'C' increased as gas came

out of solution. This fluid expansion pushed oil down and it escaped from reservoir ‘C’ through the spill point, leading to accumulation in reservoir ‘B’ by the time Phase I data were acquired.

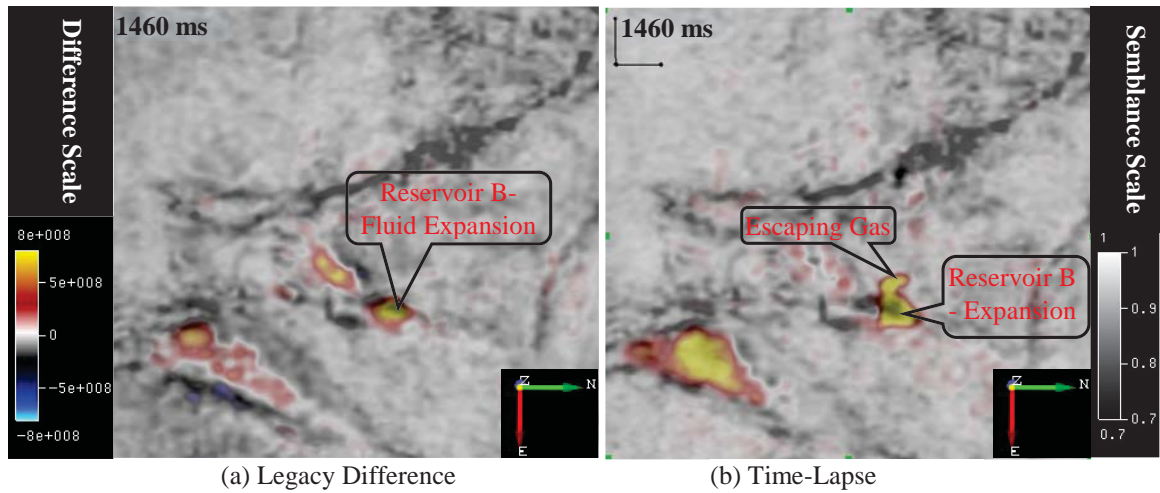


Figure 2. 23. Time slice 1460 exhibiting the effects of regional pressure drop on reservoir B. (a) Reservoir B shows fluid expansion as the production starts from reservoir A and continues till Phase I. (b) As production continues after Phase I oil in reservoir ‘B’ expands even more and gas from solution may have come out. The free gas will need more space than the oil, because of the limited space available to gas, it pushes the oil down and oil starts escaping from reservoir B. The time-lapse difference slice clearly shows the brightening of reservoir and leaked oil.

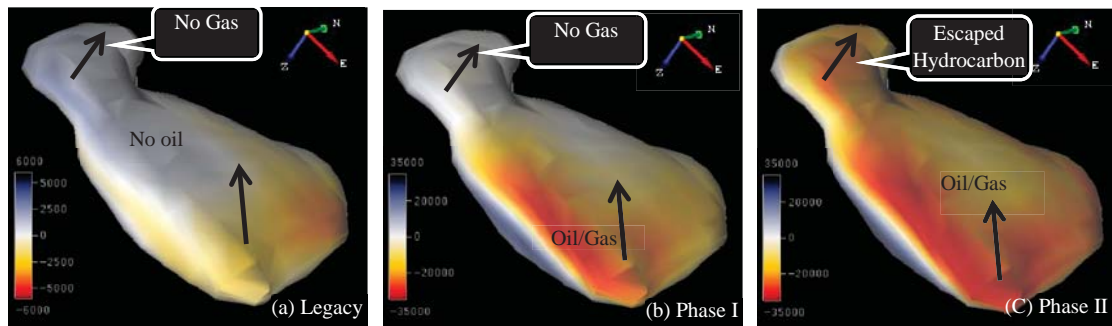
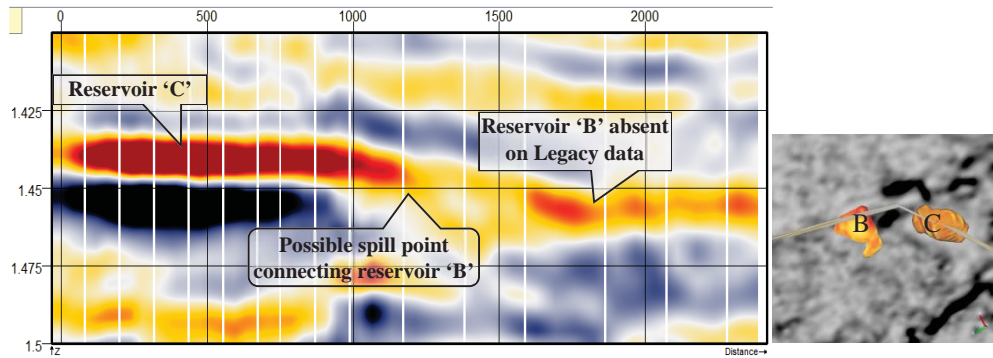


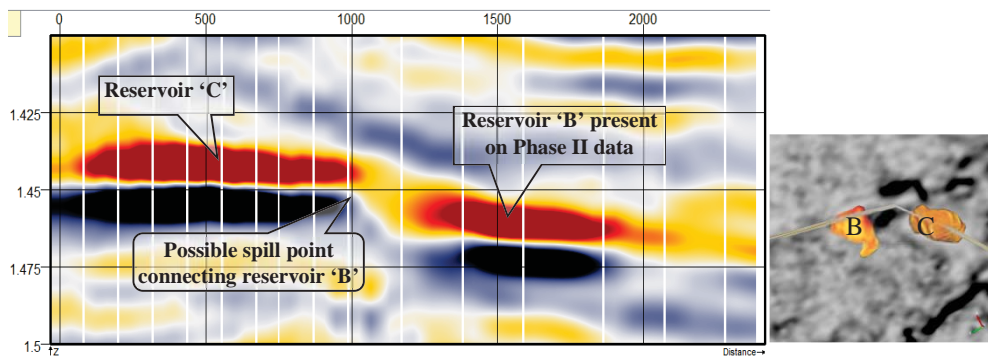
Figure 2. 24. A body of reservoir ‘B’ is presented with all the three seismic data sets acquired over the Teal South oil field at three different times. The body was established by using the time-lapse difference volume and combining all data points indicating an increase of  $5e+008$  in squared instantaneous amplitude from Phase I to Phase II. The black arrows in the figures point in the downdip direction of the reservoir. (a) Reservoir ‘B’ is colored with the legacy data acquired before the start of production. Legacy data suggest that there was no oil present in the reservoir before production. (b) Reservoir body is colored with Phase I data. Phase I data suggest that at the time of Phase I data acquisition some oil has migrated into the reservoir ‘B’ and trapped at the top of the reservoir. (c) Phase II data are displayed on the reservoir body. Phase II data suggest that after Phase I more oil has entered into the reservoir and/or the trapped oil expanded and released solution gas. Because of the limited size of the reservoir ‘B’, the oil started escaping from the reservoir into the neighboring sand where it may be stored diffusely or escape to be lost forever.

Figure 2.25 shows that reservoir ‘B’ is connected with reservoir ‘C’ at its spill point. Oil escaped from reservoir ‘C’ is being trapped in reservoir ‘B’. With continued production the oil in reservoir ‘B’ also expands and releases solution gas, further reservoir ‘C’ may

add more oil volume into reservoir 'B'. Because of the limited volume of reservoir 'B' it cannot store all the gas, and gas start leaking from reservoir 'B' also.



(a) Legacy Data



(b) Phase II Data

Figure 2. 25. Seismic section displaying a random line connecting reservoir 'B' with reservoir 'C'. Small figures displayed at the right of both sections show the location of random line with respect to reservoirs 'B' and 'C'. (a) Legacy data displayed on random line show that reservoir 'B' was not present at the time of legacy survey. (b) Phase II data show the presence of reservoir 'B' at the time of phase-II acquisition. Both reservoirs are separated by a small localized fault. Reservoir 'B' is located just below the spill point of reservoir 'C'. It suggests that any fluid leaking from reservoir 'C' will be stored in reservoir 'B'.

Figure 2.26 shows inline 3523 displaying a possible path for gas escape from reservoir 'B'. The line shows that oil in reservoir 'B' rather than expanding down dip towards the northwest, it expands westward along the top of the reservoir 'B', and from there it escapes through a broken seal or spill point as shown in Figure 2.26.

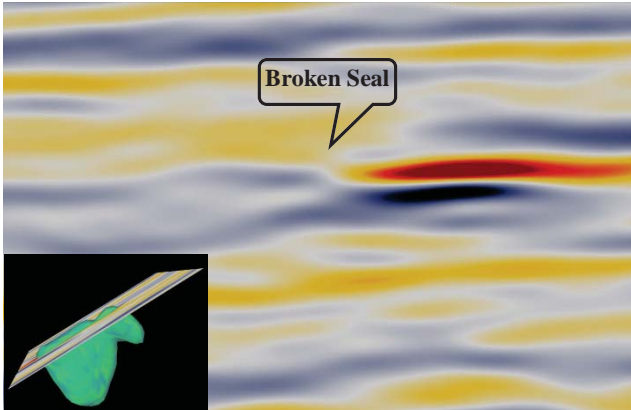


Figure 2. 26. Inline 3523 displaying Phase I data over reservoir 'B'. The figure in the lower left corner shows the position of inline with respect reservoir (looking nearly vertically down to provide perspective). Note the broken seal at local low of reservoir 'B'. Oil/gas seems escaping from here and moving downward in the leaked portion, rather than entering from bottom and rising up.

Figures 2.27 and 2.28 summarize the full path of oil leaking from reservoir 'C'. Oil leaking from reservoir 'C' flows to (water-saturated) reservoir 'B' and starts accumulating there. That reservoir has a broken seal or spill point on the western edge, and oil, after being stored for some period in reservoir 'B' starts escaping to be stored diffusely, at another location, or to be lost forever.

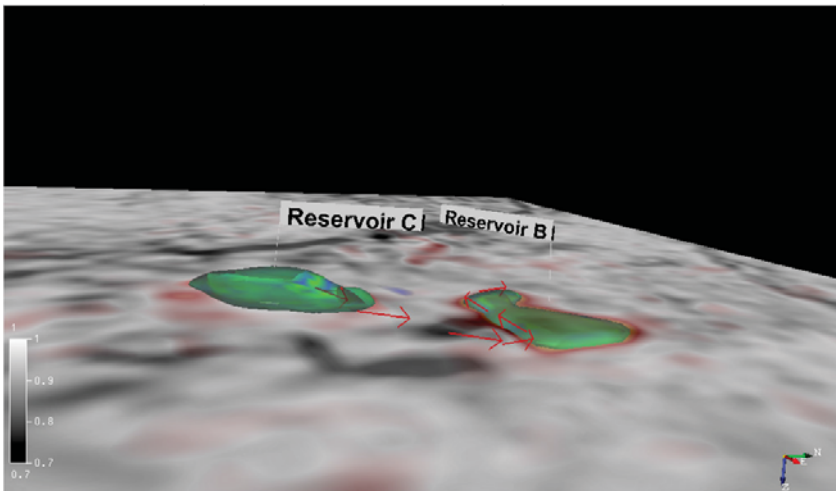


Figure 2. 27. A three dimensional view of most likely leakage path for gas escaping from reservoir C. The red arrows show the leakage path. My analysis of time-lapse data from Teal South suggests that oil in reservoir B came from reservoir C after an initial pressure drop caused by production from reservoir A. Between legacy and Phase I times the oil started migrating from reservoir C into reservoir B. As the production continued after Phase I, oil started escaping from reservoir B following the path along red arrows.

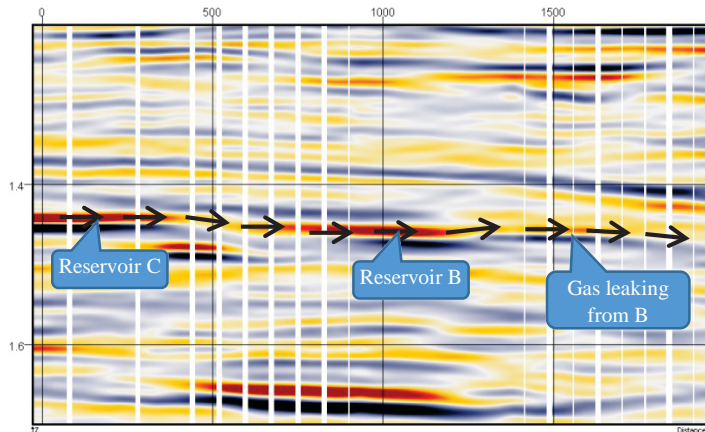


Figure 2. 28. A random seismic line exhibiting the fluid migration path from reservoir 'C' to 'B', generated by joining the arrows of figure 2.27. A complete path of gas leakage from reservoir 'C' is traced using black arrows. Phase II data are displayed on the line. The red color indicates trough and black color show peaks.

#### 2.4.2.4. Regional Pressure Communication Path and the 'Tiny' Reservoir

There is one additional 'tiny' reservoir, surrounded by faults on all sides. This reservoir has been neglected in the various studies to date, probably because of its small size. This reservoir responds to pressure changes in reservoir 'A' on both difference volumes. From legacy to Phase I it shows brightening, but from Phase I to Phase II it dims significantly. The reflections are well aligned as evidenced on seismic sections. The location and structural complexity of this reservoir suggest that any effects of pressure change in nearby reservoirs will be associated with effects in this reservoir.

Figure 2.29 shows one image containing two time slices (1448 and 1480ms) displayed together using transparency. Difference volume is displayed on both slices with semblance volume displayed only on 1480 time slice. The figure nicely shows the location of 'tiny' reservoir with respect to other reservoirs and surrounding faults. The reservoir appears as a local high on seismic sections. Difference slices show that the reservoir brightens from legacy to Phase I and then dims from Phase I to Phase II.

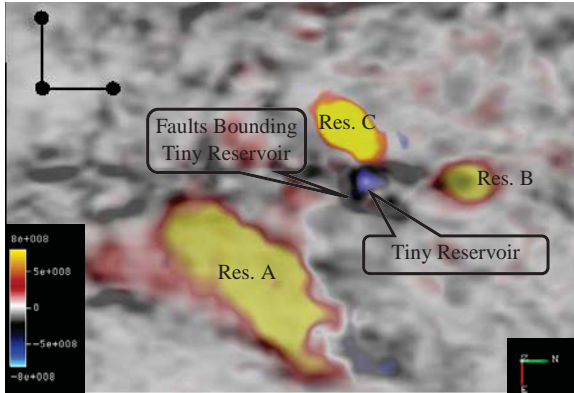


Figure 2. 29. Superimposed time slices exhibiting the location of the 'tiny' reservoir with respect to other neighboring reservoirs and regional faults. Note that the 'tiny' reservoir is surrounded by faults from all sides. The black lines on upper left corner scale the 500ft length along inline and crossline direction.

Two different paths through this new reservoir can be proposed for pressure communication between reservoir 'A' and reservoir 'C'. Random lines along the paths have been generated and are shown in figures 2.30 and 2.31. The only communication path I found from reservoir 'C' to 'tiny' reservoir is through reservoir 'B'. Both figures show a similar communication path between the 'C' and 'tiny' reservoirs. But pressure communication from reservoir 'A' to 'tiny' reservoir could be either through the water-encroachment zone (figure 2.31) or directly from reservoir 'A' (figure 2.30) where there is no apparent seal between it and the 'tiny' reservoir. The path through the water encroachment zone seems more reasonable as we see that the water sand in that direction responds to pressure drop. In any case, it can be suggested that the pressure drop in reservoir 'A' is first communicated to 'tiny' reservoir, and then goes to reservoir 'B' and finally is communicated to reservoir 'C'.

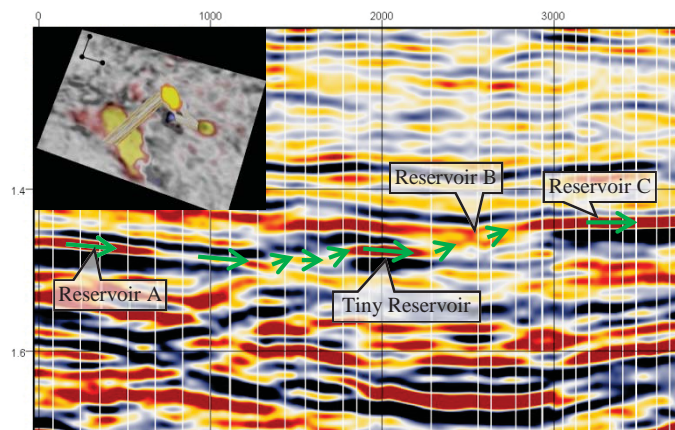


Figure 2. 30. A random line connecting all the reservoirs exhibiting time-lapse changes. The possible path for pressure communication is marked with green arrows. The figure in the left corner displays random line map location, as it turns around to connect the different reservoirs.

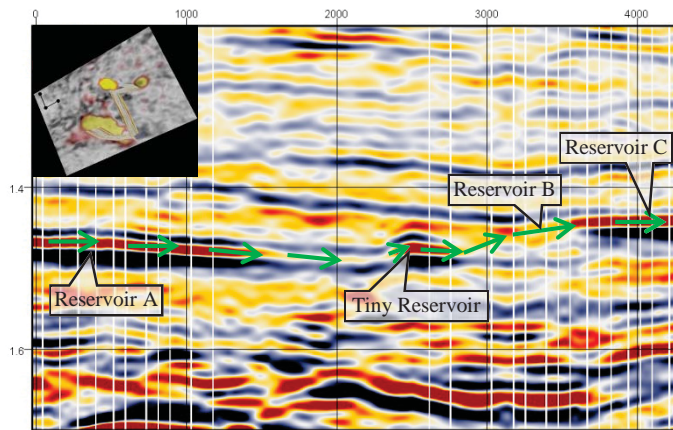


Figure 2.31. Another random line exhibiting a different path for pressure communication. The possible path for pressure communication is marked with green arrows. The figure in the left corner shows how the displayed random line turn around to connect different reservoirs. The only difference in this line is that it connects reservoir 'A' with the 'tiny' reservoir through water-sand rather directly connecting across faults.

In response to regional pressure drop, oil in the 'tiny' reservoir expands from legacy to Phase I. With further pressure drop from Phase I to Phase II water might have replaced the oil in the 'tiny' reservoir by pushing that oil towards reservoir 'A' or 'B', and that results in dimming of the 'tiny' reservoir -- but the mechanism of water-replacing-oil is unclear, and this explanation is not entirely satisfactory.

One may notice that reservoir 'B' on all these sections appears higher (shallower) than the 'tiny' reservoir, therefore one could argue with my observation that reservoir 'B' was originally water saturated while the 'tiny' reservoir was filled with oil. In this case, oil from the 'tiny' reservoir should have migrated to reservoir 'B' long before any production. The only explanation for my observation is that 'tiny' reservoir exhibits a local high on seismic data (Figure 2.31). It is possible that before discovery oil would have been trapped in that local high within the reservoir above the spill point, and pressure equilibrium would have been established between the reservoirs not letting oil escape. With the pressure drop after production started, oil expanded and gas came out of solution and the 'tiny' reservoir exhibited brightening. After a little more pressure drop, the oil from the reservoir might started to escape while water could have been entering into the reservoir due to local hydrodynamic conditions, causing dimming between Phase I and Phase II.

## 2.5. Time-Lapse, Travel-Time Shifts, and Reservoir Compaction

Production from a reservoir, especially unconsolidated over-pressured reservoir, induces time-lapse changes not only in seismic amplitude but also in the arrival times. Pressure changes can affect the stress and strain field not only in the reservoir but also in the overlying and underlying formations (Hawkins et al. 2007, Barkved and Kristiansen 2005). Seismic waves travelling through reservoirs as they are being depleted have

different travel times before and after productions because of the depletion induced changes in stress and strain fields. These changes in travel time-shifts are referred to as time-lapse time-shifts (Hatchell and Bourne 2005).

Time-lapse time-shifts within the reservoir and outside the reservoir are usually of opposing sign. Decrease in pore-pressure implies an increase in effective pressure that may result change in reservoir thickness. This process is often termed reservoir compaction. Compaction of reservoir not only changes the thickness of the reservoir but also increases seismic velocity of the formation. Decreased reservoir thickness and increased seismic velocity each decrease the travel time through the reservoir. Decrease of reservoir thickness is often coupled with the surface subsidence so the net effect of change in reservoir thickness may be negligible in the overlying rocks but in some cases the “arching” support of the overburden, and compaction of the reservoir may also result in stresses that “pull” the laterally surrounding rock and seismic velocities may decrease outside the reservoir, both above it and alongside it. The net result is that reflections may be delayed outside the reservoir after production. Maximum travel-time delays are expected close to the depleting reservoir, while travel-time advances may be expected for reflectors at or beneath the base of the reservoir.

Several approaches based on geo-mechanical modelling have been developed recently to estimate the compaction of reservoir and stress changes from travel-time shifts associated with a compacting reservoir (Landrø and Stammeijer 2004, Herwanger and Horne 2005). The topic is out of the scope of this work, which will be restricted to observations of travel-time shifts in the Teal South data sets.

In time-lapse analysis of the Teal South data, it was observed that reflections at the down-dip end of the reservoir ‘A’ were delayed in Phase II data relative to the Phase I data. This observation led me to analyze the Teal South data for indications of possible reservoir compaction in reservoir ‘A’. Any such analysis needs the travel-time shifts to be preserved in data processing, but we know that the legacy data were processed quite differently from the time-lapse data, and different velocity fields were likely used in in the two data types. These facts about data processing limit the accuracy of our observations.

### **2.5.1. Methodology**

Travel-time shifts are estimated first from legacy to Phase I data and then from Phase I to Phase II data. The legacy data were acquired using streamer cables towed close to the water surface behind a boat, and time-lapse data were acquired using ocean bottom cables resulting in different reference datum levels. Further, seasonal changes in water temperature and depth may also have induced travel-time differences. In order to compensate these travel-time changes, static shifts were applied to time-lapse data using a reflector as explained in section 2.3.1. After applying the static shift to align reflections,

travel-time shifts between the legacy and Phase I data were computed. To determine the travel time shifts, legacy and time-lapse data were matched by identifying, for example, a peak on one data set with the peak on other data set; time differences between the two were reported as time-shifts. The time-shifts were then interpolated for intervening sample points and then smoothed by applying a low-pass filter. With limited accuracy, it can be presumed that these travel-time shifts are the results of overburden and sideburden stretch caused by reservoir compaction.

The two time-lapse data sets do not need initial static correction as both data sets (Phase I and Phase II) were recorded with ocean bottom cables with the same locations and were processed identically to remove the differences. Phase I data and Phase II data are directly matched to determine the time-lapse travel-shifts between them

### 2.5.2. Results and Discussion

Figure 2.32 shows the time-shifts between the legacy and Phase I data, using inline 3500. Legacy data were set as reference. Green color indicates delay in arrival times from legacy to Phase I and blue indicates early arrival. The figure shows that there are negligible time-shifts everywhere other than at the areal location of reservoir 'A' with significant delays in arrival times in the overburden above it. Within the reservoir and below the reservoir the delay is less than above. Stretching of overburden because of reservoir depletion delays the reflections in the overburden. Compaction of reservoir A and (possible) decrease in reservoir thickness act to counter the delay caused by overburden stretching and we observe much less delay within the reservoir and below the reservoir. The effect of compaction seems to be more pronounced along the down dip direction of the reservoir.

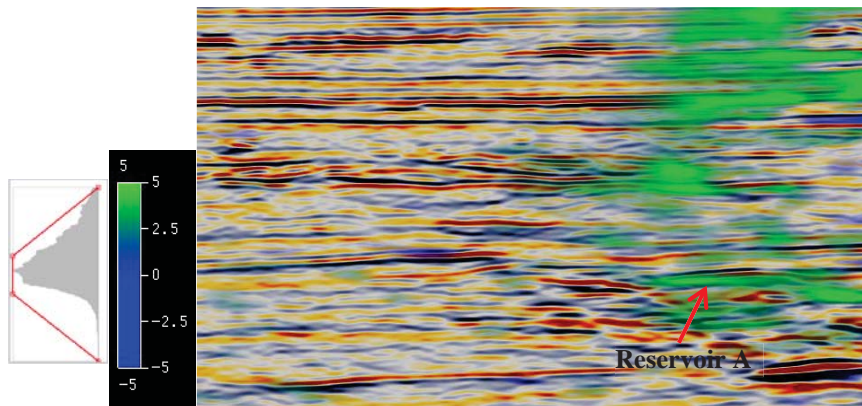


Figure 2. 32. Time-lapse travel time shifts between legacy and Phase I data, presented on inline 3500 in green and blue color. Legacy data were set as reference. Green color shows delay in arrival time and blue shows the opposite. In the background legacy data is displayed. There is a significant delay in Phase I reflection over reservoir. The travel-time shifts are believed to be because of the overburden stretch caused by compaction of reservoir A.

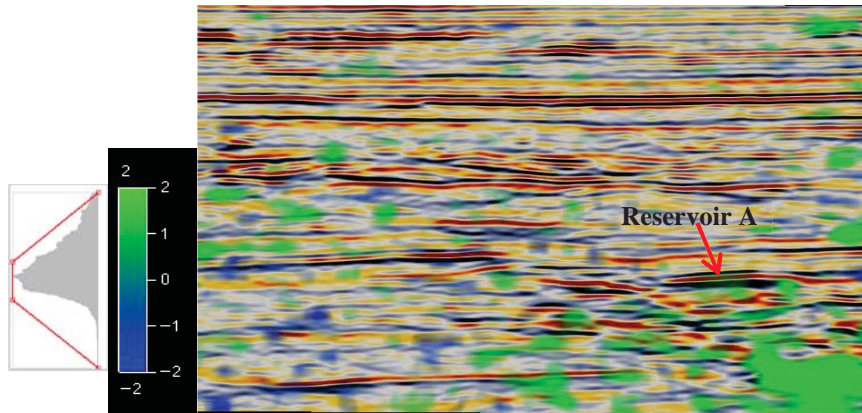


Figure 2.33. Time-lapse travel time shift between Phase I and Phase II data, presented on inline 3500 in green and blue color. Phase I data were set as reference. Green color shows delay in arrival time and blue shows the opposite. In the background legacy data are displayed. There is negligible time-shifts in overburden. There is small delay observed in the underburden. Delay in overburden could be because of stretch in underburden.

Figure 2.33 shows the time-shifts observed between Phase I and Phase II data sets. Between Phase I and Phase II, negligible time-shifts are observed in the overburden, but reflections from the reservoir top are delayed by almost 1 ms. This delay is most likely caused by the compaction of reservoir. However, reflections from interfaces beneath reservoir 'A' are delayed by almost 2 ms or more (see Figure 2.33 lower right corner). It could be a processing artifact as processing applied to time-lapse data concentrated less on reflections coming from beneath reservoir 'A'; however it could also be caused by stretching in the underburden. Hawkins et al. (2007) performed geo-mechanical modelling over three different fields from the North Sea (near each other, at depths of 5100-5600m) and inverted the time-lapse travel time shifts into respective 4D stress changes. They found almost 5 ms delay in the overburden of two reservoirs while the third reservoir exhibited only 2 ms time-shift, and that the third reservoir exhibited stronger travel-time shifts in the underburden than in the overburden. They suggested that compaction in that particular reservoir had been accommodated more by stretching of underburden than stretching of overburden. The observed travel time-shifts at Teal South between Phase I and Phase II data could be a result of similar process: stretching of underburden rather than overburden.

Both data sets suggest compaction of reservoir 'A' and stretch in the overburden and underlying rocks. Although the accuracy of time-shifts number is limited by the data quality and processing of time-lapse data, the results suggest that reservoir 'A' has undergone some amount of compaction as a result of pressure depletion. Processing of time-lapse data might have already been corrected for compaction effects, accounting for the very small effects of compaction in the time-lapse (Phase II – Phase I) data.

## 2.6. Conclusion

Time-lapse data from the Teal South oil field was analyzed to explore the effects of production on the producing reservoir and neighboring, unproduced, reservoirs. Three sets of seismic data were acquired over the field at three different times. The first set of data, the legacy data, was acquired using streamer cables prior to production, and the other two data sets (time-lapse data – Phase I and Phase II) were acquired using ocean bottom cables after 8 and 30 months of production. Time-lapse data had already been processed to preserve the production-induced changes and to suppress the background noise differences. The legacy data were cross-equalized in this study with the Phase I data to allow studies of the early period of production. The reservoirs are high-porosity, unconsolidated, and overpressured, containing light oil just above bubble point.

To define the time-lapse changes in amplitude and to emphasize the visual impact, the difference of squared instantaneous amplitude is computed between consecutive surveys, and two difference cubes were generated: one between legacy and Phase I and the other between Phase I and Phase II. The difference cubes support the results from previous studies by (Pennington et al. (2001), Ezawi, Pennington, and Islam 2012) and add the following observations.

A small time-delay (1ms) in Phase II data makes water influx appear as if it is encroaching from the downdip end, but along the upper boundary of the reservoir rather than at the base of the reservoir 'A'. A 1 ms time-shift to Phase II data moves the dimming observed to locate water encroachment at the base of the reservoir.

Neighboring reservoirs that are separated from the producing reservoir by one or more faults show time-lapse changes that implies pressure changes can be communicated easily across the fault(s).

Addition of legacy data to the time-lapse study leads to the suggestion that reservoir 'B', previously reported as a leaking reservoir, is only developed as an oil reservoir after production from reservoir 'A'. Legacy data show that the sand of reservoir 'B' was water-filled at the time of discovery. It is proposed that pressure drop from production in reservoir 'A' has been communicated to reservoir 'C', which was an oil reservoir at the time of discovery. Because of this pressure drop, gas in reservoir 'C' came out of solution and the reservoir pore volume expanded because gas occupies more space than oil. This pushed oil down within the reservoir 'C', past the spill point and towards reservoir 'B' where it is trapped again. With continued drop in pressure, more oil is added to reservoir 'B', where it also expands. After some period, oil from reservoir 'B' reaches its spill point, escaping into the surrounding rock.

Some confusing observations can be accounted for by complicated, but reasonable, scenarios. For example, the dimming and brightening of different portions of reservoir 'C' at different times can be explained by a tradeoff between frame stiffening (of the

rock) and the effects of fluid expansion, resulting in negligible time-lapse changes on stacked data in the oil zone, but in the gas cap the fluid effects dominate.

Using similarity attributes, the orientations of regional faults are analyzed and two possible paths for pressure communication between reservoir 'A' and reservoir 'C' are established. A 'tiny' reservoir is found between these two reservoirs, surrounded by faults, and showing time-lapse changes on all data sets. It is proposed that this 'tiny' reservoir is providing a path for pressure communication.

Possible compaction effects were studied through travel-time shifts. The results suggest significant compaction of reservoir 'A' between legacy and Phase I times. Due to reservoir compaction overburden is stretched that has caused travel-time delay of about 5ms in Phase I data relative to legacy data. Within the reservoir this effect is reduced because of decrease in reservoir thickness and increase in seismic velocity of reservoir, and the underburden then shows a negligible delay. Almost no time-shift is observed in the overburden from Phase I to Phase II, but a small delay is found in the under-burden that suggests stretching of underburden between Phase I and Phase II.

## **3. <sup>2</sup>Elastic property changes from reservoir compaction inferred from pre-stack seismic time-lapse data**

### **3.1. Abstract**

Hydrocarbon reservoirs are often monitored using repeated seismic observations in order to track fluid movement and other changes. Here, I present a study of compaction-induced anisotropy in an unconsolidated overpressured sand reservoir from Teal South field in the Gulf of Mexico. Most other studies have dealt with normally pressured reservoirs, and this study makes observations that appear to be unique, but may have wider significance. Previous work at Teal South had demonstrated that the time-lapse observations could not be satisfied through models of fluid changes without strong pressure effects acting on the formation rock framework. However, those studies were not highly quantitative, and some minor inconsistencies appeared on closer examination. In this study, I examine the effect of the pressure-sensitivity of seismic moduli in the formation, and carefully examine the offset-dependence of amplitudes in light of several rock-physics models, both empirical and theoretical. The reflections from the surrounding water sand are very small, and changes due to pressure sensitivity are difficult to observe, explaining the apparent lack of time-lapse pressure-sensitivity effect in those zones. The amplitude-versus-offset behavior in water, oil, and gas zones is best modeled under the assumption that this over-pressured reservoir becomes strongly anisotropic as it undergoes uniaxial compaction during production to near normal fluid pressures. While the results obtained here are only weakly constrained due to the limited offset ranges and low fold (the data had been acquired in the late 1990's), it strongly suggests that anisotropic effects in poorly consolidated overpressured reservoirs undergoing primary depletion may in fact dominate over fluid effects after bubble point has been reached.

### **3.2. Introduction**

The Teal South field is a shallow water (85 m) oil field in Eugene Island Block 354 in the Gulf of Mexico. The field produced both oil and gas from many small Tertiary reservoirs that are mainly composed of unconsolidated sands. In 1996, Texaco and Input / Output chose Teal South as a time-lapse test site to evaluate the effectiveness and efficiency of a novel 4-D / 4-C permanent reservoir monitoring system. Quick depletion and high sensitivity to production related pressure and fluid changes make the Teal South an excellent candidate for a time-lapse study. In late 1997, Texaco opened the project for industry and academia participation, through a consortium managed by the Energy Research Clearing House (Ebrom, Krail, et al. 1998). The consortium grew to include a number of companies and universities.

---

<sup>2</sup> The material contained in this chapter will be submitted for publication in Interpretation, a journal published by the Society of Exploration Geophysicists.

The Teal South project has provided three different sets of seismic data covering three different times. The first 3D seismic data set (“legacy” streamer data) was acquired in 1995, almost a year before the first production on November 1996. In July and August 1997, after almost 8 months of production, first set of 4-D/4-C data (Phase I) was acquired using ocean bottom cable (OBC). With the same survey geometry as of Phase I but with some additional coverage, “Phase II” data were acquired in April 1999, after 30 months of production. See Ebrom, Krail, et al. (1998) and Rodriguez-Suarez, Stewart, and Lu (2000) for data quality, survey design and acquisition results.

Teal South field has many small reservoirs. Among them, the main reservoir of interest to this and many previous studies is the so-called “4500-ft” reservoir, labelled as “Reservoir A” in figure 3.1. Many institutions have used Teal South data to test and develop processing and interpretation techniques for time-lapse seismic data (Druzhinin and MacBeth 2001, Shams and MacBeth 2002, Hall and MacBeth 2001, Pennington et al. 2001, Pennington et al. 2002, Ezawi, Pennington, and Islam 2012). In the Teal South project, data prior to commencement of production came from a surface-streamer 3D survey, while time-lapse observations were made using ocean-bottom cables (OBC) at two different times, both after the initial release of gas from solution; the dedicated time-lapse studies are called “Phase I” and “Phase II,” while the original data set is referred to here as the “legacy” volume.

Figure 3.1 shows the 3D structural view of the 4500-ft sand and reservoir “A”. Two NS trending normal faults provide a three-way closure on the sides of the reservoir while an oil-water contact (OWC) identifies the down-dip extent of the reservoir.

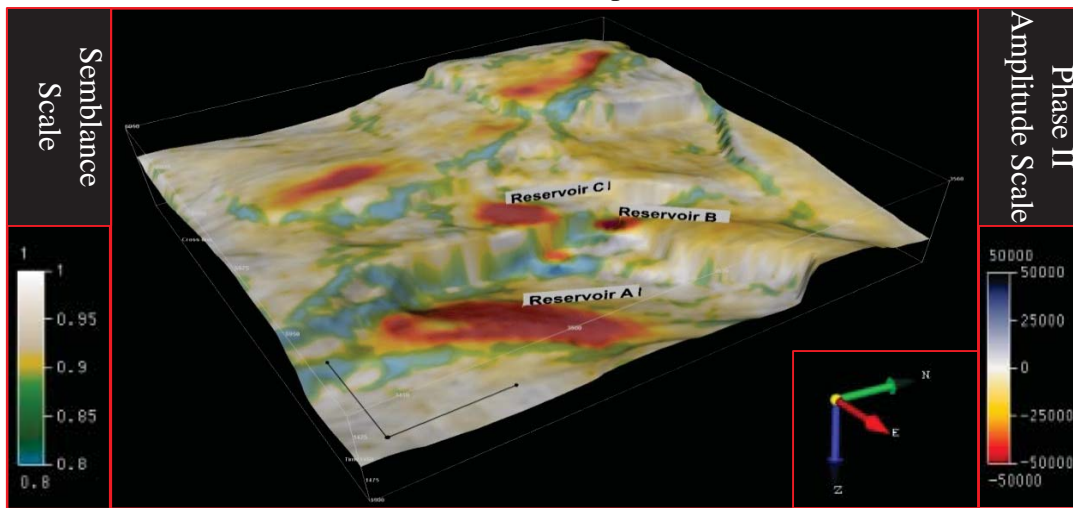


Figure 3. 1. 3D structural view of 4500-ft sand tracked on legacy data. Seismic amplitude from Phase II data is displayed on the horizon where red marks the trough and black marks the peaks, using the color scale on the right. Phase II data is underlain by ‘Semblance’ attribute computed from legacy data. Semblance is displayed using color scheme given on the left of the figure. The blue color represents the most likely locations of faults. The black lines on the horizon show 1000ft length in both directions.

A horizontal well (D-10) was drilled through the reservoir ‘A’ that produced both oil and gas. The reservoir was over-pressured at the time of the discovery (21.35 MPa; normal pressure would have been 14.33 MPa). There are only two measurements of reservoir pressure available – the initial reservoir pressure of 21.35 MPa and a measurement of 16.94 MPa made after 570 days of production. Christie, MacBeth, and Subbey (2002) performed history matching and generated a pressure profile over the life of the reservoir, the production data and proposed pressure profile for reservoir ‘A’ is displayed in Figure 3.2. The history match results suggest that there was a rapid drop in reservoir pressure at the start of the production, indicating liquid-expansion drive mechanism. The reservoir pressure being very close to the bubble point, gas started coming out of solution shortly after production started and a free-gas phase developed. During this solution-gas drive phase of production the pressure drop was gentler but steady (Pennington et al. 2001). Christie, MacBeth, and Subbey (2002) suggest that gas cap drive mechanism is supplemented with a moderate aquifer drive mechanism, consistent with other time-lapse observations reported in the original papers cited previously.

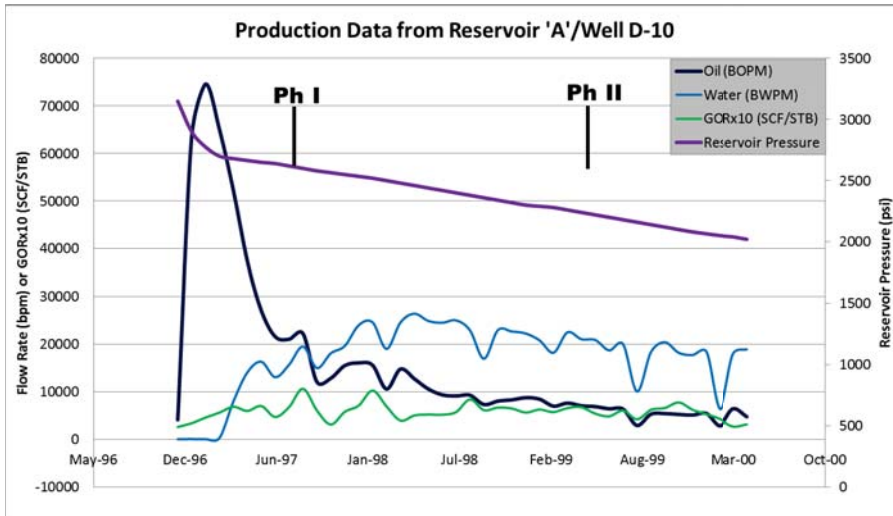


Figure 3. 2. Production history and pressure profile of the 4500-ft sand, reservoir 'A'. Oil and water flow rates are given in barrels per month, and GOR is given in SCF/STB. GOR is multiplied by 10, and will be read on scale on left. Pressure data are proposed by Christie et al., 2002. The image is reproduced after Pennington et al. (2001) with permission. See Appendix E for permission.

The 4500-ft sand exhibits typical class III Amplitude-Versus-Offset (AVO) reflection behavior as a typical ‘bright-spot’ in the shallow Gulf of Mexico. The reservoir is composed of overpressured, unconsolidated, highly porous (~39%) Tertiary sand that is highly sensitive to pressure and fluid changes. One can immediately conclude that 4500-sand will show initial and continued ‘brightening’ at zero offset as gas saturation increases with production; the initial brightening is due to the decrease in both incompressibility and density as gas comes out of solution, but the continuing expected brightening is due primarily to the density effect on the reflection coefficient rather than

the incompressibility change, which is nominal after the first several percent of pore volume is occupied by gas. Pennington et al. (2001) conducted rock-physics modelling and AVO analysis and showed that the zero-offset and AVO behavior that was observed long after gas came out of solution could not be reconciled with any model that only considered fluid changes; instead, rock frame stiffening was assumed to occur, and qualitatively accounted for the observations. They concluded that the producing reservoir will show an initial brightening at all offsets because of the free-gas evolution, but that this ‘brightening’ will be followed by a slight “dimming” at near offsets along with continued brightening at far-offsets due to a decrease in Poisson’s ratio caused by frame-stiffening as the pore pressure decreases (Figure 3.3). In the same work, they pointed out that neighboring reservoirs exhibited similar time-lapse changes, suggesting a pressure communication between the reservoirs across the faults; the present study emphasizes only the producing reservoir, but may be applicable to the unproduced nearby reservoirs that are experiencing regional pore-pressure “blowdown”.

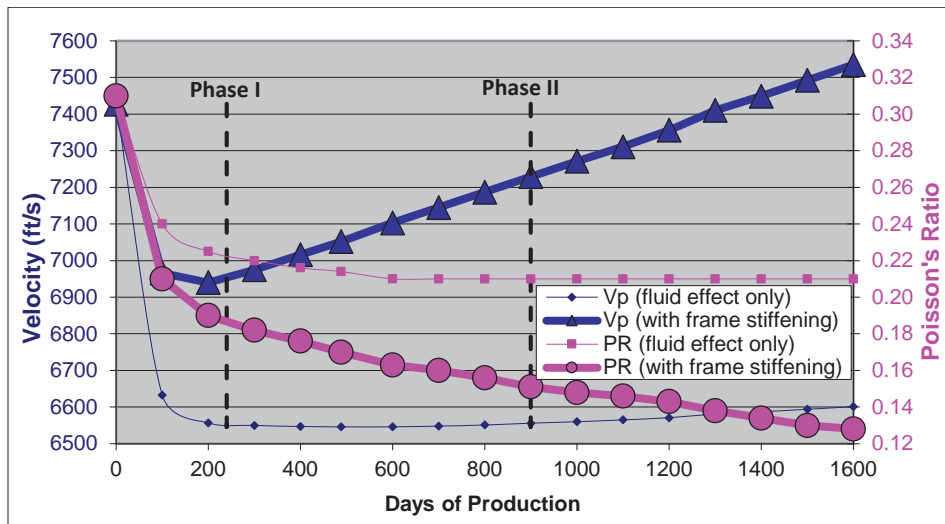


Figure 3. 3. Effect of frame stiffening on P-wave velocity and Poisson's ratio of reservoir 'A'. Fame-stiffening increases P-wave velocity and decreases the Poisson’s ratio much rapidly than fluid effect. The figure is adapted from Pennington et al. (2001) with permission. See appendix E for permission.

The original work emphasized horizon-based attributes and observations. Because of this, some observations later made in the volume-based studies of Ezawi, Pennington, and Islam (2012) had not been noticed in the original studies. The latter paper used squared instantaneous amplitude as the main attribute to study, increasing the ability to recognize large changes without being obscured by smaller, noisier changes in the data, but was based on stacked data only, and did not attempt to quantitatively interpret the results. It is important to recognize that none of these studies had identified any time-lapse changes in the water sand, although its pressure sensitivity should be as strong as it is in the oil sand. This dilemma led to the study reported here.

The objective of this work was twofold: to establish the reason for the apparent lack of response in the water sand, and to quantitatively analyze the effects of AVO on the stacked data covering the reservoirs. The fluid-substitution technique is well understood, but the stress-sensitivity of the rock frame is not well defined, particularly for unconsolidated overpressured formations. Some models are purely empirical, and I used the empirical model employed in the original study by Pennington et al (2001). A number of theoretical rock-physics models have been proposed that predict the effective elastic properties of unconsolidated sands based on the Hertz contact mechanics model (Mindlin 1949, Digby 1981, Norris and Johnson 1997, Walton 1987, Goddard 1990, Mavko, Mukerji, and Dvorkin 2009), and I used the Hertz-Mindlin model (Mindlin 1949) for soft sand and Walton's model (Walton 1987) for unconsolidated anisotropic sands to predict the elastic properties of 4500-ft sand under different stress conditions. The elastic properties of fluid saturated rock were then estimated for the oil-zone, the gas-cap zone, and the water-encroachment zone within the reservoir and for the nearby and underlying water sand, using Gassmann's model for fluid substitution (Gassmann 1951). Finally the AVO response was estimated at different stages of production and compared with the partial stacks from Phase I and Phase II. The stacked response from the predicted AVO response was then compared to the stacked response observed in the data using the squared instantaneous amplitude. Because pre-stack data from the legacy survey was not available to us, this study restricts its observations to Phase I and Phase II time-lapse OBC surveys, both of which were obtained after gas had come out of solution in the producing reservoir.

The modelling results clearly demonstrate the frame-stiffening from Phase I to Phase II. Fluid expansion causes a slight brightening at all offsets (gas had already come out of solution by the time of Phase I, limiting the observable gas effect), but the frame-stiffening effect causes a dimming at near offsets while brightening at far-offsets (Pennington et al. (2001), and when they both work together we may observe a dimming or no change at near offset but brightening at far-offset. Qualitatively, this matches the observations at Teal South, but a closer examination of offsets (or angles) casts doubt on the details of the model used by Pennington et al, 2001. Different rock-physics models used in the present work each predict different absolute rock-physics properties but they all predict similar changes in AVO response from Phase I to Phase II as well as either no change or a slight dimming of stacked amplitude. In this work, I present results only from the Hertz-Mindlin model to represent isotropic models. These models, assuming isotropic conditions, do not predict the observed strong change in amplitudes within the first 30°, particularly in the AVO gradient, between Phase I and Phase II.

The “gradient” or slope of the AVO curves is mainly controlled by the Poisson's ratio (or by the ratio between compressional and shear velocities,  $V_p/V_s$ ). The AVO curves steepen as  $V_p/V_s$  ratio decreases. To match the AVO response observed, it was essential to come up with a scenario that predicts the observed decrease in  $V_p/V_s$  ratio. The

decrease in  $V_p/V_s$  ratio is possible either by decreasing bulk modulus ( $K$ ) or by increasing shear modulus ( $\mu$ ) from Phase I to Phase II, as suggested by equation 3.1.

$$\frac{V_p}{V_s} = \sqrt{\frac{K}{\mu} + 4/3} \quad (3.1)$$

A decrease in bulk modulus does not seem plausible: increased net pressure (overburden pressure minus pore-fluid pressure) stiffens the rock frame, and the dry-frame bulk modulus is expected to increase between Phase I and Phase II (the bulk-modulus drop due to release of solution gas mostly took place prior to Phase I).

An increase in shear modulus, due to frame-stiffening and an increase in friction at grain contacts, seems a reasonable option for the decrease in  $V_p/V_s$  ratio required by the change in AVO behavior. Contact laws such as Hertz-Mindlin suggests that an increase in friction at grain contacts increases the shear modulus without any significant change in bulk modulus. Considering the fact that reservoir was highly over-pressured at the time of the reservoir discovery and still somewhat over-pressured during Phase I data acquisition, a scenario can be assumed that 4500' sand undergoes an increase in the friction factor with an increase in effective stress. But an increase in shear modulus from Phase I to Phase II would also result in near-offset reflections to decrease so much that the stacked output is expected to show 'dimming' rather than 'brightening', and this contradicts observations from the seismic data.

There are many examples of lab measurements and field observations that suggest a different (higher as well as lower) pressure dependence of effective elastic moduli than the 1/3 power proposed by the contact law (Duffaut and Landrø 2007, Bandyopadhyay 2009, Goddard 1990); that is, the stress-sensitivity in isotropic contact models may vary considerably. Effects of changes in this stress-sensitivity on AVO response were analyzed, but also fail to explain the AVO behavior of the time-lapse data.

Because strain in a compacting reservoir is likely constrained to be uniaxial – the reservoir changes thickness, but does not shrink horizontally – we may conclude that the stress changes during production are anisotropic. Stress-induced fractures are often considered to be responsible for this anisotropy (Xu 2002); unconsolidated sands, however, may become elastically anisotropic under non-hydrostatic stress conditions (Bandyopadhyay 2009). Stacked time-lapse data from the Teal South show compaction (strain in the vertical direction) of reservoir 'A' without any recognizable deformation (strain) in the horizontal directions; this condition is referred to as uniaxial compaction. I examine the possibility that uniaxial compaction produced seismic anisotropy in the 4500-ft sand; due to availability of pre-stack seismic data only for the time-lapse surveys of Phase I and Phase II, I make the simplistic assumption that the reservoir was elastically isotropic at the time of Phase I (when it was still somewhat overpressured) but was

anisotropic by Phase II. I used Walton's model for unconsolidated anisotropic sands (Walton 1987) to estimate Thomsen's anisotropy parameters ((Thomsen 1986) for the 4500' sand. Thomsen's parameters are estimated for both uniaxial compaction (assuming no strain in horizontal direction, but allowing strain in vertical direction) and triaxial compression (nominally biaxial compression, designed to restrict deformation to uniaxial compaction with both horizontal stresses being equal and appropriate to maintain no deformation in those directions). These anisotropy parameters were then used to predict the AVO response for Phase II while assuming an isotropic medium for Phase I. The results predicted AVO response changes from Phase I to Phase II that are equal to the changes observed in the seismic data. The addition of anisotropy to the Phase II predictions also helped me predict the time-lapse changes observed from the stacked time-lapse data.

Based on my rock-physics modeling results, I conclude that brightening of reservoir 'A' from legacy to Phase I is caused by the fluid expansion and release of solution gas as pressure dropped below the bubble point. The brightening of the reservoir observed on stacked data and the increase in AVO gradient from Phase I data to Phase II data is mainly due to weak anisotropy developed from production-induced compaction of the 4500-ft sand. I could find no other physical scenario that explains the obvious brightening at appropriately far offsets between Phase I and Phase II. This work demonstrates the importance of anisotropy, often ignored in seismic data interpretation and AVO analysis. Compaction-induced anisotropy can produce strong time-lapse effects, which may mislead the interpreter if ignored.

### **3.3. Teal South AVO**

To study the AVO behavior of the 4500' sand we used the partial stacks prepared by Pennington et al. (2001). They preferred to use partial stacks rather than full CDP gathers because of the unequal distribution of traces on CDP gathers in the OBC data sets. Figure 3.4 shows partial stacks of reservoir 'A' from the Phase I (blue) and Phase II (pink). I established an "average" AVO property for the reservoir under each of the Phases by averaging the AVO trends of the partial stack gathers within the yellow box shown in Figure 3.4.

Figure 3.5 shows the AVO response obtained from the mean partial stacks of reservoir 'A' plotted as a function of  $\sin^2\theta$  (Figure 3.5a) and as angle of incidence (Figure 3.5b), using a simple, but sufficiently accurate, velocity model. The plot clearly demonstrates that the partial stack amplitudes at near offset traces do not change from Phase I to Phase II, but with increasing offset the amplitude brightens from Phase I to Phase II. Because of continuous production over this time, the pore-pressure decreases, causing fluid expansion primarily through an increase in gas saturation. If this process were acting alone, we should observe a very modest increase in amplitudes at all offsets. But the decrease in pore-pressure is accompanied by an increase in net confining stress that is

expected to stiffen the rock dry-frame. The combined result requires a decrease in Poisson's ratio from Phase I to Phase II in order to match the data.

The AVO curve for Phase II shows a steeper gradient than Phase I. As the slope of the AVO curve is mainly controlled by the Poisson's ratio, we require a decrease in Poisson's ratio (or, equivalently, in  $V_p/V_s$ ). The frame stiffening effect must nullify the effect of fluid expansion at near offsets such that we do not see any significant change in near-offset partial stack from Phase I to Phase II. But we do observe brightening at far offsets, requiring the decrease in Poisson's ratio. I applied a linear fit to the AVO curves and took a ratio of the respective slopes on the  $\sin^2\theta$  plot; the ratio of AVO gradient from Phase I to Phase II is estimated to be in the range 0.60. Now we have two constraints over the AVO change from Phase I to Phase II: there is no change in AVO at near offset, and the ratio of AVO slope from Phase I data to Phase II data is 0.60.

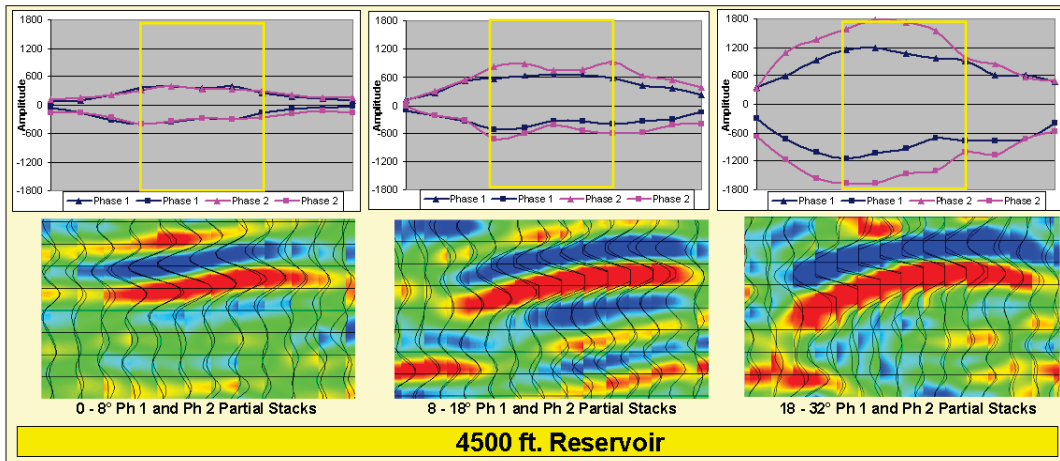


Figure 3. 4. Partial stacks extracted from the unmigrated P-wave seismic data for the 4500' sand reservoir 'A'. The blue lines represent the partial-offset stack from Phase I while the pink lines represent the partial-offset stack from Phase II data. The partial stacks enclosed in the boxes were used to compute the mean partial stack amplitude displayed in Figure 3.5. The image is reproduced after Pennington et al. (2001) with permission. See Appendix E for permission.

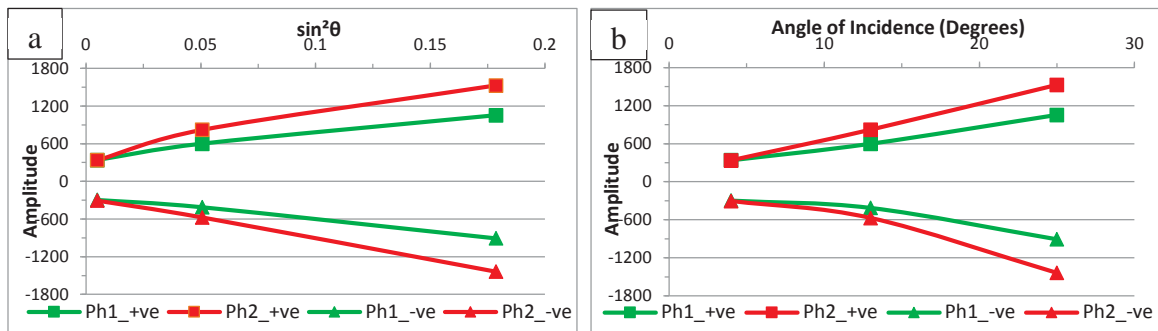


Figure 3. 5. AVO trend of 4500-ft sand reservoir 'A' as observed from the Phase I (green) and Phase II (red) unmigrated partial stacks. (a) Plot of mean partial-stack amplitude versus  $\sin^2(\theta)$ . (b) Plot of mean partial stack amplitude against angle of incidence. Note that there is a significant change in slope of the AVO curves from Phase I to Phase II.

### **3.4. Rock-physics Modelling and AVO Response**

In this section, I will use different rock-physics models in an attempt to predict AVO behavior for Phase I and Phase II data. For all these models, I am assuming constant properties for the overlying shale and reservoir sand. Fluid properties under different pressure conditions were estimated by Pennington et al. (2001) using Batzle and Wang relations (Batzle and Wang 1992). The fluid properties, shale properties, matrix properties and pressure data used in the modelling are same as those previously used by Pennington et al. (2001) and are summarized in Appendix A.

#### **3.4.1. Methodology**

Pennington et al. (2001) used Green's rock-physics model (Green 2001, Pennington, Green, and Haataja 2001) to predict the changes in dry frame elastic properties under different stress conditions for the oil zone in the producing reservoir. Using Green's model, they point out that during production from an oil-saturated rock fluid expansion and frame-stiffening work together, complicating the AVO prediction. That paper does not discuss the AVO response for any gas-cap that may exist, the water-encroachment zone, or for the neighboring or down-dip water-sand, which undergoes similar changes in net pressure. AVO response of water sand, in particular, is of interest because the water sand is presumed to experience the frame-stiffening effect but does not have gas coming out of solution.

As a first step of my work, I decided to evaluate how accurately Green's model estimates the time-lapse changes in elastic properties for gas cap, water-encroachment zone and water sand zones under different net pressure conditions.

Considering the limitations of Green's model, Hertz-Mindlin model for soft sand was later used to define the AVO trend of all zones of 4500-ft sand. In contrast to Green's model, Hertz-Mindlin model is a theoretical model that is based on Hertz's contact law.

Both models named above assume an isotropic medium and give the dry-frame elastic properties. Elastic properties for saturated rocks were then computed using Gassmann's fluid substitution. The modeled elastic properties were then used in the full Zoeppritz equation to compute the AVO response for all zones of 4500-ft sand (Zoeppritz 1919). These models, assuming isotropic medium, do not explain the AVO gradient change from Phase I to Phase II. Different possible scenarios including assumed changes in friction and pressure dependence were also analyzed to simulate the time-lapse AVO trend but no scenario under isotropic conditions explain the time-lapse AVO behavior of reservoir 'A'.

Finally, possible change in anisotropy of the 4500-sand due to production induced compaction is computed using Walton's model for unconsolidated anisotropic sands (Walton 1987). The anisotropic parameters determined by Walton's model were

incorporated with the elastic properties determined by Hertz-Mindlin model in Rüger's AVO model for anisotropic medium (Rüger 1997).

The AVO trends predicted from all above models were compared with the time-lapse AVO data using AVO gradient. In order to compare with the stacked seismic sections, The AVO results were used to prepare a synthetic CMP gather by convolving it with a 40Hz Ricker wavelet. Modelled NMO corrected CMP gathers were then stacked over  $0^{\circ}$  to  $30^{\circ}$  incident-angles representing the angle range of the original surveys. For direct comparison with the results by (Ezawi, Pennington, and Islam 2012), squared instantaneous amplitude was computed from this stacked wavelet using the Hilbert's transform. The results from all the three models are presented and discussed in section 3.5.

The sections below discuss the theory, limitations and procedure adopted in each rock-physics models used.

#### 3.4.1.1. Green's Model

The Green Model is an empirical model that uses an exponential relation between the dry-frame elastic properties and the effective stress, based on a previous model given by Eberhart-Phillips, Han, and Zoback (1989).

Rather than computing the dry-frame properties directly from Green's model, I estimated the dry-frame properties from saturated rock properties and fluid properties given by Pennington et al. (2001) using Gassmann's substitution assuming uniform saturation. The dry-frame properties were then used to estimate the saturated rock properties for gas cap, oil-zone, water-encroachment zone and water sand. The results from Green's model are presented and discussed in section 3.5.

However, Green's model has limited applicability in certain cases. The rock samples used in Green's model were competent, normally pressured and moderately porous. In contrast to this, 4500-ft sand is unconsolidated, overpressured and highly porous so Green's model does not accurately predict the effective elastic properties of 4500-ft sand.

#### 3.4.1.2. Hertz-Mindlin Model

Hertz-Mindlin model is a theoretical model based on Hertz contact law. 4500-ft sand is highly unconsolidated sand with very high porosity. A number of models have been presented to predict the effective elastic properties of unconsolidated sands (Mindlin 1949, Digby 1981, Walton 1987). These models assume unconsolidated sand as a random pack of identical spheres, and use Hertz contact law to relate effective elastic properties of the medium with the applied stress conditions.

According to the Hertz model of normal compression (Hertz, 1882), the contact area between grains increases with an increase in the normal stress. This change in contact area translates into an increase in effective elastic properties of the rock through the

contact stiffness. This model suggests a power-law relation between the effective bulk and shear moduli and the net confining pressure  $P$ , and proposes a power dependence of effective module as  $P^{1/3}$ . The model defines the effective elastic properties of a pack of spheres at some initial (depositional) porosity assuming some average number of grain contacts. The Hashin-Shtrikman (Hashin and Shtrikman 1963) lower bound is often used to estimate the effective bulk and shear moduli ( $K_{\text{eff}}$  and  $G_{\text{eff}}$ ) at porosities ( $\phi$ ) other than the initial un-compacted porosities. The equations are given in Appendix B.

To predict the elastic properties from Hertz-Mindlin model, we need to have the co-ordination number that is defined as the average number of contacts per grain. The co-ordination number depends on the grain arrangement in a packing, and ranges from 6 for a cubic packing to 12 for a hexagonal packing (Mavko, Mukerji, and Dvorkin 1998). Hertz-Mindlin model assumes a random packing of grains. Many other studies have tried to establish the relation between the porosity of a random pack of grains and the co-ordination number (Smith et al, 1929; Wadsworth 1960; Bernal and Mason 1960). Figure 3.6 shows the plot of co-ordination numbers with porosity as it has been reported in literature. The data for the plot were taken from Mavko, Mukerji, and Dvorkin (2009). The well logs from 4500-ft reservoir read a porosity of about 39% that corresponds to a coordination number of 8 in Figure 3.6. In our modelling, we used a co-ordination number of 8.

Comparison of field and lab measurements of compressional and shear velocities with the ones predicted by using Hertz-Mindlin model suggests that Hertz-Mindlin model over-predicts the shear modulus and so shear velocities. The main reason behind this over-prediction is that Hertz-Mindlin assumes no slip at grain contacts (Zimmer 2004, Duffaut and Landrø 2007, Bachrach and Avseth 2008). Mindlin (1949) demonstrates that if the spheres are first pressed together and then a tangential force is applied, the slip may occur. The amount of allowed slip depends on the friction between the contacting surfaces. Mavko, Mukerji, and Dvorkin (1998) introduced an ad hoc coefficient 'f' to account for friction, and define a new equation for shear modulus that is given in Appendix B (Equation B.5).

The coefficient 'f' defines the amount of average friction at contacts. For perfect adhesion,  $f=1$ , and in this case Poisson's ratio does not exceed 0.10. In contrast to this, absence of friction may occur in unconsolidated sands because of the presence of lubricants at some contacts (Mavko, Mukerji, and Dvorkin 1998). In this case  $f=0$ .

Friction between two grains does not affect the bulk modulus so it stays constant for all values of friction ( $0 \leq f \leq 1$ ). What value of friction should be used? Bachrach and Avseth (2008) present an example of shallow gas reservoir and demonstrate that in a granular medium a fraction of grains have frictionless contacts, and the remaining grains have infinite friction. They used binary mixing model to estimate the effective shear modulus

of the pack of grains, and concluded that the best fit to their data is achieved by using fraction of rough spheres equal to 0.07 and 0.35 respectively. Dutta et al., (2008) suggest that fraction of rough grains is 0.60.

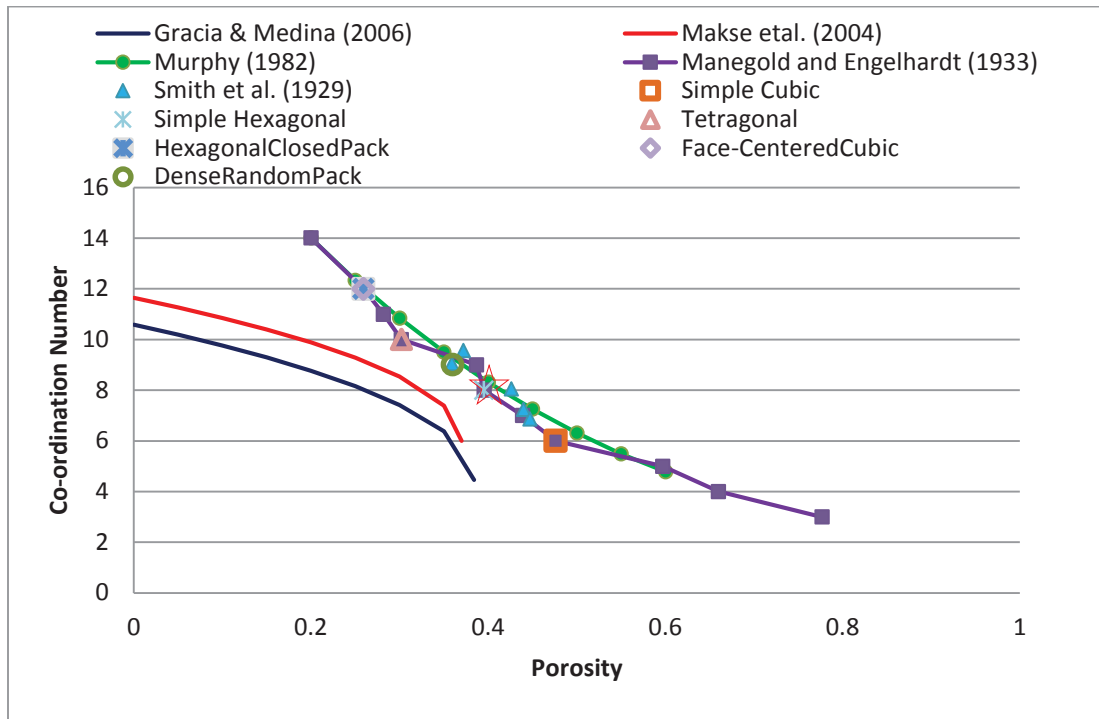


Figure 3. 6. A plot of co-ordination number with the porosity of the respective rock samples as reported in literature. The data used in this plot are taken from Mavko, Mukerji, and Dvorkin (2009). Red star marks the porosity of 4500-ft sand. The data reported in literature suggest a co-ordination number of 8 for 4500-ft sand.

Duffaut and Landrø (2007) and Zimmer (2004) report a misfit between the power-dependence of elastic moduli observed in the empirical measurements and predicted by the model. The Hertz-Mindlin model suggests a power-dependence of  $P^{1/3}$  for elastic moduli and  $P^{1/6}$  for seismic velocities. Duffaut and Landrø (2007) report that they get best fit to their data by using  $1/10$  as an exponent to pressure instead of  $1/6$  as included in the standard Hertz-Mindlin model. In contrast to this, Zimmer (2004) suggests that pressure dependence from the lab measurements is  $P^{1/4}$ . Goddard (1990) postulates that the discrepancy could be because of two possible reasons: 1- the co-ordination number changes with pressurization or 2- the grains are not perfect spheres. Zimmer, however, attributes this discrepancy to the grains rotation and slippage. He further concludes that shear modulus shows more pressure dependence than the bulk modulus.

I used the Hertz-Mindlin model to predict the dry-frame elastic properties. The initial porosity for the model is assumed to be 40%, and a co-ordination number of 8 is used. The data from well-logs suggest formation porosity of 39%. To estimate the effective elastic properties for 39% porosity, the Hashin-Shtrikman's lower bound is used. This

model is often referred as Hertz-Mindlin's soft sand model. The soft sand has been successful in predicting the elastic properties of unconsolidated sands from the North Sea and the Gulf of Mexico (Mavko, Mukerji, and Dvorkin 1998, Zimmer 2004). Dry-frame properties were estimated with different friction factors and pressure exponents and analyzed to study the effects of changes in friction and pressure dependences on AVO response. The results from Hertz-Mindlin models are presented under section 3.5.

#### 3.4.1.3. Walton's Model for Anisotropic Unconsolidated Sands

In all my work so far I have been using a basic assumption of isotropic medium for simplicity. This assumption is a routine practice among rock-physics community. However, most hydrocarbon reservoirs are anisotropic to some extent (Thomsen 1986, Stovas and Landrø 2005). Further, a layered medium composed of thin beds of different rocks (isotropic or not) will exhibit anisotropy if probed with a wavelength much longer than the individual bed thickness (Backus 1962). Despite the fact that most of the rocks on earth are anisotropic, most of the applications of elastic theory assume isotropic medium. Thomsen (1986) proposes two possible reasons for this inconsistency between the practice and reality. He suggests that most of the medium exhibit transverse anisotropy that masquerades as isotropy for most of the surface seismic data, and the expressions for anisotropy are very complicated even for this simplest case of anisotropic medium. Unconsolidated sands should become anisotropic under non-hydrostatic stress conditions. Under non-hydrostatic stress conditions, the grains' contacts that lie normal to the maximum stress direction develop a larger contact area, and the contacts that lie normal to the minimum stress axis have smaller contact area. Different contact areas in different directions make the elastic properties of the rocks anisotropic (Bandyopadhyay 2009) and the rock show different velocities in different directions.

Empirical and analytical studies show that presence of anisotropy can significantly affect AVO and conventional AVO analysis assuming isotropic medium may lead to flawed interpretations (Rüger 1997, Stovas and Landrø 2005, Wright 1987, Banik 1987). Stovas and Landro (2005) studied the effect of anisotropy on AVO. They conclude that changes in anisotropy within the reservoir rock (because of pressure change) can cause a 10-20% difference in reflection coefficient. This difference is large enough to be observed on the seismic data.

Time-lapse data from the Teal South show compaction of reservoir 'A' between Phase I and Phase II, however, no lateral deformation is observed. The vertical deformation might have induced weak polar anisotropy in the 4500-ft sand especially around the reservoir where compaction is severe.

Thomsen (1986) demonstrated that a transversely isotropic medium can be defined by only five independent constants that define the three anisotropy parameters, often called

Thomsen's anisotropy parameters. These parameters are P-wave anisotropy parameter ( $\epsilon$ ), S-wave anisotropy parameter ( $\gamma$ ) and angular anisotropy parameter ( $\delta$ ).

' $\epsilon$ ' describes the fractional difference between the p-wave velocities along and normal to the symmetry axis. ' $\gamma$ ' describes the fractional difference between SH- velocities along and normal to the axis of symmetry (Mavko, Mukerji, and Dvorkin 2009). ' $\delta$ ' describes the angular dependence of p-wave velocity. It defines the second derivative of p-wave phase velocity function at vertical incidence (Tsvankin, Helbig, and Treitel 2001, Bandyopadhyay 2009). Thomsen also demonstrated that ' $\delta$ ' is the most important anisotropy parameter as it affects the reflections at small incidence angles where most of the reflection profiling takes place.

The one most recognized model to compute anisotropic parameters for unconsolidated sands is by Walton (1987). He, using contact law, derived the relations to compute elastic stiffness of an anisotropic medium under an arbitrary applied strain. The elastic stiffness then can be used to compute the anisotropy parameters.

Walton also provided expressions for effective moduli. These expressions are similar to Hertz-Mindlin model, and he defines the moduli for two distinct scenarios; no-slip ( $f=1.0$  for Hertz-Mindlin) and no-friction ( $f=0.0$  for Hertz-Mindlin). Walton assumes that normal and shear deformation of two grains in contact occur simultaneously while the Hertz-Mindlin model assumes that normal deformation occurs first and then a tangential deformation may occur at grain contacts (Mavko, Mukerji, and Dvorkin (2009)).

Walton's model for anisotropic sands is applicable to situations where uniaxial strain has caused the anisotropy. Bandyopadhyay (2009) corrected his relation for shear moduli, and then extended this model for triaxial strain conditions.. The equations for later case assume that the strain along vertical axis is larger than the horizontal axis and there is equal strain along both horizontal directions. The equations are valid for weak transverse isotropy, also called polar anisotropy. In order to define anisotropy in the 4500-ft sand, I computed the Thomsen anisotropy parameters using equations derived by Bandyopadhyay (2009) from Walton's model. The relations are given in Appendix C

Thomsen (1993) gave the relations for AVO of a medium with weak anisotropy. Rüger (1997) modified his relation and derived a new approximation that is given in Appendix C. Approximations by Thomsen (1993) and Rüger (1997) have the same AVO gradient but Rüger's relation is believed to be more accurate at large angles.

Teal South time-lapse data clearly show the evidences for vertical compaction without any signs of lateral deformations. In other words, time-lapse data indicate the presence of vertical strain ( $E_{33} \neq 0$ ) in the Teal south but no horizontal strain ( $E_{22} = E_{11} \approx 0$ ). This inequality of strain between the vertical and lateral axis could have caused weak polar anisotropy.

In order to define anisotropy in the 4500-ft sand caused by compaction, I computed the Thomsen anisotropy parameters, first assuming uniaxial compaction (no lateral strain) and then triaxial compression (both vertical and horizontal strain).

Effective moduli from the Hertz-Mindlin model and Walton's model are very close to each other for isotropic conditions. Assuming that the elastic properties and velocities predicted by the Hertz-Mindlin model are equivalent to the vertical velocity of the reservoir A, I used these velocities and the previously computed Thomsen anisotropy parameters in Rüger's equation to predict the AVO response for all zones of the 4500-ft sand. The AVO response was predicted for Phase II and final (strong depletion –after 1600 days of production) conditions only, assuming that the reservoir was isotropic at the time of Phase I acquisition, presented in the following section.

### **3.5. Results and Discussion**

Most of the rock physics models used in this work generated similar trends of time-lapse variations in elastic properties, though with different absolute numbers. All models conclude frame-stiffening in response to reservoir pressure drop is important, but different models exhibit different pressure dependencies. The results from the isotropic cases of Green's model and Hertz-Mindlin model are discussed together, and compared with each other to evaluate the similarity and differences of the two methods. The discussion will be followed by an analysis for effect of friction factor and pressure dependence on AVO. Finally, results from Walton's anisotropic model will be discussed to conclude that anisotropic conditions better explain the time-lapse AVO response and stacked response from Teal South that could not be explained under isotropic conditions.

#### **3.5.1. Green's Model and Hertz-Mindlin Model**

Figure 3.7 and Figure 3.8 show the change in modeled p-wave velocity and Poisson's ratio as water encroaches into the reservoir and/or gas comes out of the solution during the production life of the 4500-ft reservoir, using Green's model and Hertz-Mindlin model respectively.

Both models show a similar general trend in response to reservoir pressure drop. The Hertz-Mindlin model for soft sand predicts lower velocities as compared to the Green's model. Hertz-Mindlin model predicts compressional velocity of 7640 ft/s for water sand at initial reservoir pressure. This velocity is a little higher than 7460 ft/s, read from well logs from nearby wells. Green's model predicts even higher velocities, it is due to the fact that Green's model is an empirical relation based on competent rocks that exhibit higher velocities.

One important point to notice is that the Hertz-Mindlin predicts a Poisson's ratio too low to be acceptable. The assumption of no slip at grains' contacts or infinite friction ( $f=1$ ) in the Hertz-Mindlin model results in an effective shear modulus that is too high and a

Poisson's ratio that is too low. This may also account for over-prediction of p-wave velocity in water sand by Hertz-Mindlin model compared to the logged p-wave velocity.

Both isotropic models conclude that all zones of the reservoir show similar general trends of p-wave velocity and Poisson's ratio, with differences only in detail. Because the reservoir was very close to the bubble point at the time of discovery, gas started coming out of solution immediately after the start of production, causing a sudden drop in fluid modulus and resulting rapid decrease in p-wave velocity. As production continued, the pore-pressure decreased and net pressure (the difference between overburden and pore-fluid pressure) acting on the rock frame increased that caused the rock frame to stiffen. After Phase I the frame stiffening dominates the fluid expansion effect and p-wave velocity show a gradual increase.

Like the p-wave velocity, Poisson's ratio also shows dominant fluid effect at the start of production that is followed by a dominant frame-stiffening effect. Poisson's ratio drops rapidly at the start, due to the release of gas from solution (which drops the p-wave velocity) and after that it drops at a slower rate, indicating a decrease in bulk to shear modulus ratio, due to the combined and competing effects of frame-stiffening (acting on both bulk and shear moduli) and fluid effects (acting only on bulk modulus).

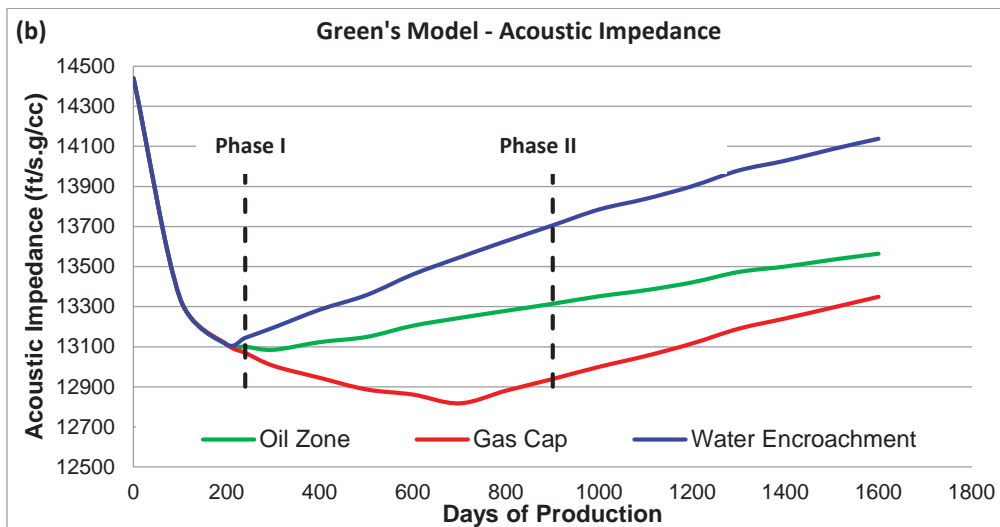
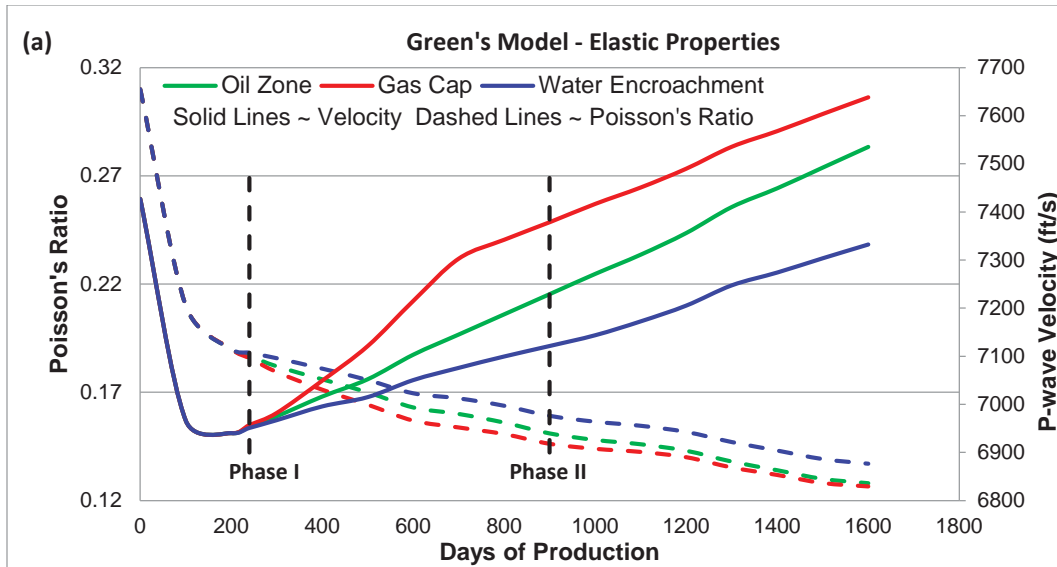


Figure 3. 7. Elastic properties of 4500-sand predicted by Green's model. (a) Plot of P-wave velocity (solid lines) and Poisson's ratio (dashed-lines) estimated from Green's model for oil zone (green), gas cap (red) and water-encroachment zone (blue). The initial rapid decrease in velocity is caused by the release of gas from the solution as the reservoir pressure dropped below bubble point shortly after production started. With continued production the frame-stiffening effect dominates over the fluid effect, causing a gradual increase in p-wave velocity. (b) Plot of acoustic impedance with time of production. The initial drop in acoustic impedance predicts a significant brightening from legacy to Phase I data in all zones for zero offset reflections. From Phase I to Phase II data the frame stiffening effect becomes dominant in oil-zone and water encroachment zone and a dimming effect should be observed at near offsets. The gas-cap is expected to exhibit a brightening effect at zero offset from Phase I to Phase II because of the density effect dominating over stiffening.

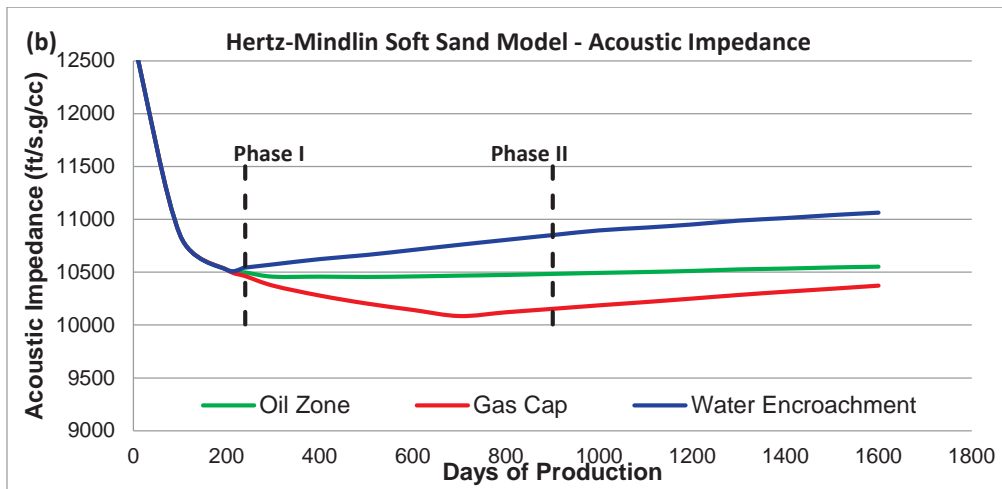
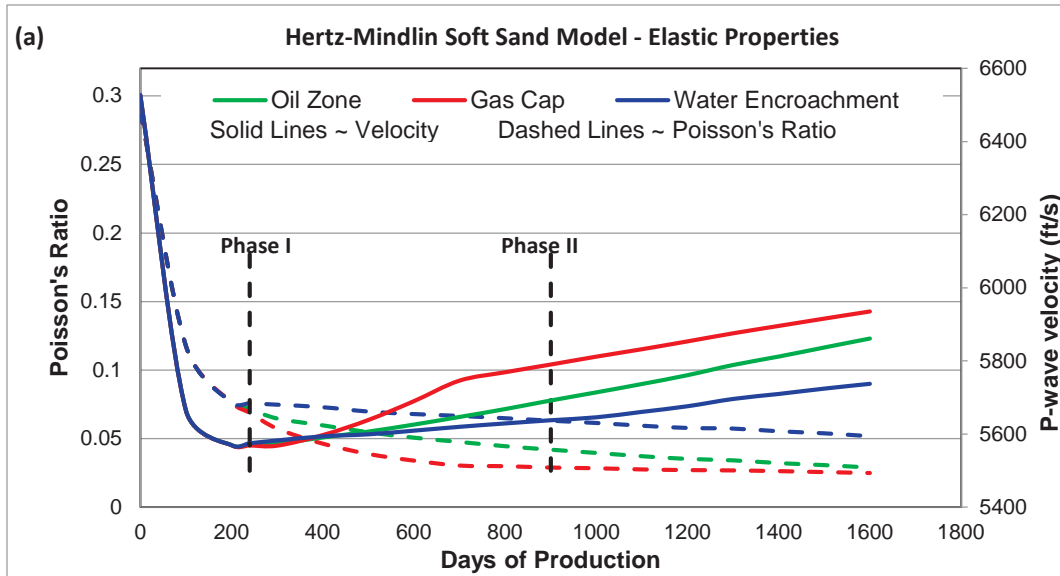


Figure 3. 8. Elastic properties of reservoir A predicted by Hertz-Mindlin model. (a) Plot of P-wave velocity (soled lines) and Poisson's ratio (dashed lines) of saturated 4500-ft sand as predicted from Hertz-Mindlin soft sand model against days of production. After predicting the dry-frame from Hertz-Mindlin model, the saturated rock properties were estimated by using Gassmann's substitution and fluid properties for oil zone (green), gas-cap (red) and water encroachment zone (blue). As compared to the Green's model results, the soft sand model predicts the lower velocities for the Teal South sand and also shows lower pressure dependence as compared to the Green's model. Note that Poisson's ratio predicted from Hertz-Mindlin model is too low to be realistic, because of the assumption of no slip at grain contacts. (b) The plot of model predicted acoustic impedance against the days of production. The graph suggests a dimming because of water-encroachment, slight dimming in oil zone and brightening in gas-cap at zero-offset from Phase I to Phase II.

Figure 3.9 shows the p-wave velocity and Poisson's ratio of the nearby or down-dip water sand plotted as a function of days of production, predicted using Green's model. Figure 3.10 gives a similar plot predicted by Hertz-Mindlin model.

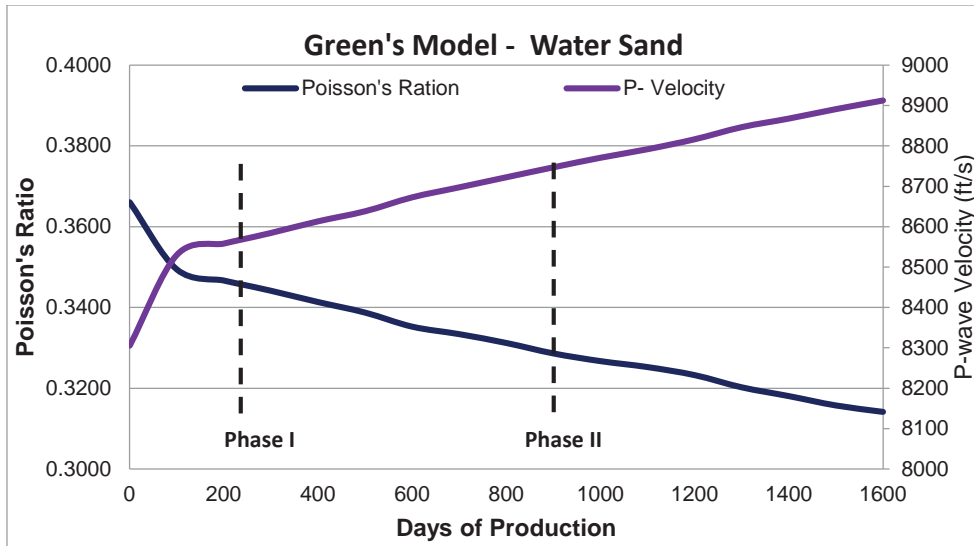


Figure 3. 9. P-wave velocity (purple) and Poisson's ratio (blue) for water sand estimated by Green's model plotted against days of production. For water sand, it is assumed that there was no change in fluid properties but only the frame stiffening with the decrease in pore-pressure caused by the production. The graph shows a rapid increase in p-wave velocity and decrease in Poisson's ratio at the start of the production, with more gradual changes with continuing production. As the density remains constant, acoustic impedance follows the shape of the p-wave velocity, implying a dimming at near offsets, especially significant at the start of the production.

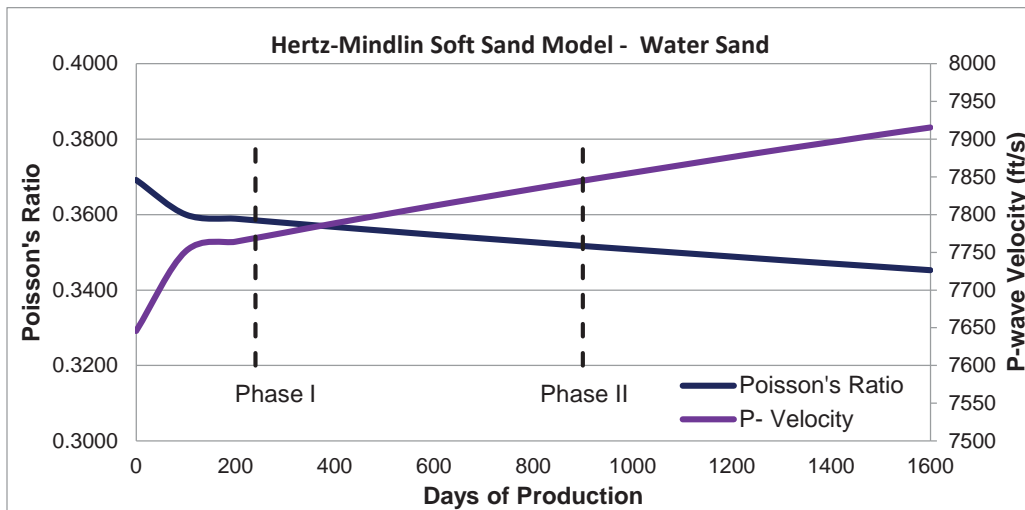


Figure 3. 10. Plot of p-wave velocity (purple) and Poisson's ratio (blue) of water sand computed by Hertz-Mindlin model against the days of the production. Note that like Green's model, the Hertz-Mindlin model also shows a sudden increase in velocity and a decrease in Poisson's ratio because of frame stiffening at the start of production associated with the sudden pressure drop caused by the fluid expansion. Comparison of figure 3.10 with figure 3.9 clearly demonstrates that Hertz-Mindlin model shows smaller sensitivity as compared to the Green's model.

The water sand, in contrast to the other zones, has negligible changes in fluid properties because there is no gas effect, and the primary factor affecting its elastic properties is the frame stiffening due to the pore-pressure drop. The water-sand is predicted to exhibit a rapid increase in p-wave velocity at the start of production, and a decrease in Poisson's

ratio, both of which continue at a lower rate with ongoing production, reflecting the rate of pressure change in the reservoir and nearby water sands.

Comparison of Figure 3.10 with Figure 3.9 & Figure 3.8 with Figure 3.7 shows that the Hertz-Mindlin model is less sensitive to pressure variations as compared to Green's model. Assuming a constant density of water sand for all phases of production, one can immediately conclude that water sand from the Teal South should show a continuous dimming effect at near offsets.

Figures 3.11 and 3.12 show the AVO curves for each zone estimated using Zoeppritz's equations and elastic properties estimated from Green's model and Hertz-Mindlin respectively. The CMP gathers generated from the AVO curves are given in Appendix D. The stacked seismic response generated by stacking CMP gathers over an angle range of  $0^{\circ}$  to  $30^{\circ}$  is displayed in Figures 3.13(a) and 3.14(a) with respective instantaneous amplitudes shown in Figures 3.13(b) and 3.14(b).

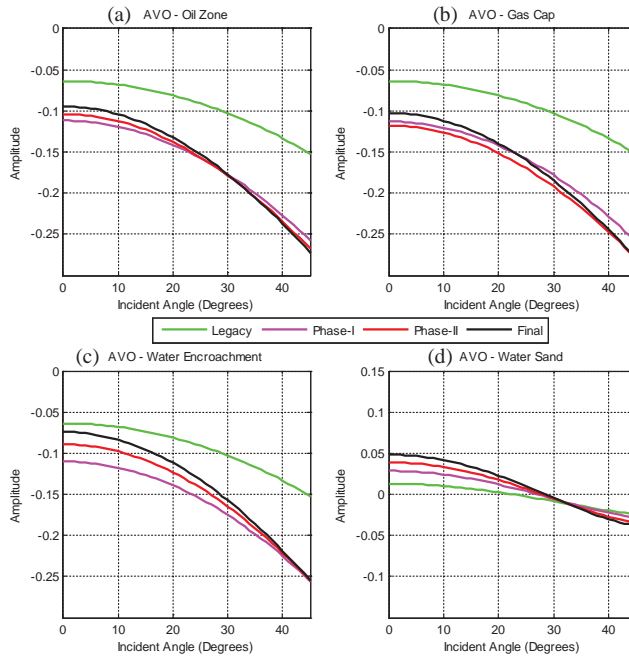


Figure 3. 11. AVO response of 4500-ft sand predicted from the rock properties estimated by Green's Model at different stages of production: before production [legacy (green)], Phase I (pink), Phase II (red), after complete depletion ("final", black). The AVO response is computed for four different cases: (a) AVO response for oil zone assuming that with production the oil saturation decreases gradually with an increase in gas saturation. (b) AVO response of gas-cap estimated assuming that with the production the gas saturation will increase rapidly reducing oil saturation while keeping water saturation constant. (c) AVO response for water encroachment zone assuming that with production formation water will replace the oil without changing gas-saturation after it reaches 10%. (d) AVO response of water sand, assuming 100% water saturation during all phases of production (note different vertical scale on this plot).

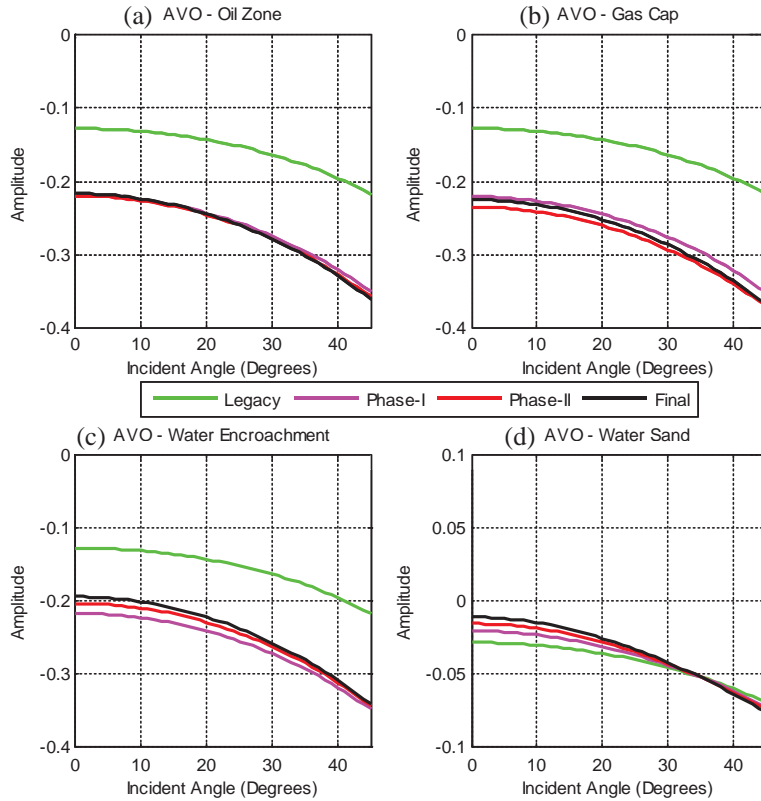


Figure 3. 12. AVO response of the 4500-ft sand using elastic properties predicted by Hertz-Mindlin model. The green line shows the AVO prediction for legacy, Phase I AVO is shown in magenta, Phase II is in red and the black line predicts the AVO response at the time of complete depletion. The AVO response are estimated using the Hertz-Mindlin predicted elastic properties of oil zone (a), gas cap (b), water encroachment zone (c) and water sand in full Zoeppritz's equation. The AVO trend predicts a clear and significant brightening from legacy to Phase I for all zones except water sand that predicts a dimming effect. From Phase I to Phase II, oil-zone shows no change at zero offset but brightens with offset. Gas cap shows almost constant brightening effect at all offset. Water encroachment shows the dimming effect that decreases gradually with offset and may start brightening at very far offset. Water sand also shows dimming effect at near offset that gradually decreases with offset, and appear as brightening effect at far-offset. (Note different vertical scale on this plot.)

### 3.5.1.1. Legacy to Phase I

The AVO curves from both models suggest that there will be a significant brightening effect at all offsets for all zones other than water-sand. This increase in reflection coefficient is mainly caused by the release of free gas from the solution as the reservoir was near bubble point at the time of the production. The brightening of reflections increases gradually with offset due, primarily, to frame stiffening. The increase in brightening with offset is comparatively less for Hertz-Mindlin model as compared to Green's model because of its lower pressure sensitivity. However, both models predict a significant brightening of reservoir 'A' on the stacked seismic section from Legacy to Phase I. It is consistent with our observation of increase in reflection strength over all zones of reservoir 'A' from legacy to Phase I (presented in chapter 2).

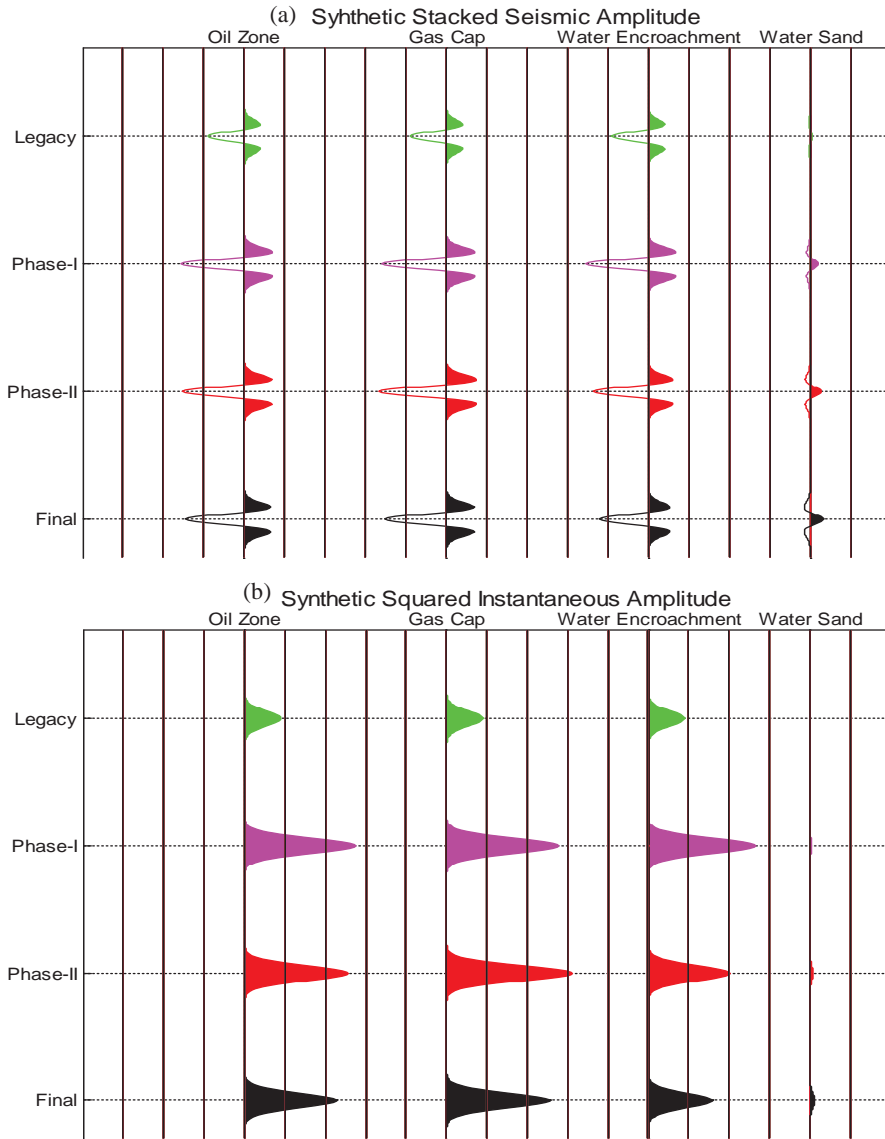


Figure 3. 13. Stacked seismic response predicted by Green's Model. (a) Synthetic stacked seismic wavelets based on elastic properties predicted by Green's Model. The stacked wavelet is estimated by stacking the CMP gather of figure D.1 over an angle range of 0-30°. (b) The squared instantaneous amplitude of the stacked wavelets of (a). The figure shows a significant brightening effect of stacked seismic section in all hydrocarbon zones from legacy (green) to Phase I (magenta) for all zones of reservoir 'A'. From Phase I to Phase II only the gas cap shows a modest increase in reflection strength while in the water-encroachment zone the stacked reflections dim considerably and little effect is predicted in the oil zone. In the water sand the stacked amplitude is very weak and changes in stacked amplitude and instantaneous amplitude of water sand are expected not to be visible on the actual data using these attributes.

Green's model (Figure 3.11 and Figure 3.13 (a)) predicts a small positive reflection coefficient for water sand at all offsets. In contrast to Green's model, Hertz-Mindlin model (Figure 3.12) predicts negative reflection coefficient for water sand that is consistent with our observations from the Teal South seismic data. Green's model, used by Pennington et al (2001), implies a small positive reflection, after making fluid

substitutions. This discrepancy is not significant here, since we are searching for changes with time, and the reflection amplitudes from the water sand are very small whether modeled as the previous paper implied, or with slightly different models equally consistent with the (poor-quality) log data.

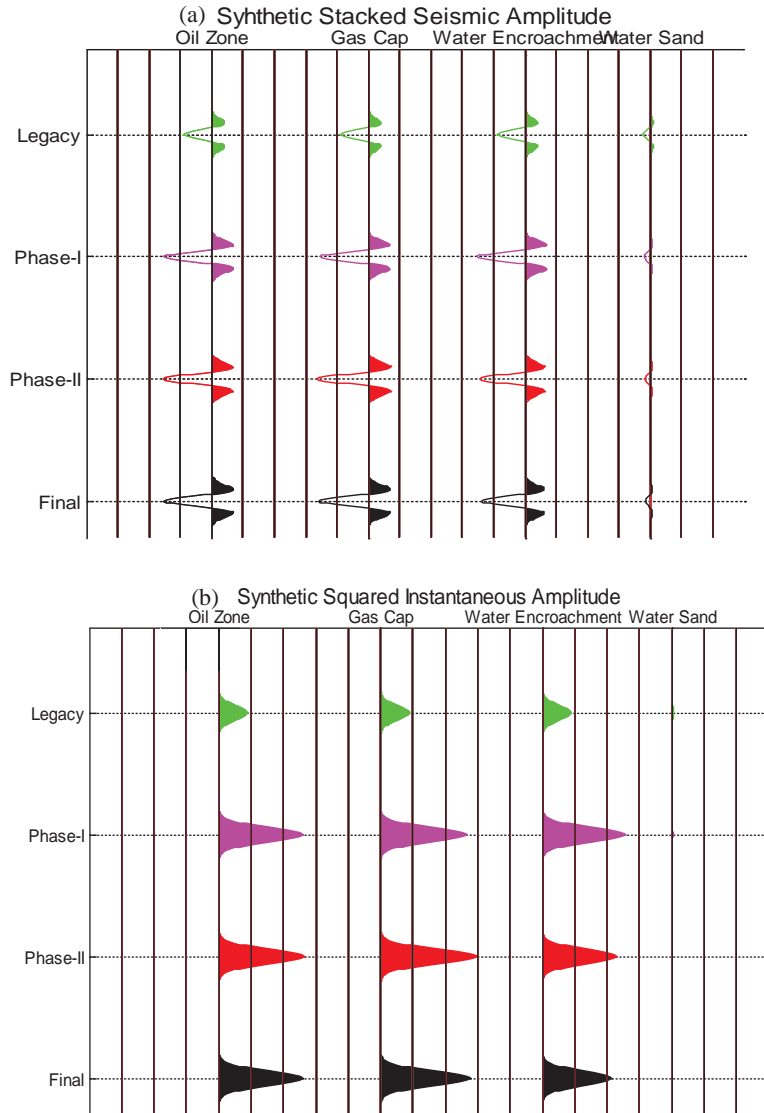


Figure 3. 14. Stacked seismic response predicted by Hertz-Mindlin model. (a) Synthetic stacked seismic section. The stacked seismic section is predicted by stacking the CMP gathers of figure D.2 over an angle range of  $0^{\circ}$ - $30^{\circ}$ . (b) Instantaneous amplitude computed from the stacked section by using the Hilbert's Transform. The figure shows a brightening of all zones from legacy to Phase I similar to Green's model. After Phase I, gas cap exhibits brightening and oil zone show no time-lapse change. This prediction agrees with time-lapse observations from reservoir C. Water encroachment causes dimming of reflections.

The AVO response of the water sand suggests that stacked output should exhibit a dimming effect (Hertz-Mindlin model - for water-sand having lower impedance than the

overlying shale) and brightening effect (Green's Model - for water-sand having higher impedance than the overlying shale). In contrast to AVO prediction, the time-lapse data do not exhibit any significant change from legacy to Phase I and Phase I to Phase II based on comparison of reflection strength (presented in chapter 2). Figures 3.13 and 3.14, however, explain this discrepancy. The water sand has a very small impedance contrast with the overlying shale so make very weak reflections. Because of the weak reflections, the time-lapse changes in water sand are not observable. CMP gather given in Appendix D (Figure D.1(e)) shows that water sand may have the highest fractional (percentage) changes over the production life of the reservoir but the absolute numbers are so small to be visible on stacked sections when plotted with bright reflections from reservoir.

Both models predict the time-lapse changes from Legacy to Phase I that are qualitatively consistent with the time-lapse observations from stacked section.

#### 3.5.1.2. Phase I to Phase II

Oil Zone: AVO curves of Green's model (Figure 3.11) shows that the reflections from oil zone dim at near offsets while brightening at far offsets. Within the angle range used for stacking ( $0^{\circ}$ - $30^{\circ}$ ), the model predicts only dimming that decreases with offset and the stacked output (shown in Figure 3.13) shows a net dimming effect. These results are opposite to our observations of reflection strength from Phase I to Phase II.

AVO response in oil zone predicted by Hertz-Mindlin model suggests almost no change at zero-offset that is consistent with our observation from the partial stacks prepared from the pre-stack seismic gathers, and is presented in Figure 3.5. At far offsets, the predicted curve shows very small (negligible) brightening with offset, and the slopes of predicted AVO curves from Phase I to Phase II show almost no change. This is because Hertz-Mindlin predicts a constant dry-frame  $V_p/V_s$  ratio in unconsolidated sands at all pressures. However, lab measurements as well as field observations demonstrate that dry-frame  $V_p/V_s$  ratio drops with increasing differential stresses (Duffaut and Landrø 2007). More detailed discussion on this discrepancy is given later. Synthetic stacked section and its squared instantaneous amplitude shows a little brightening of oil zone from the Phase I to Phase II. Though the observations of brightening are qualitatively consistent with the time-lapse measurements but model predicts much less brightening than actually observed from time-lapse stacked seismic data.

Gas Cap: Predicted AVO response of gas cap shows brightening at all offsets (Figure 3.11 and Figure 3.12), gradually increasing with offset as the frame-stiffening decreases Poisson's ratio. The net stacked amplitude and reflection strength (Figure 3.13 and Figure 3.14) show that the reflections from the gas cap will brighten from Phase I to Phase II. This conclusion is consistent with our observations of actual time-lapse data. But both models predict weaker time-lapse changes in gas cap compared to time-lapse changes

associated with the water-encroachment zone discussed below that contradict the observations.

**Water Encroachment Zone:** AVO curves for water-encroachment show that reflections dim at all offsets as production continues from Phase I to Phase II. The increase in water saturation and frame-stiffening both cause dimming, so the dimming intensifies. However, the reduction in reflection strength gradually decreases with offset as frame stiffening decreases the Poisson's ratio that makes Phase II AVO curve steeper than Phase I. The stacked amplitude for water encroachment zone shows a significant decrease in reflection strength, consistent with our observations from the Teal South data. But the model predicts the strength of time-lapse changes in water-encroachment zone stronger than the ones predicted for gas cap, opposite to our observations from the Teal South data where we observe strong time-lapse changes over the gas-cap and oil-zone with small changes from water-encroachment.

**AVO Gradient:** Figure 3.15 shows the modeled AVO curves plotted as a function of  $\sin^2\theta$  for oil-zone only. All four curves in both figures show the AVO response for oil zone only at different stages of production. This figure can be directly compared to the Figure 3.5 (a) that shows AVO trend observed on the field data. For comparison purposes, a linear fit is applied to Phase I and Phase II data on both figures and the ratio of their slopes was computed. Time-lapse seismic data from Phase I to Phase II from reservoir 'A' exhibit a ratio of 0.60 while Green's model predicts a ratio of 0.88 and Hertz-Mindlin model predicts a ratio of 0.93. I do not have CMP gathers for other zones so the analysis is limited to the oil-zone only. However, modelling results suggest that other zones should exhibit similar behavior. Both models were unsuccessful in predicting the AVO response change from Phase I to Phase II.

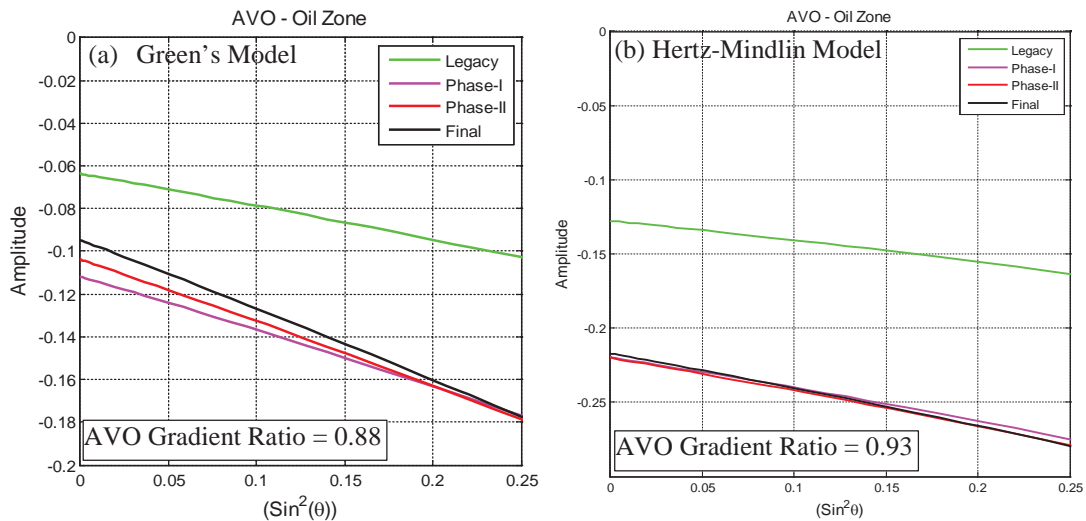


Figure 3. 15. Plot of modeled seismic amplitude of oil zone as a function of  $\sin^2(\theta)$ . (a) The AVO response is predicted using elastic properties estimated from Green's model. This plot shows an initial dimming that gradually diminishes at

far offset. (b) The AVO curves are predicted using the Hertz-Mindlin model for soft sand. The figure shows that there is no change in zero-offset reflection coefficient from Phase I to Phase II and no significant change in AVO gradient from Phase I to Phase II.

### 3.5.1.3. Summary

Rock physics models by Hertz-Mindlin and Green were used to estimate the elastic properties for the reservoir 'A' over the production life of the Teal South oil field. Models predict that with production from the reservoir pore-pressure decreases resulting into an increase in effective stress because of which the rock dry-frame stiffens. The pore-fluid also changes its elastic properties because of the release of free gas and fluid expansion under reduced pore-pressure. The fluid properties were estimated using the Batzle and Wang method. Gassmann's equations for fluid substitution were used to derive the elastic properties of the saturated rock from oil-zone, gas cap, water encroachment zone and water-sand. The elastic properties were then used to predict the AVO response of reservoir for different times of production. The resultant AVO curves suggest that reflection strength increases from legacy to Phase I generating brighter stacked amplitudes in Phase I as compared to legacy. It is consistent with our findings from the Teal South data.

From Phase I to Phase II, the gas cap shows brightening at all offset with a net 'brightening' effect on stacked amplitude, similarly the water encroachment dims at all offset and so gives a 'dimmer' stacked section. This prediction is consistent to our observations in terms of sign of time-lapse changes but the intensity of changes recorded on time-lapse data does not match with the intensity of the changes predicted by the models.

The two models predict different AVO response for Oil zone. Green's model predicts dimming at near offsets while brightening at far-offset making a net dimming effect on the stacked section while Hertz-Mindlin model predicts no time-lapse change at zero-offset but slight brightening at far offset making a net brightening effect on stacked section. The stacked field data, in contrast, exhibit strong brightening effects. Both models under-predict the change in AVO gradient of oil zone from Phase I to Phase II.

Modelling results show that water sand exhibits very weak reflections so time-lapse changes are of very small magnitude, and when we compute the instantaneous amplitude and square it the changes becomes even weaker so remain invisible. It is because of this fact that we do not see any time-lapse changes in water sand.

Green's model over-predicts the elastic properties of the dry-frame. It has not been able to predict the changes in AVO gradient as observed from the time lapse data and reported by Pennington et al. (2001). The model is based on empirical data that was mostly composed of competent rocks, in contrast to the 4500-ft sand that is composed of unconsolidated sand. Most models based on empirical data from lab measurements made on consolidated, moderately porous, normally pressured rock samples will produce

results similar to Green's model used here. 4500-ft sand is unconsolidated, highly porous and over-pressured sand, and such models may not be appropriate for unconsolidated rocks like 4500-ft sand.

Hertz-Mindlin model works well in unconsolidated rocks like 4500-ft sand. Using a coordination number of 8 and an initial porosity of 40%, the model defines the elastic properties that match to the available well-logs within limited accuracy of the data. A little over-prediction is observed that is most likely due to the assumed no slip at grain contacts. The time lapse changes predicted by the Hertz-Mindlin model are partially consistent with the observed changes from reservoir 'A'. The mismatch between predictions and field data are due to the fact that field data exhibit a strong change in AVO gradient and Hertz-Mindlin model under isotropic conditions does not predict that strong changes in AVO gradient. The model predicts that ratio of AVO gradient from Phase I to Phase II is about 0.93 in contrast to the observed ratio of 0.60.

Time-lapse predictions for oil-zone and gas cap by Hertz-Mindlin model are consistent with the time-lapse observation of reservoir 'C' reported in chapter 2; brightening of gas cap with negligible time-lapse changes in oil-zone.

### **3.5.2. Effects of Friction and Pressure Dependence on AVO Gradient**

#### **3.5.2.1. Sensitivity to Friction at Grain Contacts**

According to Zoeppritz equations, the change in reflection coefficients with offset for incident angles in the intermediate range ( $15^{\circ}$ - $30^{\circ}$ ) are mainly controlled by the Poisson's ratio or  $V_p/V_s$  ratio. Shuey (1985) demonstrated that a plot between the p-p reflection coefficient ( $R_{pp}$ ) against  $\sin^2\theta$  generates a linear trend in his approximation, the slope of which depends upon the Poisson's ratio or  $V_p/V_s$  ratio of layers across the interface. Field data from Teal South exhibit a significant drop in Poisson's ratio (increase in AVO gradient) from Phase I to Phase II but Hertz-Mindlin model results show a very small change in Poisson's ratio. Similar discrepancies have been reported in the literature (Bachrach, Dvorkin, and Nur 2000, Duffaut and Landrø 2007). The most common explanations suggest that friction at grain contacts changes and pressure dependence of the Hertz-Mindlin model changes with differential stresses (Goddard 1990, Bachrach, Dvorkin, and Nur 2000, Duffaut and Landrø 2007). Duffaut and Landrø (2007) reported a similar discrepancy between modeled and AVO-determined  $V_p/V_s$  ratio based on some core-measurements and time lapse AVO data in response to increased pore-pressure caused by injection. They suggest that the change in  $V_p/V_s$  ratio happens because of the change in consolidation with pressure. They use the coordination number as a fudge factor to get a best fit to the data, and define it as 'consolidation parameter'. Bachrach, Dvorkin, and Nur (2000), Huffman and Castagna (2001) and Prasad (2002) also reported an increase in compressional to shear velocity ratio with decreasing differential stresses. Zimmer (2004) analyzed various reasons for this, and concluded that it is most likely the

slip or rotation at grain contacts that cause this discrepancy. He also demonstrated that change in coordination number (as suggested by Duffaut and Landrø (2007)) cannot change  $V_p/V_s$  ratio enough to match his experimental results. Zimmer postulated that with increased confining stress the grains are better locked against each other resulting into an increase in friction at grain contacts. The better interlocking of grains increases the shear strength of the dry-frame without affecting bulk modulus so cause a significant decrease in the Poisson's ratio and  $V_p/V_s$  ratio.

A similar process could be the reason behind the discrepancy between Teal South AVO measurements and predictions. The Teal South reservoir was overpressured at discovery, and was yet overpressured when Phase I data were acquired. The higher pore-pressure could have decreased the grain to grain contacts. With the continued production, the pore-pressure decreased and the grains may have better locking at Phase II than Phase I resulting into an increase in friction factor that could have decreased the Poisson's ratio in Phase II.

In order to test this scenario, I predicted the elastic properties from Hertz-Mindlin using different values of friction factors. For this purpose, I used the Hertz-Mindlin's equation modified by Mavko, Mukerji, and Dvorkin (1998) and is given below to compute the shear modulus while bulk modulus remains unchanged.

$$\mu'_{HM} = \frac{2 + 3f - \nu(1 + 3f)}{5(2 - \nu)} \left[ \frac{3C^2(1 - \phi)^2 \mu^2}{2\pi^2(1 - \nu)^2} P \right]^{1/3} \quad (3.2)$$

Figure 3.16 shows the p-wave velocities and Poisson's ratio as predicted for different values of friction. For this graph, I used the properties for oil-zone only. The only parameter changing between different curves is the friction factor. All other parameters are kept constant. The figure shows that with increase in friction factor compressional velocity increases but Poisson's ratio decreases.

It turns out that friction factor will not have a significant impact on the stacked amplitude. Increase in friction factor where increases the slope of the AVO response because of lower Poisson's ratio making brightspots even brighter it also decreases the magnitude of zero-offset reflections (for class III AVO) because of increased p-wave velocity (Figure 3.17). The net results of adding friction factor on stacked section is dimming rather than brightening. However, friction factor has potential to impact the AVO gradient significantly. For reservoirs with higher coordination number and lower porosity, the change in AVO response because of change in friction factor will be even more significant. The 4500-ft sand does not seem having any change in friction factor.

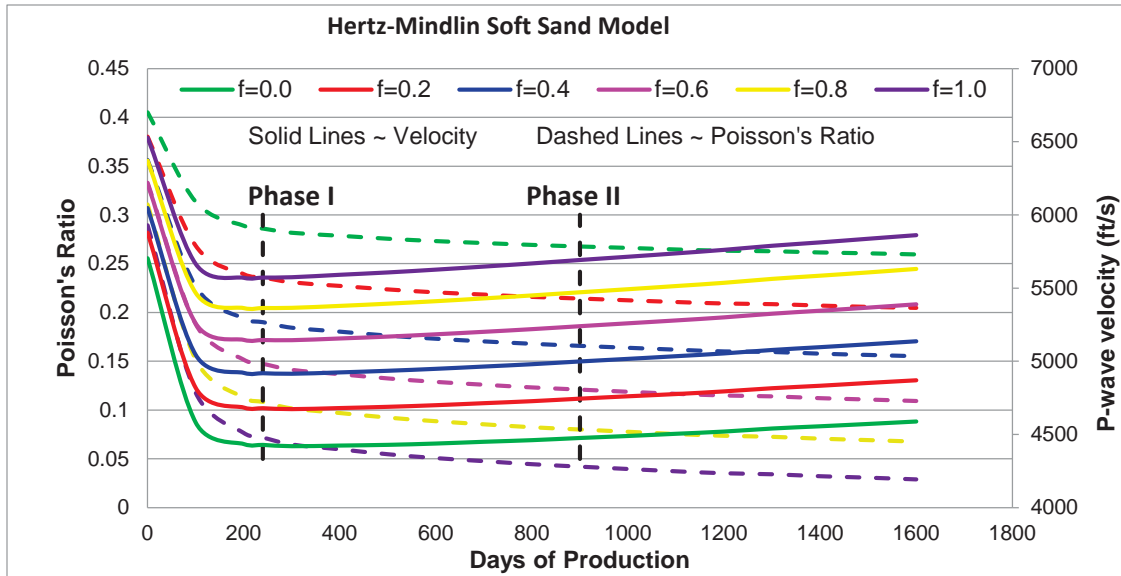


Figure 3. 16. Elastic properties estimated by Hertz-Mindlin model using different values of friction factor ( $f$ ). All other factors are kept constant. The curves are predicted using properties for Oil zone only. Note from the figure that increase in friction factor decreases Poisson's ratio but it also increases the compressional velocity.

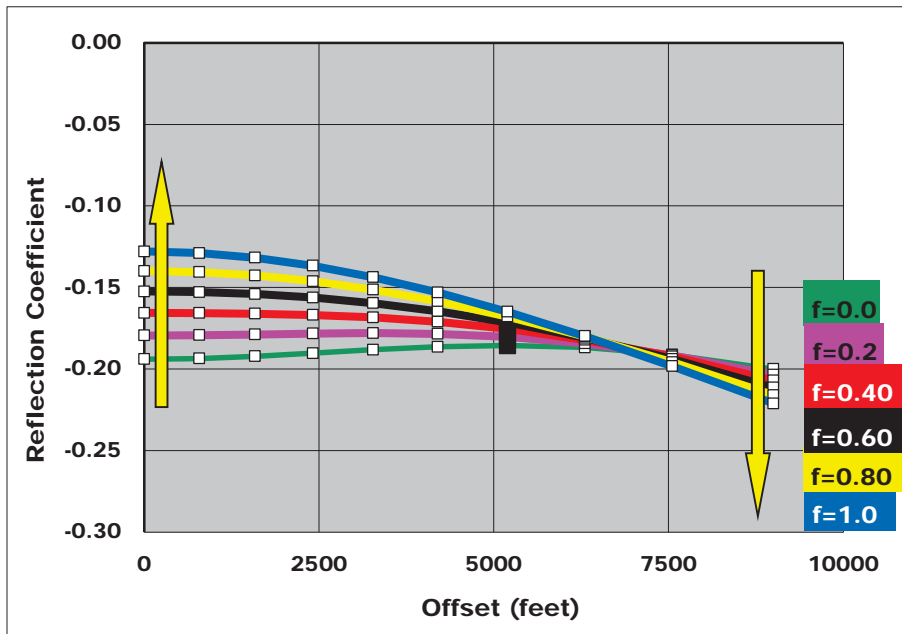


Figure 3. 17. Analysis of effects of friction factors on AVO response. Each curve represents AVO response for a different assumed friction coefficient. All properties used in modeling AVO trend are kept constant for each curve except the friction factor. The curves are estimated for oil-zone under Phase II pressure conditions showing that with increased friction at grain contacts the slopes of AVO curves increase, but the zero-offset reflection coefficient also decreases. The degree of decrease in zero-offset reflections seems more pronounced than the net effect of steepening of slope. The stacked output then may show dimming as friction increases from Phase I to Phase II. The white square in the figure marks every 5 degree increase in angle of incidence and the black square marks 30 degrees.

### 3.5.2.2. Analysis of Pressure Dependence of the Hertz-Mindlin Model

Zimmer (2004) and Duffaut and Landrø (2007) have reported that the Hertz-Mindlin model shows lower pressure dependence of elastic moduli than lab measurements. The former also suggests that pressure dependence observed in lab measurements may decrease from  $P^{1/2}$  to  $P^{1/3}$  as effective stress increases. Goddard (1990) postulated that the increase in pressure dependence could be because of the non-spherical natural of grains or because of the change in co-ordination number with pressurization. He further added that transition of pressure dependence from  $P^{1/2}$  to  $P^{1/3}$  was also observed by Duffy and Mindlin (1957).

In order to evaluate the effect of change in pressure dependency, I rewrote the Hertz-Mindlin relations by replacing the constant exponent  $1/3$  with variable 'n'. The Hertz-Mindlin equations then become:

$$K_{HM} = \left[ \frac{C^2(1-\phi_0)^2 G^2}{18\pi^2(1-\nu)^2} P \right]^n \quad (3.3)$$

$$G_{HM} = \frac{5-4\nu}{5(2-\nu)} \left[ \frac{3C^2(1-\phi_0)^2 G^2}{2\pi^2(1-\nu)^2} P \right]^n \quad (3.4)$$

Where

'n' defines the pressure dependence of Hertz-Mindlin relation. According to contact law,  $n=1/3$ , but I used different values for 'n' ( $n=1/2, 1/3, 1/4, 1/5$  and  $1/6$ ) and estimated the dry-frame properties using equations 3.3 and 3.4. All other properties were kept constant. Model-predicted p-wave velocities and Poisson's ratios for different values of power exponent 'n' are given in Figure 3.18(a). The figure shows that compressional velocity increases with an increase in exponent and Poisson's ratio decreases.

If it is assumed that pressure dependency of 4500-ft sand decreases with an increase in confining stress based on previous work reported in literature (Goddard 1990, Zimmer 2004, Duffaut and Landrø 2007), then Figure 3.18 suggests that the Poisson's ratio from Phase I to Phase II should increase in contrast to our observation of decrease in Poisson's ratio from Phase I to Phase II (Figure 3.4 and 3.5). Increase in pressure dependence seems improbable as no scenario that may explain a possible increase in pressure dependence has been proposed. Figure 3.18 also suggests that for pressure exponents higher than  $1/3$  the model predicts negative Poisson's ratio (e.g., for  $n=1/2$ ).

Figure 3.18(b) shows the AVO response as predicted from the Hertz-Mindlin model by using different values for exponent. The figure shows that with an increase in exponent, the zero-offset reflections dim for a typical class III AVO though the gradient of AVO curve increases suggesting a lower Poisson's ratio. The stacked output will then show a dimming effect from lower pressure dependence to higher pressure dependence. In case of transition from higher to lower pressure dependence, the slope of the AVO curve will

decrease suggesting an increase in Poisson's ratio that is opposite to our observation from the Teal South AVO. Changing pressure dependence (increasing or decreasing) in the Hertz-Mindlin model does not help to predict the time-lapse AVO change.

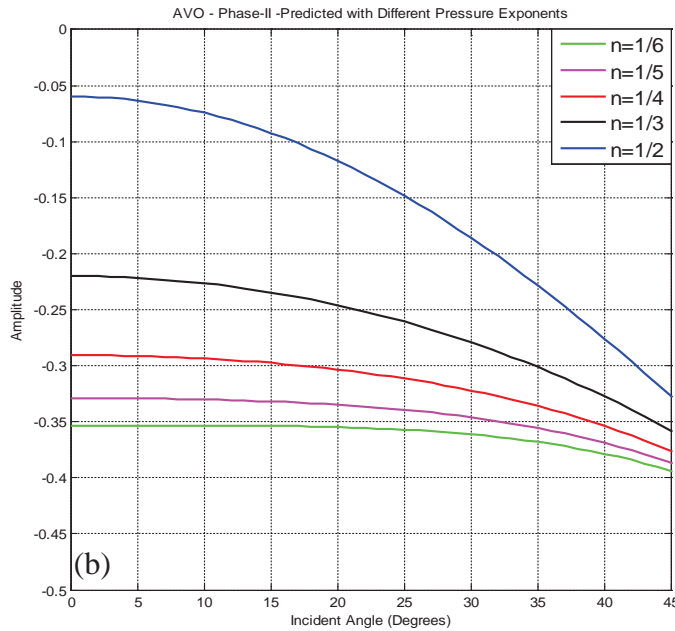
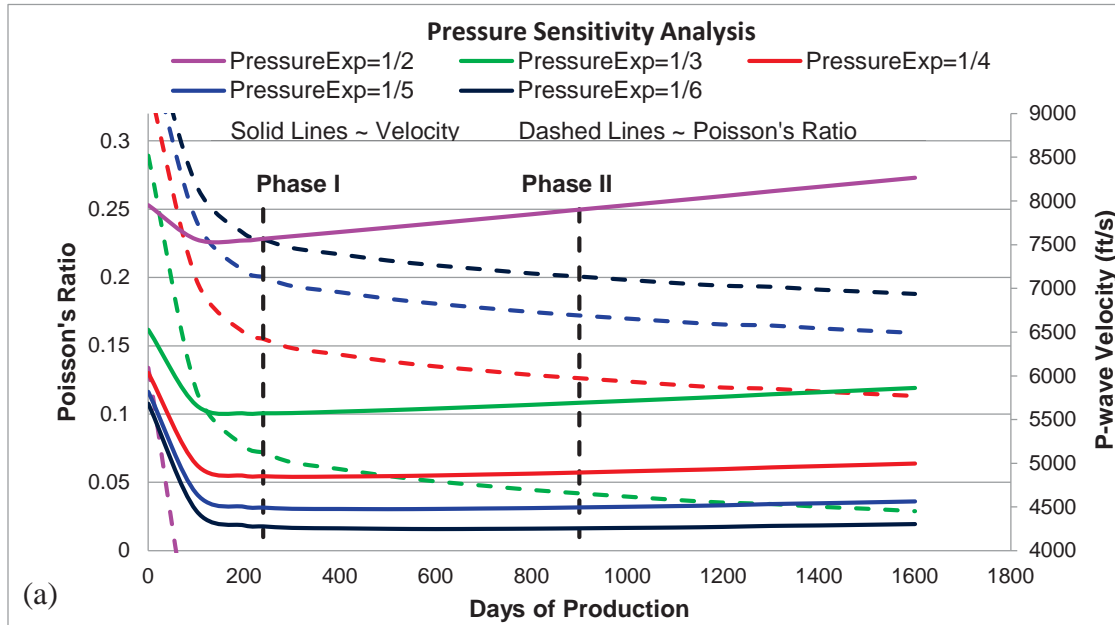


Figure 3. 18. Pressure dependence sensitivity of the Hertz-Mindlin Model. (a) Plot of compressional velocities and Poisson's ratio with days of production predicted with different pressure exponents ('n'). Pressure dependence is greater for higher values of 'n'. Compressional velocity increases with pressure exponent while Poisson's ratio decreases with pressure exponent. (b) AVO response predicted from the elastic properties shown in (a). The figure shows that reflection co-efficient brightens at lower pressure exponent but the slope of the AVO curve decreases, in disagreement with observations at Teal South.

### 3.5.2.3. Summary

I evaluated the effects of changes in friction factor and pressure dependency on AVO predictions. The modelling results suggest that by changing these parameters one may be able to predict the time-lapse change in AVO gradient with a reasonable accuracy but such changes will be accompanied by an over-prediction of zero-offset reflection-coefficients (decrease in magnitude of negative reflection coefficient in the Teal South example). It is observed that change in zero-offset reflections is more than the resultant AVO gradient change. The final predicted stack output then show dimming in contrast to the field observations of brightening.

The standard Hertz-Mindlin model for soft sand has accurately predicted the zero-offset reflection coefficient for the Teal South. The change in time-lapse AVO observed in the Teal South data cannot be modeled by using Hertz-Mindlin model under isotropic conditions.

### 3.5.3. Walton's Model for Anisotropic Unconsolidated Sands

After attempting all possible scenarios under isotropic conditions, I performed AVO modelling assuming anisotropic conditions for Phase II. I computed the Thomsen parameters for uniaxial compaction conditions. One of the parameters required for this purpose is strain along the vertical axis. This parameter is not known with certainty, but fortunately it does not affect the Thomsen parameters which turn out to depend on stress ratios, which are fixed for uniaxial compaction, regardless of the actual strain. Using sand properties similar to the ones used in Hertz-Mindlin model, the following values for Thomsen parameters are found for uniaxial compaction:

Rough Model (no slip at grain contact,  $f=1$ )

$$\varepsilon=-0.25; \quad \gamma= -0.168; \quad \delta=-0.200;$$

For smooth model, the Thomsen's parameters are constant under uniaxial compaction independent of the material, and their values are:

Smooth Model (no friction,  $f=0$ )

$$\varepsilon=-0.3125; \quad \gamma= -0.25; \quad \delta=-0.208;$$

The model suggests values of Thomsen's anisotropy parameters for all non-zero values of vertical strain under uniaxial compaction that depend only on the elastic properties of the matrix/mineral. Bandyopadhyay (2009), however, states that anisotropy of a rock under uniaxial compaction is entirely controlled by variation of porosity and coordination number with increasing strain, a result not consistent with the results obtained here. An important aspect to note is that under uniaxial compaction all Thomsen parameters are negative. The smooth model always predicts higher values of anisotropy parameters than the rough model.

I also computed the Thomsen's parameters for 4500-ft sand assuming triaxial compression rather than uniaxial compaction for reasonable values of compression. To determine Thomson's parameters under triaxial compression, we need to know strain anisotropy i.e., the ratio between the strain along vertical axis and strain along horizontal axis ( $E_{11}/E_{33}$ ). Along the horizontal axis, either there was no deformation (uniaxial compaction) or it was so small to be seen so ( $E_{11}=E_{22}\approx 0$ ). I conclude the following limits for triaxial compression:

$$0 \leq E_{11}/E_{33} \ll 1$$

Anisotropy parameters for a range of values of  $E_{11}/E_{33}$  were computed, and the parameters were estimated assuming rough contacts and smooth contacts, plotted as a function of  $E_{11}/E_{33}$  in figure 3.19. The anisotropy parameters increase in magnitude with an increase in strain ( $E_{11}/E_{33}$ ) ratio but the rate of increase in anisotropy decreases, and after  $E_{11}/E_{33}$  ratio of 0.01 the anisotropy parameters is nearly constant. The figure also shows that model with smooth grain contacts ( $f=0$ ) always predicts higher anisotropy than the rough model ( $f=1$ ).

It is reasonable to assume that in most compacting reservoirs,  $E_{11}/E_{33}$  will be much less than 0.01, and I picked the following values of anisotropic parameters for my modelling purposes.

Rough Model:

$$\varepsilon = -0.1243$$

$$\delta = -0.1243$$

$$\gamma = -0.0708$$

Smooth Model:

$$\varepsilon = -0.1647$$

$$\delta = -0.1647$$

$$\gamma = -0.0986$$

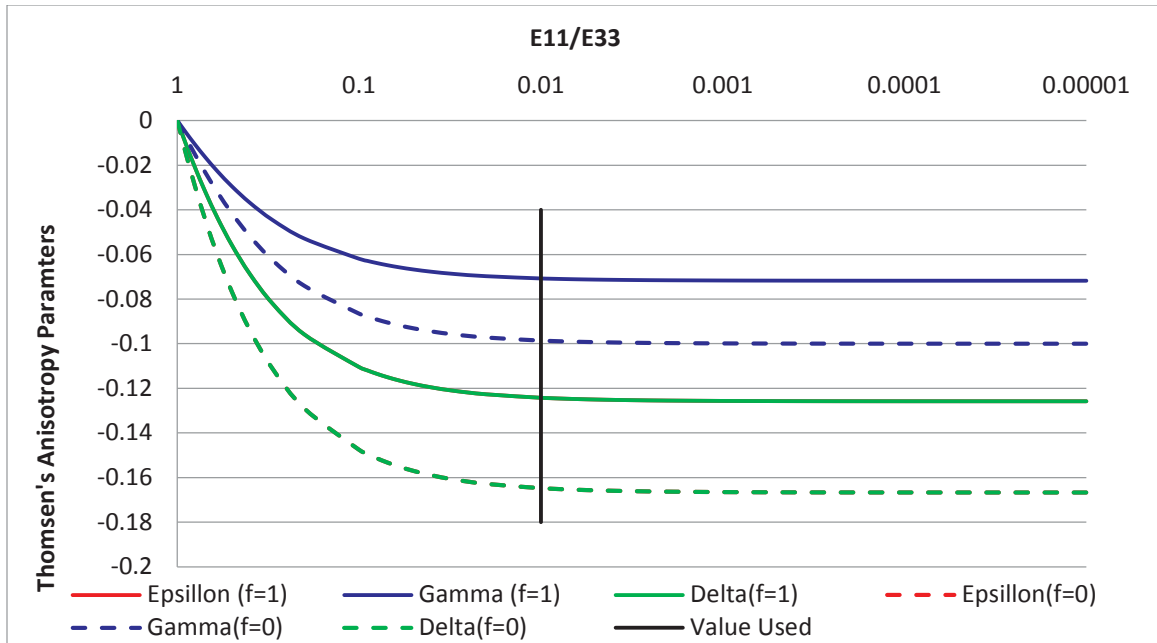


Figure 3. 19. Plot of Thomsen's parameter with the strain anisotropy ( $E_{11}/E_{33}$ ). Logarithmic scale is used on x-axis to cover the wide range of strain ratios. The solid lines show the anisotropy parameters estimated for rough model that assumes no slip at contact ( $f=1$ ) and dashed lines show the anisotropy parameters for smooth model that assumes frictionless contacts ( $f=0$ ). Under triaxial compression with  $E_{11}=E_{22}$ , the model predicts equal values for the Thomsen's parameters ' $\epsilon$ ' (red) and ' $\delta$ ' (green). The red curves representing ' $\epsilon$ ' are hidden under the green curves of ' $\delta$ '. The graph shows that all the magnitudes of all anisotropy parameters increase with an increase in strain anisotropy, and after a certain value ( $\sim 0.01$ ) of  $E_{11}/E_{33}$ , the anisotropy parameters are nearly constant. The black solid line marks the value of anisotropy parameters used for the Teal South modeling in this study.

Though I computed the Thomsen's parameters for rough and smooth model both, but in AVO modeling I used the values only for the rough model. Smooth contacts always predict the higher anisotropy so with rough model we will be able to describe a base case successfully.

### 3.5.3.1. AVO Response Assuming Uniaxial Compaction

Using the Thomsen's parameters, estimated for uniaxial compaction, and effective elastic properties predicted by the standard Hertz-Mindlin model in Rüger's approximation, I computed the AVO curves under anisotropic conditions.

Figure 3.20 shows AVO response of all zones of 4500-ft sand. AVO curves for legacy and Phase I are computed assuming isotropic conditions. AVO curves computed at the time of Phase II and complete depletion are estimated using the Thomsen's parameters ( $\epsilon=0.2514$ ,  $\delta=0.16798$ ,  $\gamma=0.200$ ) computed for uniaxial compaction condition. Addition of anisotropy after Phase I has increased the AVO gradient significantly.

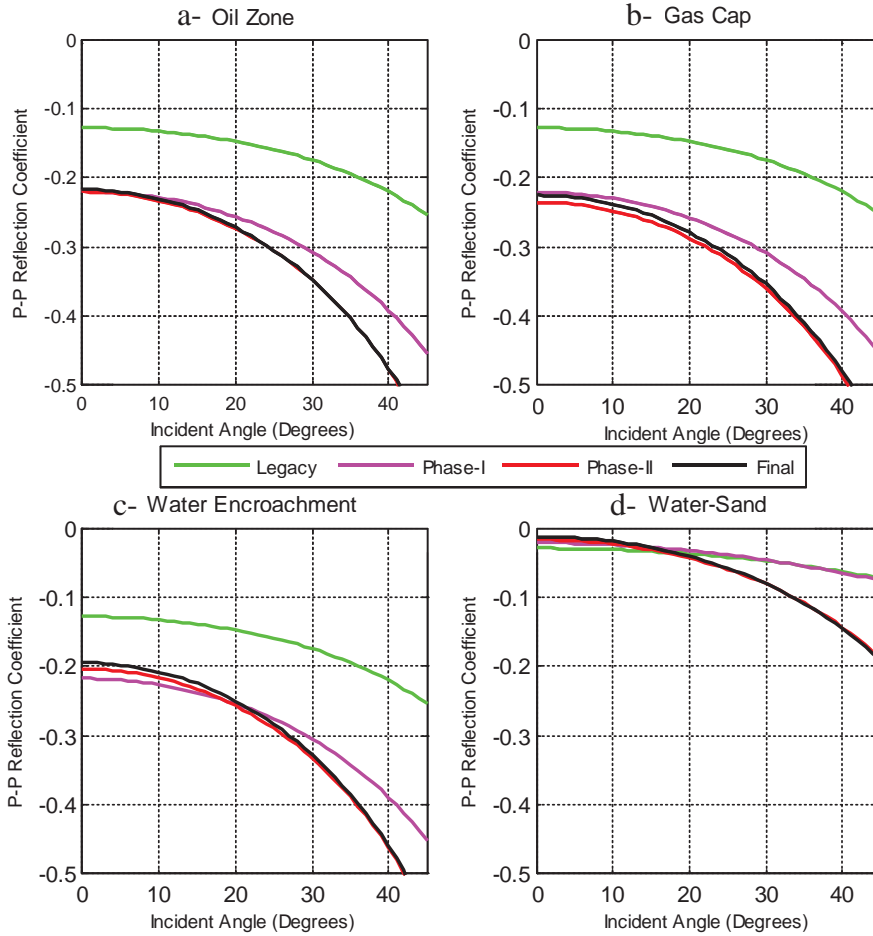


Figure 3. 20. AVO response under anisotropic conditions caused by uniaxial compaction. AVO curves are estimated assuming isotropic conditions for legacy (green) and Phase I(magenta) and anisotropic (uniaxial) conditions for Phase II (red) and final depletion (black). The Thomsen anisotropy parameters used for the AVO response prediction are estimated for 4500-ft sand reservoir assuming uniaxial compaction. Fluid substitution uses Gassmann’s (1951) relation for uniform saturation. Addition of anisotropic parameters significantly changes the slopes of the AVO curves for Phase II and final depletion. The slope change from Phase I to Phase II in oil zone now seems similar to the AVO trend of the time-lapse data shown in Figure 3.5.

The AVO curves for oil zone now show that there will be negligible change in reflection strength at zero-offset from Phase I to Phase II, and the AVO gradient increases significantly from Phase I to Phase II indicating continuous increase in brightening with offset. Assuming isotropic conditions, we were unable to predict the time-lapse changes in AVO gradient but addition of anisotropy has successfully predicted the change in AVO gradient from Phase I to Phase II. Figure 3.21 shows a plot of modeled amplitude versus  $\sin^2\theta$  for oil zone. Predicted AVO response matches with the field AVO response very closely. Like previous models, AVO gradient ratio was computed between Phase I and Phase II. The ratio for the predicted AVO response is 0.65 that is very close to 0.60, the gradients ratio computed from prestack time-lapse seismic data.

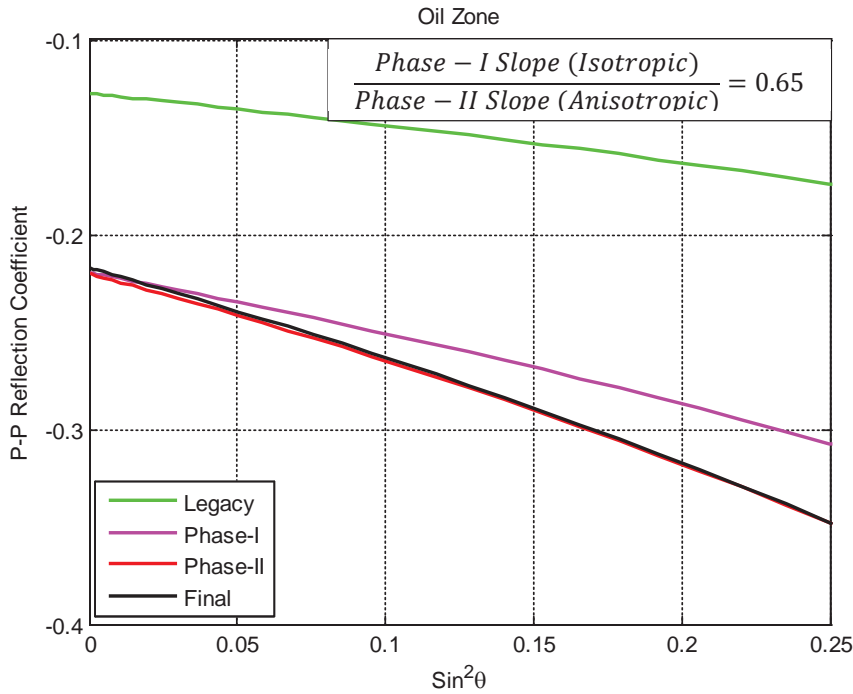


Figure 3. 21. Modelled amplitude for oil zone of reservoir ‘A’ versus Sin<sup>2</sup>θ assuming anisotropic (uniaxial) conditions for Phase II data. The elastic properties of 4500-ft sand estimated by Hertz-Mindlin Model (shown in figure 3.8) and the Thomsen’s parameters estimated from Walton’s model, assuming uniaxial compaction, are used in Rüger (1997) approximation to compute the P-P reflection coefficient for different angles of incidence. The AVO curves of Phase I and legacy assume isotropic conditions (i.e.  $\epsilon=0$ ,  $\delta=0$ ,  $\gamma=0$ ). Thomsen parameters used for Phase II and final curves are  $\epsilon=-0.2514$ ,  $\delta=-0.16798$ ,  $\gamma=-0.200$ .

The stacked amplitude computed from the modeled AVO curves is given in Figure 3.22 (a) with its squared instantaneous amplitude in Figure 3.22(b). The stacked seismic section predicts a significant brightening of all zones from legacy to Phase I except in the water-sand. From Phase I to Phase II, the model predicts a significant brightening of oil zone and gas cap, consistent with the recorded seismic data. According to our model as the water encroaches into the reservoir, the reflections may dim quite a bit but the dimming is hardly visible on the predicted response. Similarly models suggests almost no time-lapse changes observable in the water sand.

The results suggest that anisotropy increases AVO gradient causing a significant brightening of stacked amplitude in oil zone and gas cap where the models under isotropic conditions predict no significant changes.

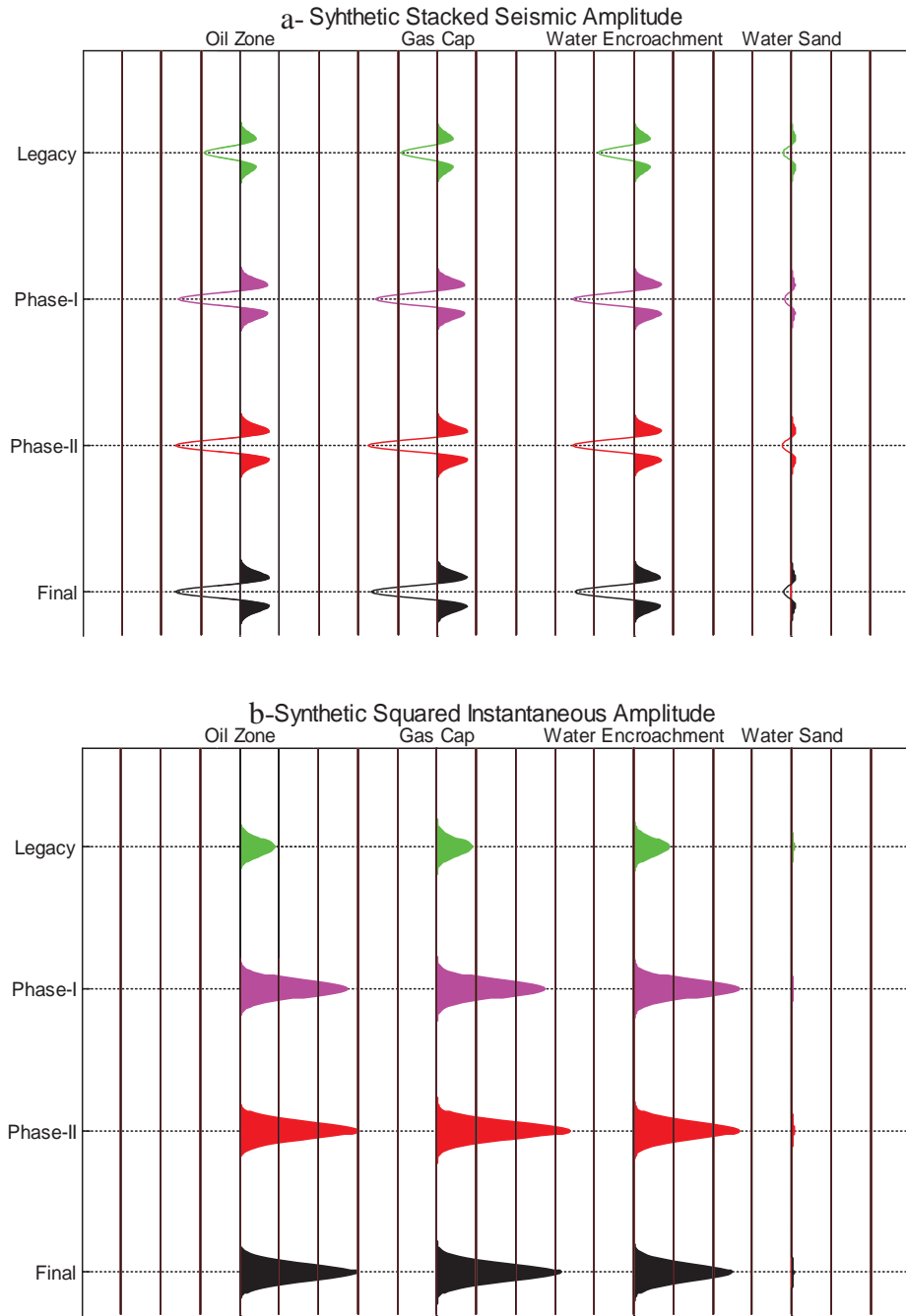


Figure 3. 22. Stacked seismic response predicted by Hertz-Mindlin model assuming anisotropic (uniaxial) conditions for Phase II data. (a) Stacked seismic amplitude computing from the AVO response of Figure 3.20. The AVO response was convolved with a 40 Hz Ricker wavelet to generate a synthetic CMP gather that is stacked over an angle range of  $0^{\circ}$  to  $30^{\circ}$ . Note that the seismic response shows continuous brightening of oil-zone and gas cap from Phase I to Phase II that is consistent with our field observations. The water encroachment shows a little bit of dimming that is hardly visible, and water sand shows almost no change. All these predictions and the predicted response from legacy to Phase I are perfectly consistent with the time-lapse data from the Teal South. (b) Squared synthetic instantaneous amplitude computed from the stacked seismic amplitude given in figure 3.22(a).

### 3.5.3.2. AVO Response under Triaxial Compression

As in the uniaxial compaction case, AVO curves were also computed using Thomsen anisotropy parameters for triaxial compression case with small lateral strains and are given in Figure 3.23. Overall the addition of anisotropy for Phase II modelling predicts the results that match more closely with the stacked seismic data and unmigrated partial stacks (Figures 3.4 & 3.5).

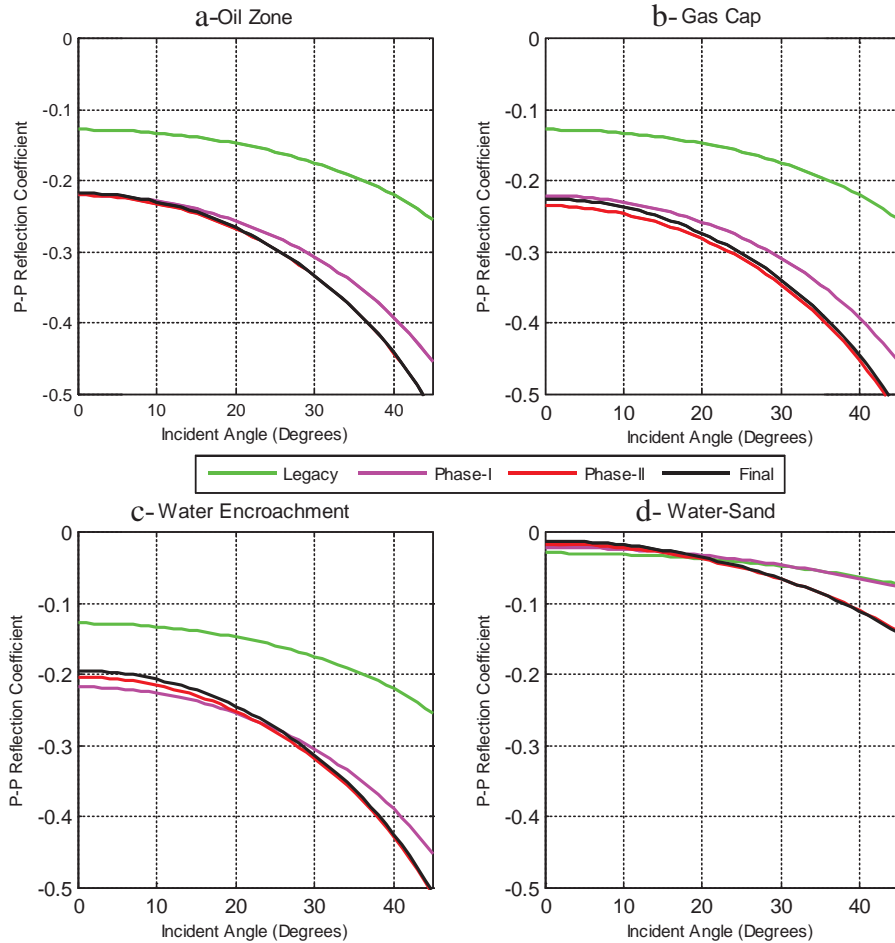


Figure 3. 23. AVO curves predicted assuming triaxial compression. The AVO curves for legacy (green) and Phase I conditions (magenta) conditions are estimated assuming isotropic medium. The AVO curves for Phase II (red) and complete depletion (black) are estimated by adding Thomsen parameters for a weak transverse anisotropic medium under triaxial compression. The values for Thomsen's parameters used are:  $\epsilon=-0.1243$ ,  $\gamma=-0.0708$ , and  $\delta=-0.1243$ . (a) The AVO curves for oil zone shows no time-lapse change at zero-offset and then continued brightening at far offset that increases with offset. (b) The gas cap response shows brightening at near offset that increases with offset. (c) The water encroachment zone shows dimming at near offset that gradually decreases with offset and ultimately turns to brightening at far offset. (d) Water sand shows dimming at near offset that decreases with offset and then ultimately turns into brightening at far offset. (Note the different scale in this plot)

AVO response from oil zone shows an increase in brightening from legacy to seismic. From Phase I to Phase II AVO curves show no time-lapse change at zero-offset but with increasing offset reflections brighten in Phase II. The trend in general is in agreement

with the AVO response from the seismic data shown in Figure 3.5, but brightening effect observed on the partial stack is a little stronger than predictions. Figure 3.24 shows the AVO trend of oil zone as a function of  $\sin^2\theta$ . Model predicts that the ratio of AVO gradient from Phase I to Phase II is about 0.76, close to the gradient ratio observed from the time-lapse data.

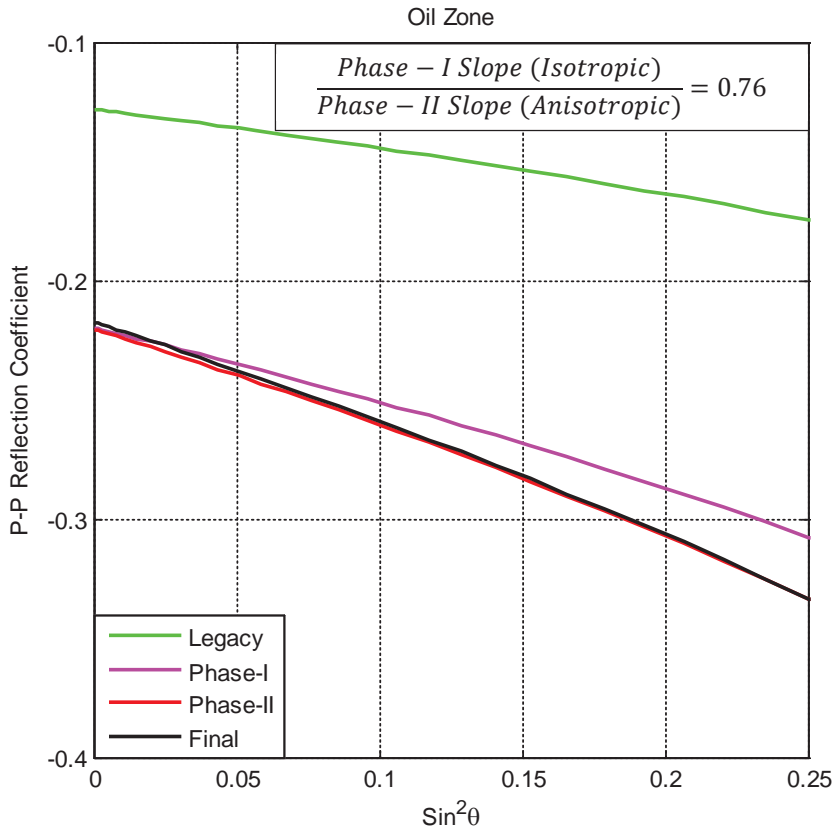


Figure 3. 24. AVO trend of oil zone of 4500-ft sand assuming anisotropic conditions caused by triaxial compression. The AVO response for Phase I (magenta) and legacy (green) are computed for isotropic conditions, and AVO curves for reservoir conditions at the time of Phase II (red) and depletion (black) are computed for anisotropic conditions. The anisotropic parameters used are computed assuming that reservoir is under triaxial compression.

Figure 3.25 shows the stacked seismic section generated from the model generated AVO response (Figure 23). Figure 25(b) shows the respective synthetic squared instantaneous amplitude, an attribute used by Ezawi, Pennington, and Islam (2012) to analyze the time-lapse changes in the Teal south. The modeled stacked section and its Hilbert Transform accurately predict the time-lapse changes observed in the Teal South oil field.

Model predicts brightening of reflections in the gas cap and oil zone from Phase I to Phase II while dimming of reflections is predicted for water encroachment. These predictions of time-lapse changes on stacked sections are consistent with the field

observations reported by Ezawi, Pennington, and Islam (2012). The brightening effect predicted in the oil zone is weaker than the gas cap.

AVO response from water sand shows a little bit of dimming at near offset that turns into brightening at far offset like the water encroachment zone but the strength of reflection is much lower than the reservoir zones. Within the stacking range, near offset dimming and far offset brightening would cancel out leaving almost no time-lapse change from Phase I to Phase II. The stacked and instantaneous amplitudes also show negligible change in the water sand over the life of the reservoir.

[Note: For all models, the saturated rock properties were computed using the Gassmann (1951) equation for fluid substitution for uniform isotropic saturation, even for anisotropic medium. Fluid content has very small effect on anisotropy parameters (Thomsen 2012, Bandyopadhyay 2009) so I ignored the effect of fluid content].

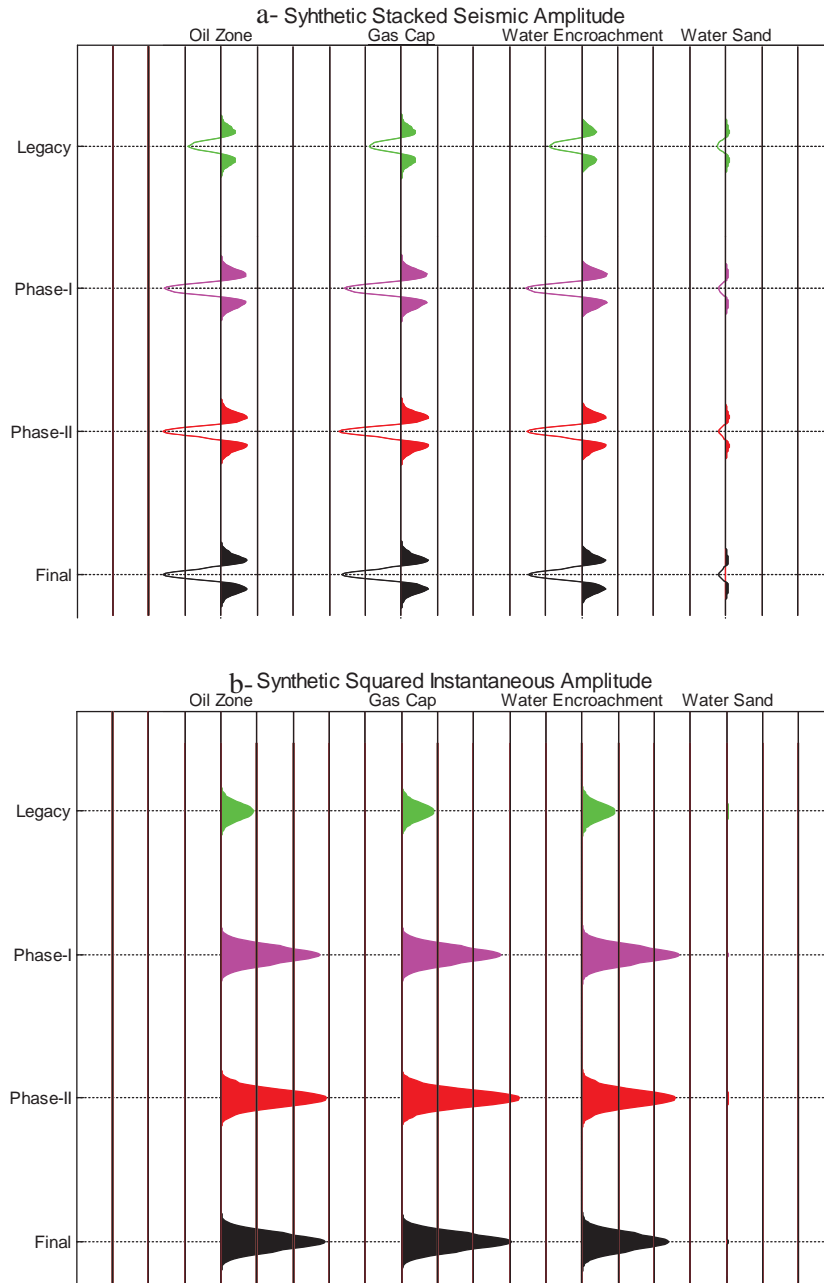


Figure 3. 25. Stacked seismic response predicted by Hertz-Mindlin model assuming anisotropic conditions for Phase-II data caused by assumed triaxial compression. (a) Stacked seismic section predicted from the AVO curves of Figure 3.23 by convolving AVO curves with a 40Hz Ricker wavelet. (b) Synthetic squared instantaneous amplitude computed from the stacked section given in figure 3.25 (a). Both plots show brightening of oil-zone and gas cap from Phase I to Phase II, and show a dimming effect by the water encroachment. Note that change in water sand is just negligible and is hard to see on the stacked seismic sections. All these predictions are perfectly in agreement with the stacked seismic sections of time-lapse surveys in a qualitative sense at least. It is hard to compare the results with the seismic data on a quantitative basis.

### 3.5.3.3. Summary

The stacked seismic data from the Teal South show that reservoir has undergone compaction between Phase I and Phase II causing (some) vertical strain in the reservoir. It is assumed that compaction induced polar anisotropy in the reservoir that is sought to be isotropic before production. Axis of symmetry is assumed to be vertical. Further, it is assumed that there is negligible strain along the horizontal axis. Bandyopadhyay (2009) after Walton (1987) gave relations to compute the Thomsen's anisotropy parameters for uniaxial compression and triaxial conditions. I used his relations to compute the anisotropy parameters for the Teal South reservoir under the above mentioned assumptions, for both assumed uniaxial compaction and triaxial compression conditions.

Thomsen's parameters were then used in (Rüger (1997)) equation to compute the AVO response for anisotropic medium. The elastic properties used were estimated from the Hertz-Mindlin's soft sand model for isotropic conditions. Anisotropy parameters were used only to estimate the AVO response for Phase II and later, assuming that reservoir was isotropic at legacy and Phase I. AVO response was stacked and instantaneous amplitude was estimated.

Adding anisotropy for Phase II improves the accuracy of the model predictions. Adding anisotropy (uniaxial and triaxial), I was able to model the change in AVO trend from Phase I to Phase II. All other models, assuming isotropic conditions, could not predict the change in AVO response from Phase I to Phase II.

Thomsen's parameters estimated under uniaxial compaction modelled the AVO change from Phase I to Phase II more accurately than triaxial compression with small lateral strains. Thomsen's parameters estimated assuming triaxial compression predict the time-lapse changes in the stacked section that are qualitatively in well agreement with the time-lapse seismic data from the reservoir. The model also predicts the AVO change from Phase I to Phase II with a reasonable accuracy. The model suggests that ratio between Phase I AVO gradient and Phase II AVO gradient is 0.76, and a ratio of 0.60 is observed from partial stacks prepared from time-lapse data.

With the limited quality and quantity of the available data and information, the models involving anisotropic parameters has done a decent job of predicting the Phase II AVO response and stacked sections. With the given information and data, it is not possible to decide if triaxial compression has done a better job of modeling or uniaxial compaction. But I will be more confident considering the triaxial compression results more accurate as reservoirs are believed to be under triaxial compression conditions.

Based on above modeling results, it can be reasonably concluded that the 4500-sand had a change in anisotropy because of production from reservoir 'A'. Reservoir might be under isotropic conditions originally, but at sometime after production, it became anisotropic. There are many possible mechanisms behind the production induced

anisotropy, but I assume that 4500-sand became anisotropic because of reservoir compaction.

I also conclude that the change in AVO from Phase I to Phase II can be explained only by assuming a change in anisotropy of the reservoir. No other model explains all the time-lapse changes observed in the seismic data.

The work also shows that anisotropy has a tendency to distort the AVO response significantly, and ignoring anisotropy could be very dangerous in such cases.

### **3.6. Conclusion**

Time-lapse changes observed on the stacked seismic section and pre-stack CMP gathers of the Teal South oil field are modeled using different rock-physics models. Three different rock-physics models were used for this purpose.

Green's model significantly overpredicted the elastic properties of the water sand. Yet, model nicely predicts the time-lapse changes observed on stacked data from legacy to Phase I. This model fails to predict the time-lapse changes after Phase I.

Models based on contact mechanics have done a decent job of simulating the changes in stacked seismic sections and pre-stack gathers. I used the Hertz-Mindlin model for soft conditions, assuming no slip at grain contact. Effective elastic properties of the dry-frame estimated by the Hertz-Mindlin are more accurate than those of predicted by Green's model. The predictions were in good agreement with the elastic properties read from well-logs and observed from seismic data. The model successfully predicts the time-lapse observations from reservoir 'C'. For reservoir 'A', Hertz-Mindlin model predicted the time-lapse changes accurately from legacy to Phase I but under-predicted the brightening of oil zone on stacked section, and similarly does not predict the change in AVO gradient observed on prestack time-lapse data.

Friction factor and pressure dependency of the properties are analyzed for the possible reasons of this discrepancy. None of these models explain the changes in AVO gradient.

Incorporating Walton's model for anisotropic unconsolidated sands helped to explain the time-lapse observations from reservoir 'A'. Walton's model was used to determine the Thomsen's anisotropy parameters. The anisotropy parameters were computed for assumed conditions of uniaxial compaction and triaxial compression. Addition of anisotropy to contact model helped to correctly model the time-lapse changes.

Anisotropy parameters defined under uniaxial compaction better predict the time-lapse AVO changes, and anisotropy parameters derived for triaxial compression case predicts the time-lapse changes of stacked section more accurately than uniaxial compaction.

Based on all this, we conclude that the reservoir was isotropic at the time of discovery, and model it as if it stayed isotropic until the time of Phase I. The reservoir being highly porous, unconsolidated and overpressured at the time of discovery compacted during further production, as suggested by the time-lapse seismic data (discussed in chapter 2). Because of this compaction, the reservoir developed polar anisotropy (weak transverse anisotropy), which significantly increases the slope of AVO curves from Phase I to Phase II.

It is anisotropy that caused the brightening effect from Phase I to Phase II on the stacked data. This anisotropy has the potential to generate a 'false brightspot' on the stacked section, and can be very dangerous if ignored in interpretation. It is very important to include analysis of anisotropy in routine interpretation practices.

Reservoir 'C' in contrast to producing reservoir (reservoir 'A') seems still under isotropic conditions as the time-lapse observations from reservoir 'C' can be correctly modeled using Hertz-Mindlin model under isotropic conditions.

The model also demonstrates that the reflections from water-sand are very weak, and time-lapse changes in such weak reflections are hard to see, especially when plotted on a shared scale with brightspots. Hilbert transform further suppresses the amplitude of these changes, making them effectively invisible.

## 4. Conclusion

Seismic time-lapse and legacy data from Teal South were analyzed aiming to answer the questions raised in previous studies, using seismic attributes, instantaneous amplitude and semblance, identifying specific locations of fluid migration from the produced and nearby reservoirs. AVO analysis quantified aspects of the changes observed in the time-lapse data, requiring anisotropy presumably resulting from reservoir compaction to account for the observations.

Because of regional pressure drop caused by production from reservoir 'A', oil in nearby reservoirs expanded and gas evolved from solution. Reservoir 'B' lies very close to the spill point of reservoir 'C' so as oil escaped from 'C', it was trapped in reservoir 'B' for some time. Reservoir 'B' was saturated with water at the time of discovery, but by the time of Phase I was filled with oil and gas that had leaked from reservoir 'C' and by the time of Phase II was over-filled and oil and gas was escaping from it. A 'tiny' reservoir closer to reservoirs 'B' and 'C' helps to identify the direction of fluid pressure changes.

It is also observed that reservoir 'C' does not show time-lapse changes in oil-zone between Phase I and Phase II, although such changes are evident in the gas cap. One explanation is that frame stiffening cancels the effect of fluid expansion in oil zone, but in gas cap the effect of gas dominates, causing the reflections to be brighter. Modeling of isotropic time-lapse changes suggests that reservoir 'C' was under isotropic conditions at the time of Phase II data acquisition.

Time-lapse data analysis also indicate that the reservoir 'A' has been compacted significantly since the start of production, as evidenced from travel-time shifts, due to the stretching of rocks around the compacting reservoir, and from some shifts in reflections at the base of the reservoir.

Rock-physics models were used to simulate the time lapse AVO trend and predict the stacked outputs for oil zone of reservoir 'A'. The rock-physics models assuming isotropic conditions failed to simulate the time-lapse changes in oil-zone. However, assuming change in isotropic conditions of the reservoir from Phase I to anisotropic conditions by Phase II, the time-lapse changes were correctly predicted. Here we assumed that the reservoir was isotropic at the time of discovery, and that pressure drop due to production induced reservoir compaction, and compaction then induced anisotropy in the reservoir by the time of Phase II.

Using Walton's model for anisotropic unconsolidated sands Thomsen's anisotropic parameters were computed for uniaxial compaction case and triaxial compression case. Using these anisotropic parameters with the elastic properties predicted by hertz-Mindlin model in Rugar's relation for AVO, I correctly predicted the time-lapse variations in AVO and stacked seismic data for all zones of reservoir A.



## 5. Appendices

### 5.1. Appendix A: Reservoir Fluid, Shale and Sand Properties, and Pressure Data

Table A. 1. Fluid properties used in rock-physics modelling discussed in chapter 3.

Reservoir Section	Production Stage	Production Period (Days)	Reservoir Pressure (psi)	Bulk Modulus (MPa)			Density (g/cc)			Saturation			Effective Bulk Modulus (MPa)	Effective Density (g/cc)
				Water	Oil	Gas	Water	Oil	Gas	Water	Oil	Gas		
Oil Zone	Legacy	0	3150	3010	1208	46	1.06	0.80	0.15	0.2	0.8	0	1372	0.852
	Phase I	240	2616	2983.8	1162	36.6	1.06	0.79	0.13	0.2	0.58	0.22	152	0.698
	Phase II	900	2220	2964	1129	29	1.06	0.79	0.11	0.2	0.43	0.37	76	0.591
	Final	1600	1800	2943	1095	23	1.06	0.79	0.09	0.2	0.29	0.51	44	0.485
Gas Cap	Legacy	0	3150	3010	1208	46	1.06	0.80	0.15	0.2	0.8	0	1372	0.852
	Phase I	240	2616	2983.8	1162	36.6	1.06	0.79	0.13	0.2	0.56	0.24	141	0.685
	Phase II	900	2220	2964	1129	29	1.06	0.79	0.11	0.2	0.1	0.70	41	0.366
	Final	1600	1800	2943	1095	23	1.06	0.79	0.09	0.2	0.1	0.70	33	0.351
Water Encroachment Zone	Legacy	0	3150	3010	1208	46	1.06	0.80	0.15	0.2	0.8	0	1372	0.852
	Phase I	240	2616	2983.8	1162	36.6	1.06	0.79	0.13	0.22	0.58	0.2	166	0.717
	Phase II	900	2220	2964	1129	29	1.06	0.79	0.11	0.55	0.25	0.2	137	0.802
	Final	1600	1800	2943	1095	23	1.06	0.79	0.09	0.60	0.20	0.2	110	0.811
Water Sand	Legacy	0	3150	3010	1208	46	1.06	0.80	0.15	1	0	0	3010	1.06
	Phase I	240	2616	2983.8	1162	36.6	1.06	0.79	0.13	1	0	0	2984	1.06
	Phase II	900	2220	2964	1129	29	1.06	0.79	0.11	1	0	0	2964	1.06
	Final	1600	1800	2943	1095	23	1.06	0.79	0.09	1	0	0	2943	1.06

Table A. 2. Rock properties used in rock-physics modeling discussed in chapter 3.

Material	Bulk Modulus (GPa)	Shear Modulus (GPa)	Poisson's Ratio	Density (g/cc)
Quartz (mineral)	37	45	0.0673	2.65
Shale (porous)	9.49	2.024	0.40	2.050

**Table A. 3. Reservoir 'A' production and pressure history**

Date	Oil (BOPM)	Gas (MCFPM)	Water (BWPM)	GOR (SCF/STB)	GOR(X10) (SCF/STB)	Reservoir Pressure (psi)
Nov-96	4132	1076	18	260	2604	3150
Dec-96	63582	21526	54	339	3386	2900
Jan-97	74603	34272	24	459	4594	2775
Feb-97	65022	36601	318	563	5629	2700
Mar-97	52187	35743	7987	685	6849	2680
Apr-97	37408	22388	14067	598	5985	2665
May-97	27092	18992	16330	701	7010	2650
Jun-97	21610	10176	13076	471	4709	2640
Jul-97	21068	14314	15699	679	6794	2620
Aug-97	22225	23631	19517	1063	10633	2600
Sep-97	12082	7340	15006	608	6075	2580
Oct-97	12858	4017	18098	312	3124	2565
Nov-97	15516	8973	19633	578	5783	2550
Dec-97	16080	11422	24002	710	7103	2535
Jan-98	15589	15992	24610	1026	10259	2520
Feb-98	10593	7340	19025	693	6929	2500
Mar-98	14780	5855	24572	396	3961	2480
Apr-98	12746	6409	26428	503	5028	2460
May-98	10599	5535	24912	522	5222	2440
Jun-98	9366	4849	24530	518	5177	2420
Jul-98	9116	5231	25033	574	5738	2400
Aug-98	9282	7795	22914	840	8398	2380
Sep-98	7330	4505	16970	615	6146	2360
Oct-98	8047	5378	22971	668	6683	2340
Nov-98	8308	5405	22688	651	6506	2320
Dec-98	8758	4948	22267	565	5650	2300
Jan-99	8447	5291	20815	626	6264	2290
Feb-99	6987	4015	18231	575	5746	2280

Mar-99	7626	5017	22500	658	6579	2260
Apr-99	7060	4772	21073	676	6759	2240
May-99	6886	3720	20905	540	5402	2220
Jun-99	6435	3118	18706	485	4845	2200
Jul-99	6355	3849	20011	606	6057	2180
Aug-99	2928	1236	10069	422	4221	2160
Sep-99	5294	3288	18339	621	6211	2140
Oct-99	5419	3575	20433	660	6597	2120
Nov-99	5246	4074	18205	777	7766	2100
Dec-99	5116	3177	17736	621	6210	2080
Jan-00	5435	2879	18388	530	5297	2065
Feb-00	2844	1207	6368	424	4244	2050
Mar-00	6417	1733	17932	270	2701	2040
Apr-00	4768	1500	18925	315	3146	2020

## 5.2. Appendix B: Hertz-Mindlin Model

The model gives the following relations for the effective bulk and shear moduli of a dry, random pack of identical spheres(Mavko, Mukerji, and Dvorkin 1998).

$$K_{HM} = \left[ \frac{C^2 (1 - \phi_0)^2 G^2}{18\pi^2 (1 - \nu)^2} P \right]^{1/3} \quad (\text{B.1})$$

$$G_{HM} = \frac{5 - 4\nu}{5(2 - \nu)} \left[ \frac{3C^2 (1 - \phi_0)^2 G^2}{2\pi^2 (1 - \nu)^2} P \right]^{1/3} \quad (\text{B.2})$$

where

$K_{HM}$ = Hertz-Mindlin's effective bulk modulus

$G_{HM}$ = Hertz-Mindlin's effective bulk modulus

$C$ = Co-ordination number (average number of contacts per sphere)

$\Phi_0$ = Initial porosity (porosity of un-compacted sand)

$G$ = Grain's shear modulus (GPa)

$P$ = Applied Hydrostatic Pressure

$\nu$ = Grain's Poisson's Ratio

Hashin-Shtrikman's (Hashin and Shtrikman 1963) lower bound is used to estimate the effective moduli ( $K_{eff}$  and  $G_{eff}$ ) at porosities ( $\phi$ ) other than the initial un-compacted porosities. The equations are given below.

$$K_{eff} = \left[ \frac{\phi / \phi_0}{K_{HM} + \frac{4}{3} G_{HM}} + \frac{1 - \phi / \phi_0}{K + \frac{4}{3} G_{HM}} \right]^{-1} - \frac{4}{3} G_{HM} \quad (B.3)$$

$$G_{eff} = \left[ \frac{\phi / \phi_0}{G_{HM} + \frac{G_{HM}}{6} \left( \frac{9K_{HM} + 8G_{HM}}{K_{HM} + 2G_{HM}} \right)} + \frac{1 - \phi / \phi_0}{G + \frac{G_{HM}}{6} \left( \frac{9K_{HM} + 8G_{HM}}{K_{HM} + 2G_{HM}} \right)} \right]^{-1} - \frac{G_{HM}}{6} \left( \frac{9K_{HM} + 8G_{HM}}{K_{HM} + 2G_{HM}} \right) \quad (B.4)$$

Equation B.2 assumes no slip at grain contacts so overestimate the shear strength. Mavko, Mukerji, and Dvorkin (1998) introduced an ad hoc coefficient 'f' to account for friction at grain contacts, and gave the following relation for shear modulus.

$$\mu'_{HM} = \frac{2 + 3f - \nu(1 + 3f)}{5(2 - \nu)} \left[ \frac{3C^2(1 - \phi)^2 \mu^2}{2\pi^2(1 - \nu)^2} P \right]^{1/3} \quad (B.5)$$

'f' defines the amount of average friction at contacts.

For perfect adhesion,  $f=1$ , and the equation becomes equivalent to the standard Hertz-Mindlin equation (B.2) for shear modulus, and in this case Poissons's ratio does not exceed 0.10. In contrast to this, absence of friction may occur in unconsolidated sands because of the presence of lubricants at some contacts (Mavko, Mukerji, and Dvorkin 1998). In this case  $f=0$ , and shear modulus will be given by the following equation:

$$\mu'_{HM} = \frac{1}{5} \left[ \frac{3C^2(1 - \phi)^2 \mu^2}{2\pi^2(1 - \nu)^2} P \right]^{1/3} \quad (B.6)$$

### 5.3. Appendix C: Walton's Model for Anisotropic Medium and Thomsen's Anisotropy Parameters

Famous anisotropy parameters are due to Thomsen (1986). He demonstrates that a transversely isotropic medium can be defined by only five independent constants.

$$\begin{bmatrix} C_{11} & C_{12} & C_{13} & & & \\ C_{12} & C_{11} & C_{13} & & & \\ C_{13} & C_{13} & C_{33} & & & \\ & & & C_{44} & & \\ & & & & C_{44} & \\ & & & & & C_{66} \end{bmatrix}, \text{ where } C_{66} = 1/2(C_{11} - C_{12}) \quad (\text{C.1})$$

He proposed the following notations to describe a weak transverse anisotropic medium.

$$\text{P-wave velocity,} \quad \alpha = \sqrt{C_{33}/\rho} \quad (\text{C.2})$$

$$\text{S-wave velocity,} \quad \beta = \sqrt{C_{44}/\rho} \quad (\text{C.3})$$

$$\text{P-wave anisotropy parameter,} \quad \varepsilon = \frac{(C_{11} - C_{33})}{2C_{33}} \quad (\text{C.4})$$

$$\text{S-wave anisotropy,} \quad \gamma = \frac{(C_{66} - C_{44})}{2C_{44}} \quad (\text{C.5})$$

$$\& \quad \delta = \frac{(C_{13} + C_{44})^2 - (C_{33} - C_{44})^2}{2C_{33}(C_{33} - C_{44})} \quad (\text{C.6})$$

' $\varepsilon$ ' describes the fractional difference between the p-wave velocities along and normal to the symmetry axis. ' $\gamma$ ' describes the fractional difference between SH- velocities along and normal to the axis of symmetry (Mavko, Mukerji, and Dvorkin 2009). ' $\delta$ ' describes the angular dependence of p-wave velocity. It defines the second derivative of p-wave phase velocity function at vertical incidence (Tsvankin, Helbig, and Treitel 2001, Bandyopadhyay 2009). (Thomsen 1986) also demonstrates that ' $\delta$ ' is the most important anisotropy parameter as it affects the reflections at small incidence angles where most of the reflection profiling takes place.

For weak transverse anisotropic conditions the Thomsen's parameter ' $\delta$ ' can be approximated by (Tsvankin, Helbig, and Treitel 2001):

$$\delta \approx \frac{(C_{13} + 2C_{44} - C_{33})}{C_{33}} \quad (\text{C.7})$$

An additional parameter ‘ $\eta$ ’ was introduced by (Alkhalifah and Tsvankin 1995). It is called ‘anellipticity’ parameter and defines the effects of anisotropy on moveout. It is defined by the following relation.

$$\eta = \frac{\varepsilon - \delta}{1 + 2\delta} \quad (\text{C.8})$$

Walton (1987) using contact law has derived the relations to compute the elastic stiffness of an anisotropic medium under an arbitrary applied strain. The elastic stiffness then can be used in equations 3.15 -3.18 to compute the anisotropy parameters. Walton has also given expressions for effective moduli. The expressions are similar to Hertz-Mindlin model, and defines the moduli for two distinct scenario; no-slip ( $f=1.0$  for Hertz-Mindlin) and no-friction ( $f=0.0$  for Hertz-Mindlin). Walton assumes that normal and shear deformation of two-grains in contact occur simultaneously while the Hertz-Mindlin model assumes that normal deformation occur first and then a tangential deformation may occur at grain contacts (Mavko, Mukerji, and Dvorkin (2009)). Walton’s model for anisotropic sands is applicable to only uniaxial strain. Bandyopadhyay (2009) corrected his relation for shear moduli, and then extended this model for triaxial strain conditions.

Bandyopadhyay (2009) give the following equations for Thomsen’s parameter under uniaxial compression. The equations given below are for rough contacts (i.e.  $f=1$  for the Hertz-Mindlin model).

$$\varepsilon = -\frac{5\alpha + 2\beta}{16(\alpha + \beta)}, \quad (\text{C.9})$$

$$\gamma = -\frac{\alpha + \beta}{2(2\alpha + 5\beta)}, \quad (\text{C.10})$$

$$\delta = -\frac{5\alpha + 2\beta}{12(2\alpha + \beta)}, \quad (\text{C.11})$$

$$\alpha = \frac{(1 - \phi)N(-E_{33})^{1/2}}{32\pi^2 B}, \quad (\text{C.12})$$

$$\beta = \frac{(1 - \phi)N(-E_{33})^{1/2}}{32\pi^2 (2B + C)} \quad (\text{C.13})$$

$$B = \frac{1}{4\pi} \left\{ \frac{1}{\mu} + \frac{1}{\mu + \lambda} \right\}, \quad (\text{C.14})$$

$$C = \frac{1}{4\pi} \left\{ \frac{1}{\mu} - \frac{1}{\mu + \lambda} \right\}, \quad (\text{C.15})$$

‘ $\mu$ ’ and ‘ $\lambda$ ’ are the Lamé constant for the grain material, and  $E_{33}$  is the strain along the axis of applied stress (vertical here).

For triaxial compression case, Bandyopadhyay (2009) defines a new term, called the ‘stress anisotropy’ and is defined as

$$E_r = \frac{E_{11} - E_{33}}{2E_{33}}, \quad (\text{C.16})$$

Thomsen’s parameters for a medium under triaxial compression are then defined by the following relations.

$$\varepsilon = \frac{2E_r(3C + 7B)}{7(3C + 10B) + 2(3C + 14B)E_r}, \quad (\text{C.17})$$

$$\gamma = \frac{E_r(2C + 7B)}{2[7(C + 5B) + (4C + 21B)E_r]}, \quad (\text{C.18})$$

$$\delta \approx \varepsilon, \quad (\text{C.19})$$

The equations 3.27-3.30 assume that the strain along vertical axis is larger than the horizontal axis i.e.,  $E_{33} \gg E_{11}$ . Also it assumes equal strain along both lateral directions i.e.,  $E_{11} = E_{22}$ . The equations are valid for weak transvers anisotropy.

(Thomsen (1993)) gave the relations for reflection coefficient of a medium with weak anisotropy. Rüger (1997) modified his relation and derived a new approximation that is given below.

$$R_{pp}(\theta) = \frac{1}{2} \frac{\Delta Z}{Z} + \frac{1}{2} \left\{ \frac{\Delta V_{P0}}{V_{P0}} - \left( \frac{2\Delta V_{S0}}{V_{P0}} \right)^2 \frac{\Delta G}{G} + \Delta \delta \right\} \sin^2 \theta + \frac{1}{2} \left\{ \frac{\Delta V_{P0}}{V_{P0}} + \Delta \varepsilon \right\} \sin^2 \theta \tan^2 \theta \quad (\text{C.20})$$

where

$Z =$  Acoustic impedance  $= \rho V_{P0}$ ,

$V_{P0} =$  Vertical P-wave velocity,

$V_{S0} =$  Vertical S-wave velocity,

$G =$  Vertical shear modulus  $= \rho V_{S0}^2$

$\theta =$  Incident phase-angle

## 5.4. Appendix D: CMP Gathers Generated from the AVO curves Predicted by Rock Physics Models

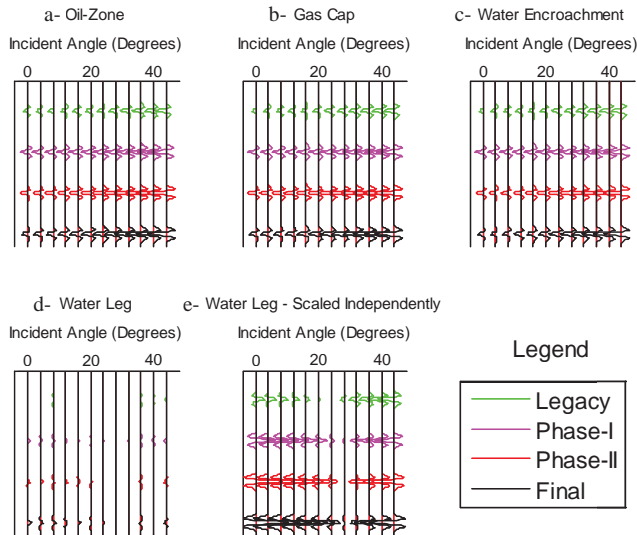


Figure D. 1. NMO corrected synthetic CMP gathers presenting AVO response for 4500-ft sand predicted from Green's model and Zoeppritz equations. The gathers were generated by convolving a 40Hz Ricker wavelet with the AVO response shown in figure 3.7. The amplitudes of all CMP gathers given in figures (a-d) are scaled equally while the CMP gather for water-sand given in (e) is scaled independently.

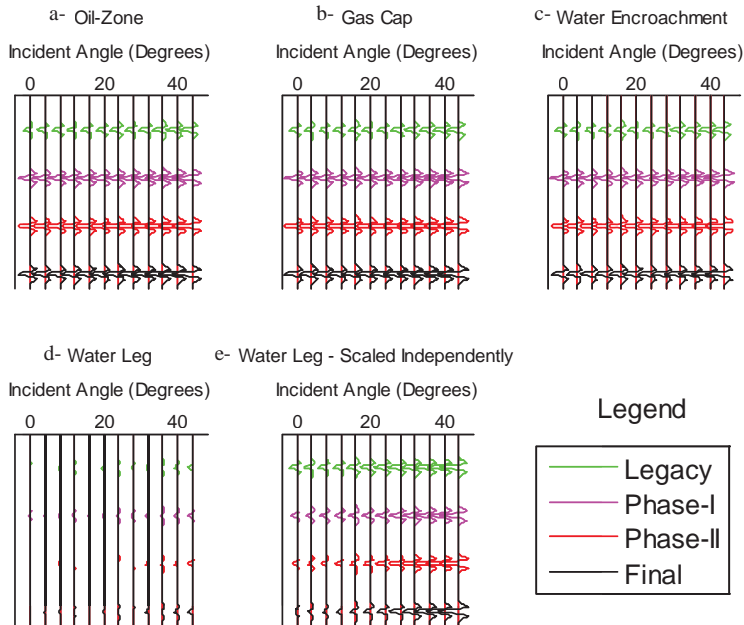


Figure D. 2. Synthetic CMP gathers presenting the AVO response of 4500-ft predicted by the Hertz-Mindlin model. AVO response of figure 3.12 was convolved with a 400 Hz Ricker wavelet to generate the CMP gathers.

## **5.5. Appendix E: Permissions to use copyrighted material.**

### **E.1. Permission for figures 1.1 and 1.2.**

Following text is copied from google website on August 6, 2014 at 02:28 PM. The text is available at the following link.

<http://www.google.com/permissions/geoguidelines.html#maps-print>

“To determine if your proposed use of Content is acceptable, you should first read closely the applicable Terms of Service:

- [Google Maps/Google Earth Terms and Conditions](#)
- [Google Maps/Google Earth APIs Terms of Service](#)

Your use of Content, as defined in the Terms of Service, in anything from marketing and promotional materials to films and books is first and foremost governed by the license provided in the applicable Terms of Service for the product. In certain circumstances, Google may be able to grant you a broader license to use the Content in a manner not covered in the Terms of Service. Plus, apart from any license granted to you by Google, your use of Content may be acceptable under principles of "fair use."

Fair use is a concept under copyright law in the U.S. that, generally speaking, permits you to use a copyrighted work in certain ways without obtaining a license from the copyright holder. There are a variety of factors that affect whether your use of Content would be considered fair use, including the purpose and character of your use, the nature of the copyrighted work, the amount of the copyrighted material used, and the effect of your use upon the potential market for the copyrighted work. For example, there are differences between use in a for-fee service and use in a work of scholarship, or the use of a single map screenshot and the use of detailed map images for an entire country. There are similar, although generally more limited, concepts in other countries' copyright laws, including a concept known as "fair dealing" in a number of countries. That all being said."

“Due to limited resources and high demand, we are unable to sign any letter or contract specifying that your project or use has our explicit permission. The only exception is when you apply for a television and film [broadcast license](#).”

### **E.2. Permission for use of figure 3.2, 3.3 and 3.4**

The text below is copied from email communication between the author (Nayyer Islam) and The Director Publications, Society of Exploration Geophysicists (SEG).

July 26, 2014.

“Greetings Nayyer,

You have SEG’s permission to use the figures cited below in your doctoral dissertation. SEG asks only that you provide complete citations for the figures.”

Sincerely,

Ted

Ted Bakamjian, IOM CAE

Director, Publications

Society of Exploration Geophysicists

P. O. Box 702740, Tulsa, OK 74170-2740 USA

Web: <http://www.seg.org/>

SEG Digital Library: <http://library.seg.org>

On Jul 23, 2014, at 5:02 PM, Nayyer Islam <[nislam@mtu.edu](mailto:nislam@mtu.edu)> wrote:

Respected SEG Publications Director,

I am a PhD candidate at Michigan Technological University. I am working on my dissertation, and I need permission to reproduce/republish four copyrighted figures from The Leading Edge’s October 2001 edition in my dissertation. The dissertation will generate two publications that we (myself and Dr. Wayne D. Pennington [my adviser]) will publish with SEG. Dr. Pennington is also the first author on the paper I am seeking permission for. Below is the complete citation for the paper.

Pennington, W. D., H. Acevedo, J. I. Haataja, and A. Minaeva. 2001, Seismic time-lapse surprise at Teal South: That little neighbor reservoir is leaking! : The Leading Edge, 20, no. 10, 1172-1175.

doi: 10.1190/1.1487249

I need permission for following figures; figure 2, figure 5, figure 7 and figure 10. The figures will be used for a discussion of previous work and data extraction.

Your help in this regard will be highly appreciated.

Sincerely,

Nayyer Islam

PhD Candidate, Geological Engineering

President, Geophysical Society at MTU

## 6. References

- Alkhalifah, T., and I. Tsvankin. 1995, Velocity analysis for transversely isotropic media. *Geophysics*, **60**, no. 5,1550-1566.
- Bachrach, R., and P. Avseth. 2008, Rock physics modeling of unconsolidated sands: Accounting for nonuniform contacts and heterogeneous stress fields in the effective media approximation with applications to hydrocarbon exploration. *Geophysics*, **73**, no. 6,E197-E209.
- Bachrach, R., J. Dvorkin, and A. M. Nur. 2000, Seismic velocities and Poisson's ratio of shallow unconsolidated sands. *Geophysics*, **65**, no. 2,559-564.
- Backus, G. E. 1962, Long-wave elastic anisotropy produced by horizontal layering. *Journal of Geophysical Research*, **67**, no. 11,4427-4440.
- Bandyopadhyay, K. 2009, Seismic anisotropy: Geological causes and its implications to reservoir geophysics: Stanford University.
- Banik, N. 1987, An effective anisotropy parameter in transversely isotropic media. *Geophysics*, **52**, no. 12,1654-1664.
- Barkved, O. I., and T. Kristiansen. 2005, Seismic time-lapse effects and stress changes: Examples from a compacting reservoir. *The Leading Edge*, **24**, no. 12,1244-1248.
- Barnes, A. E. 2007, A tutorial on complex seismic trace analysis. *Geophysics*, **72**, no. 6,W33-W43.
- Batzle, M., and Z. Wang. 1992, Seismic properties of pore fluids. *Geophysics*, **57**, no. 11,1396-1408.
- Bracewell, R. N. 1965, *The Fourier transform and its applications*: McGraw-Hill New York.
- Christie, M., C. MacBeth, and S. Subbey. 2002, Multiple history-matched models for Teal South. *The Leading Edge*, **21**, no. 3,286-289.
- Digby, P. 1981, The effective elastic moduli of porous granular rocks. *Journal of Applied Mechanics*, **48**, no. 4,803-808.
- Druzhinin, A., and C. MacBeth. 2001, Robust cross-equalization of 4D-4C PZ migrated data at Teal South. Paper read at 71st SEG meeting, San Antonio, USA, Expanded Abstracts.
- Duffaut, K., and M. Landrø. 2007,  $V_p/V_s$  ratio versus differential stress and rock consolidation—A comparison between rock models and time-lapse AVO data. *Geophysics*, **72**, no. 5,C81-C94.
- Duffy, J., and R. D. Mindlin. 1957, Stress-strain relations and vibrations of a granular medium. DTIC Document.
- Eberhart-Phillips, D., D.-H. Han, and M. D. Zoback. 1989, Empirical relationships among seismic velocity, effective pressure, porosity, and clay content in sandstone. *Geophysics*, **54**, no. 1,82-89.
- Ebrom, D., P. Krail, D. Ridyard, and L. Scott. 1998, 4-C/4-D at Teal South. *The Leading Edge*, **17**, no. 10,1450-1453.
- Ebrom, D., B. Nolte, G. Purnell, D. Sukup, P. Krail, and T. EPTD. 1998, Analysis of multicomponent seismic data from offshore Gulf of Mexico. Paper read at 68 th Annual Meeting SEG Expanded Abstracts.

- Ezawi, M. A., W. D. Pennington, and N. Islam. 2012, Time-Lapse Seismic Observations of Regional Gas Blowdown at Teal South. Paper read at 2012 SEG Annual Meeting.
- Goddard, J. 1990, Nonlinear elasticity and pressure-dependent wave speeds in granular media. *Proceedings of the Royal Society of London. Series A: Mathematical and Physical Sciences*, **430**, no. 1878,105-131.
- Green, A. M. 2001, THE EFFECTS OF THE VARIATION OF EFFECTIVE PRESSURE IN RESERVOIRS ON MEASURED COMPRESSIONAL WAVE AND SHEAR WAVE SEISMIC VELOCITIES, Michigan Technological University.
- Hall, S. A., and C. MacBeth. 2001, AVOA attribute analysis and cross-plotting for time-lapse monitoring of stress and saturation changes: Application to the Teal South 4D-4C dataset. Paper read at 2001 SEG Annual Meeting.
- Hashin, Z., and S. Shtrikman. 1963, A variational approach to the theory of the elastic behaviour of multiphase materials. *Journal of the Mechanics and Physics of Solids*, **11**, no. 2,127-140.
- Hatchell, P., and S. Bourne. 2005, Rocks under strain: Strain-induced time-lapse time shifts are observed for depleting reservoirs. *The Leading Edge*, **24**, no. 12,1222-1225.
- Hawkins, K., S. Howe, S. Hollingworth, G. Conroy, L. Ben-Brahim, C. Tindle, N. Taylor, G. Joffroy, and A. Onaisi. 2007, Production-induced stresses from time-lapse time shifts: A geomechanics case study from Franklin and Elgin fields. *The Leading Edge*, **26**, no. 5,655-662.
- Herwanger, J., and S. Horne. 2005, Predicting time-lapse stress effects in seismic data. *The Leading Edge*, **24**, no. 12,1234-1242.
- Huffman, A. R., and J. P. Castagna. 2001, The petrophysical basis for shallow-water flow prediction using multicomponent seismic data. *The Leading Edge*, **20**, no. 9,1030-1052.
- Landrø, M., and J. Stammeijer. 2004, Quantitative estimation of compaction and velocity changes using 4D impedance and travelttime changes. *Geophysics*, **69**, no. 4,949-957.
- Mavko, G., T. Mukerji, and J. Dvorkin. 1998, *The Rock Physics Handbook: Tools for Seismic Analysis in Porous Media*. Cambridge University Press, Cambridge, New York, USA.
- Mavko, G., T. Mukerji, and J. Dvorkin. 2009, *The rock physics handbook: Tools for seismic analysis of porous media*: Cambridge university press.
- Mindlin, R. 1949, Compliance of elastic bodies in contact. *Journal of applied mechanics*, **16**.
- Norris, A., and D. Johnson. 1997, Nonlinear elasticity of granular media. *Journal of Applied Mechanics*, **64**, no. 1,39-49.
- Pennington, W. D., H. Acevedo, A. Green, J. Haataja, S. Len, A. Minaeva, and D. Xie. 2002, Calibration of seismic attributes for reservoir characterization. Final Report MTU, Houghton.

- Pennington, W. D., H. Acevedo, J. I. Haataja, and A. Minaeva. 2001, Seismic time-lapse surprise at Teal South: That little neighbor reservoir is leaking! : The Leading Edge, **20**, no. 10,1172-1175.
- Pennington, W. D., A. M. Green, and J. I. Haataja. 2001, Seismic Petrophysical Modeling of Oil and Gas Production: Teal South Field, Gulf of Mexico. Paper read at AAPG Annual Convention,, at Denver, Colorado.
- Prasad, M. 2002, Acoustic measurements in unconsolidated sands at low effective pressure and overpressure detection. *Geophysics*, **67**, no. 2,405-412.
- Rickett, J., and D. E. Lumley. 1998, A cross-equalization processing flow for off-the-shelf 4-D seismic data. 68th Ann. Internat. Mtg,16-19.
- Rodriguez-Suarez, C., R. R. Stewart, and H.-X. Lu. 2000, Analysis of the Teal South, Gulf of Mexico, 3D-4C seismic survey. Paper read at 70th Annual Meeting SEG Expanded Abstracts.
- Rüger, A. 1997, P-wave reflection coefficients for transversely isotropic models with vertical and horizontal axis of symmetry. *Geophysics*, **62**, no. 3,713-722.
- Shams, A., and C. MacBeth. 2002, Robust time-lapse AVOA analysis using OBC: A case study from Teal South. Paper read at 72nd SEG Meeting, Salt Lake City, USA, Expanded Abstracts.
- Shuey, R. 1985, A simplification of the Zoeppritz equations. *Geophysics*, **50**, no. 4,609-614.
- Stovas, A., and M. Landro. 2005, Fluid-pressure discrimination in anisotropic reservoir rocks - A sensitivity study. *Geophysics*, **70**, no. 3,O1-O11. doi: 10.1190/1.1926576.
- Stovas, A., and M. Landrø. 2005, Fluid-pressure discrimination in anisotropic reservoir rocks—A sensitivity study. *Geophysics*, **70**, no. 3,O1-O11.
- Taner, M. T., F. Koehler, and R. Sheriff. 1979, Complex seismic trace analysis. *Geophysics*, **44**, no. 6,1041-1063.
- Thomsen, L. 1986, Weak elastic anisotropy. *Geophysics*, **51**, no. 10,1954-1966.
- Thomsen, L. 1993, Weak anisotropic reflections. Offset-dependent reflectivity—Theory and practice of AVO analysis: *Soc. Expl. Geophys*,103-111.
- Thomsen, L. 2012, On the fluid dependence of the parameters of anisotropy. Paper read at 2012 SEG Annual Meeting.
- Tsvankin, I., K. Helbig, and S. Treitel. 2001, Seismic signatures and analysis of reflection data in anisotropic media.
- Walton, K. 1987, The effective elastic moduli of a random packing of spheres. *Journal of the Mechanics and Physics of Solids*, **35**, no. 2,213-226.
- Wright, J. 1987, The effects of transverse isotropy on reflection amplitude versus offset. *Geophysics*, **52**, no. 4,564-567.
- Xu, S. 2002, Stress-induced anisotropy in unconsolidated sands and its effect on AVO analysis. Paper read at 2002 SEG Annual Meeting.
- Zhang, J. J., and L. R. Bentley. 2000, Complex seismic trace analysis and its application to time-lapse seismic surveys. CREWES, Geology and Geophysics, University of Calgary.

- Zimmer, M. A. 2004, Seismic velocities in unconsolidated sands: Measurements of pressure, sorting, and compaction effects: Stanford University.
- Zoeppritz, K. 1919, On the reflection and propagation of seismic waves at discontinuities. *Erdbebenwellen VII B*,66-84.